

Growth of Epitaxial Graphene on 6H-SiC and Its Characterization by Surface Analysis Methods

Akkawat Ruammitree

Growth of Epitaxial Graphene on 6H-SiC and Its Characterization by Surface Analysis Methods

**6H-SiC 上のエピタキシャルグラフェンの成長と
表面分析法によるその評価**

Akkawat Ruammitree

Department of Quantum Engineering
Graduate School of Engineering

Doctor of Engineering

Nagoya University

2014

Contents

Chapter 1	Introduction.....	5
1.1	Graphene structure and its properties.....	5
1.2	Dependence of graphene electronic property on graphene layer number.....	6
1.3	History of graphene fabrication.....	7
1.4	SiC structure and its properties.....	8
1.5	Growth of graphene on SiC by thermal decomposition in Argon gas atmosphere.....	10
1.6	Purpose of this study.....	12
1.7	Outline of this thesis.....	13
Chapter 2	Experimental methods.....	16
2.1	Basic principle of analytical methods.....	16
2.1.1	Atomic force microscopy.....	16
2.1.2	Angle resolved photoemission spectroscopy.....	19
2.1.3	Reflection high-energy electron diffraction.....	20
2.1.4	X-ray diffraction.....	21
2.2	Basic principle for X-ray diffraction.....	23
2.2.1	Classic scattering from a free electron.....	23

2.2.2 Scattering from several electrons.....	26
2.2.3 Scattering by an atom.....	27
2.2.4 Diffraction by graphene on SiC (0001).....	29
Reference for chapter 2.....	31

Chapter 3 Synthesis and characterization of epitaxial graphene

on 6H-SiC (0001).....	32
3.1 Graphene Synthesis.....	32
3.1.1 SiC single crystalline substrate.....	32
3.1.2 Thermal treatment of SiC.....	32
3.2 Characterization of epitaxial graphene on 6H-SiC (0001).....	35
3.2.1 Reflection high-energy electron diffraction (RHEED).....	35
3.2.2 Synchrotron X-ray diffraction (XRD).....	36
3.2.3 Angle-resolved photoemission spectroscopy (ARPES).....	36

Chapter 4 Graphene film thickness estimation by X-ray diffraction.....40

4.1 Experimental.....	41
4.2 Thickness estimation by XRD method.....	42
4.2.1 Calculation method for graphene thickness estimation.....	44
4.2.2 Fitting calculated curve with uniform model on XRD experimental curve.....	47
4.2.3 Fitting calculated curve with non-uniform model on XRD experimental data.....	48

4.3 Confirmation of the thickness estimation by SEM.....	56
4.4 Confirmation of the thickness estimation by ARPES.....	59
4.5 Confirmation of the thickness estimation by Raman.....	62
4.6 Conclusion.....	63
References for chapter 4.....	64

Chapter 5 Growth of epitaxial graphene with large domain on C-terminated 6H-SiC (000 $\bar{1}$).....	66
5.1 Experimental.....	67
5.2 Structure of graphene on C-face SiC measured by RHEED	67
5.3 Graphene properties characterized by Raman.....	70
5.4 Surface morphology.....	72
5.5 Conclusions.....	75
References for chapter 5.....	75

Chapter 6 Growth of embedded and protrusive striped graphene on Si-terminated 6H-SiC (0001).....	77
6.1 Experimental.....	77
6.2 Structure of graphene on Si-face SiC measured by RHEED	78
6.3 Growth of embedded and protrusive striped graphene on Si-face SiC (0001).....	84
6.4 Raman characterization.....	94
6.5 Conclusions.....	95

References for chapter 6.....	96
Chapter 7 Growth of non-concentric graphene ring on Si-face	
6H-SiC (0001) surface.....	98
7.1 Experimental.....	99
7.2 Condition for the growth of graphene ring on Si-face SiC (0001).....	99
7.3 Edge structure of graphene ring	102
7.4 Growth of graphene rings.....	104
7.5 Discussion.....	107
7.5.1 Growth of graphene stripe at step edge.....	107
7.5.2 Growth process of graphene rings.....	108
7.6 Conclusions.....	112
References for chapter 7.....	114
Chapter 8 Summary of this thesis.....	117
Acknowledgements.....	119
List of Papers.....	120
Original Paper	120
International Conferences.....	121
Awards.....	123

Chapter 1

Introduction

1.1 Graphene structure and its properties

Graphene is an allotrope of carbon, in which carbon atoms are arranged into a two-dimension honeycomb lattice as shown in Figure 1.1 (a). The unit mesh of graphene is formed by two unit cell vectors of $|\mathbf{a}_G| = |\mathbf{b}_G| = 0.24589$ nm. A unit cell (shaded area) contains 2 carbon atoms. Figure 1.1 (b) shows chemical bondings between atoms in graphene. Graphene has two important bondings which are a π bond perpendicular to the planar sheet and sp^2 bond (σ bond) in-plane sheet.

Graphene has a variety of exotic properties such as its high strength and flexibility. Namely, graphene is about 100 times stronger than steel and it can be stretched by 20 percent. And yet, graphene is flexible like rubber [2]. In the electronic band structure, graphene has remarkable electronic properties such as high mobility and linear dispersion (Dirac cone) at the K-point in the Brillouin zone where the valence and conduction bands touch with each other as shown in the magnified image in Figure 1.1 (b). The velocity of graphene electrons near the Dirac cone can be calculated by the relation of $E = \hbar k v_f$ where E is electron energy; \hbar is Planck's constant divided by 2π ; k is wave vector and v_f is the Fermi velocity. The calculation shows the value of v_f of $\sim 10^6$ m/s. These unique properties of graphene make it a promising candidate for the future electronic and photonic devices.

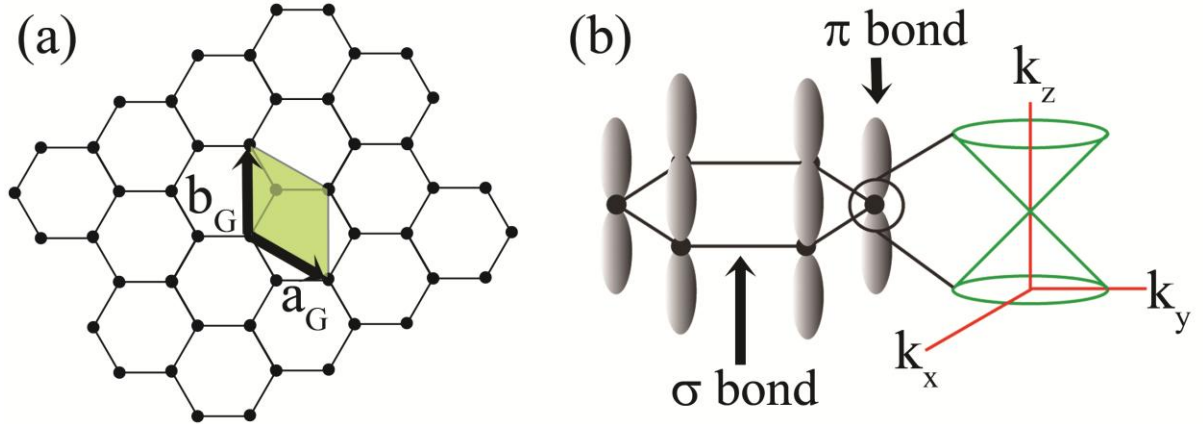


Figure 1.1. (a) Structure of graphene and (b) Bondings on graphene. The magnified image shows the linear dispersion at the K point.

1.2 Dependence of graphene electronic property on graphene layer number

Figure 1.2 shows calculated electronic band curves of graphene film which covers on Si-face SiC [1]. In the case of buffer layer, there is no Dirac cone and the band gap is very wide. For monolayer graphene (2 carbon layers) there is a Dirac cone where the conduction and valence bands touch each other without band gap. In the case of bilayer graphene, there are two parabolic bands with a small band gap. The parabolic bands originate from the interaction of Fermi electrons. As described above, graphene electronic properties vary with layer number of graphene and hence the accurate method for graphene thickness estimation is necessary. In chapter 4 of this thesis the author demonstrates an accurate method for graphene film thickness estimation by using X-ray diffraction.

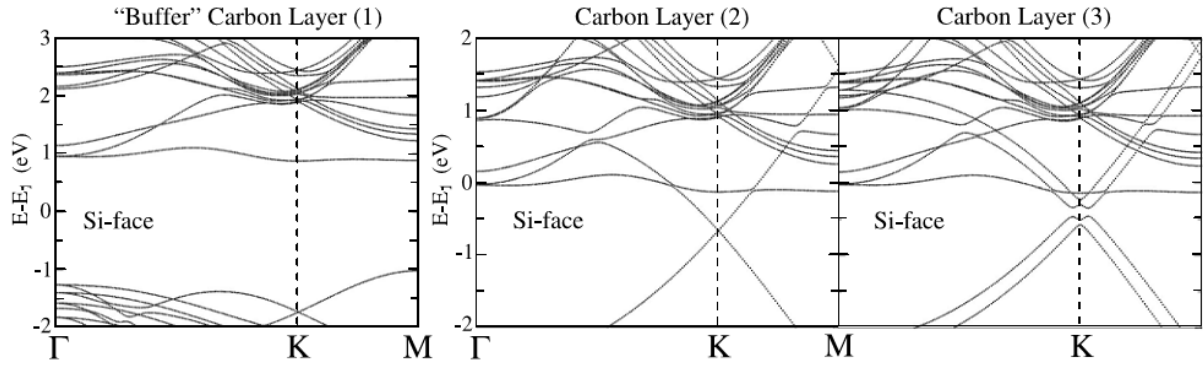


Figure 1.2. Calculated electron band structures of graphene on Si-face SiC. Reproduced by permission of IOP Publishing [1] and reprinted with permission from [3]. Copyright (2007) by the American Physical Society.

1.3 History of graphene fabrication

Graphene was first produced in 2004 by Andre Geim, Konstantin Novoselov and their collaborators from the University of Manchester, UK and the Institute for Microelectronics Technology in Chernogolovka, Russia [4]. In 2010, the Nobel Prize in physics was awarded to Andre Geim and Konstantin Novoselov. Nevertheless there are some groups reporting that Andre Geim and Konstantin Novoselov are not the first people who discover graphene, i.e. there are some research group produced graphene before them. The timeline about history of graphene fabrication is shown in Table 1.1.

Table 1.1. Timeline in the history of graphene preparation modified from reference [5].

Period	Event	Worker names
1840-1958	Graphite oxide was prepared.	Schafhaeutl, Brodie, staudenmaier, Hummers and others
1962	Reduced graphene oxide (r-Go) by the chemical and thermal reduction of graphite oxide.	Boehm and co-workers
1969	Graphene monolayer on the Pt surface was confirmed.	Morgan and Somorjai
1970	graphene monolayer was prepared by segregating carbon on the surface of Ni (100).	Blakely and co-workers
1975	graphene monolayer was prepared by subliming silicon from silicon carbide.	Van Bommel and co-workers
1999	Graphite was micromechanically exfoliated into thin lamellae comprised of multiple layers of graphene	Ruoff and co-workers
2004	Graphene was prepared by micromechanical exfoliation.	Geim and co-workers

Graphene can be fabricated by various methods such as mechanical exfoliation of graphite, chemical vapor deposition (CVD) of carbon-bearing gases on the surface of copper films [6]-[7], and cutting open nanotubes [8]. The growth of graphene by heating silicon carbide (SiC) crystals is also one of the efficient approaches for a large scale production of graphene. For some applications such as field-effect transistors (FETs) need a substrate which has graphene on an insulator. The transference of graphene which was grown elsewhere, onto another insulator degrades the graphene properties such as carrier mobility. The growth of graphene on a SiC substrate can solve this problem because SiC is a semi-insulator.

1.4 SiC structure and its properties

Silicon carbide (SiC) is an extremely hard material which consists of silicon and carbon atoms. In this thesis, I study on the growth of epitaxial

graphene on SiC. The knowledge about the SiC structures is necessary because they can affect on the growth of epitaxial graphene. Moreover, understanding of SiC structures such as interlayer spacings help us to distinguish between SiC and epitaxial graphene peaks in X-ray diffraction when the sample is measured to determine the graphene film thickness (see chapter 4). Generally, there are 2 types of SiC which are commonly used, i.e., 4H-SiC and 6H-SiC. An nH-SiC unit cell is defined by n bilayers of SiC. For example, 4H and 6H-SiC contain 4 and 6 SiC bilayers, respectively. Each bilayer of SiC consists of Si and C plane. Figure 1.3 shows schematic of the unit cell structure of 4H and 6H-SiC. The lattice constant (a_{SiC}) and layer spacing are ~ 0.308 nm and ~ 0.25 nm, respectively, for both types. In addition, the stacking sequences for 4H and 6H-SiC are ABCB... and ABCACB..., respectively.

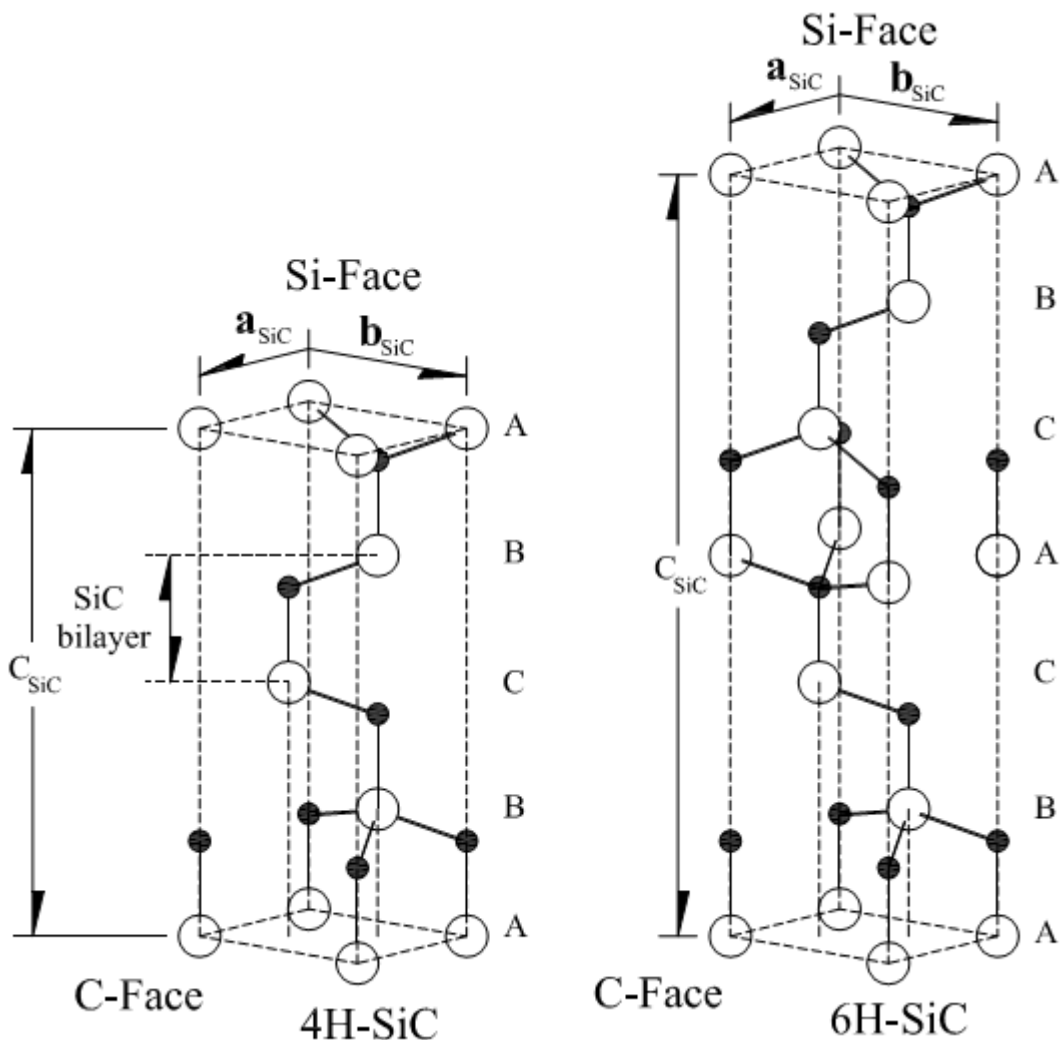


Figure 1.3. The unit cell structure of 4H and 6H SiC. Small and big circles represent carbon and silicon atoms, respectively. Reproduced by permission of IOP Publishing [1].

Silicon carbide (SiC) is a semiconductor with attractive properties such as wide band gap, high saturated electron mobility, high break-down electric field, good chemical and thermal stability [11]. Since SiC is a polar crystal, SiC has 2 types of surface i.e. Si-terminated and C-terminated faces. SiC substrate that ends up with the Si layer is called Si-face SiC. Similarly, SiC substrate that ends up with the C layer is called C-face SiC. However, graphene formed on Si-face and C-face SiC substrates have different quality and thickness. For example, the graphene film on Si-face SiC has orderly orientation, i.e., the graphene layer stacking is almost AB stacking and orientation of each layer is same. On the other hand, the layer stacking of graphene film on C-face SiC has various orientations. In addition, if the SiC both faces (Si-face and C-face) are annealed under the same conditions (same annealing temperature, time and ambient pressure), the formation of graphene film on C-face SiC will be thicker than that on Si-face. Moreover, the buffer layer will appear only on Si-face SiC but it disappears on C-face SiC.

1.5 Growth of graphene on SiC by thermal decomposition in argon gas atmosphere.

The conventional growth of graphene on SiC is just annealing SiC substrate in UHV at graphitization temperature. Figure 1.4 (a) shows graphene morphology after annealing in UHV. The terrace width of graphene is very narrow around 200-500 nm. In 2009, Emtsev *et al.* tried to anneal Si-face SiC substrate under argon pressure [12]. They found that annealing under argon gas can reduce the graphene roughness. Figure 1.4 (b) shows the morphology of graphene on Si-face SiC (0001) after annealing the SiC substrate under argon gas pressure of 0.3 atm. The terraces of graphene film which was grown by annealing under argon gas are wider obviously than the sample which is annealed in UHV. Wider terraces on Ar-grown epitaxial graphene are attributed to the reduction of Si evaporation from the SiC substrate. The presence of a argon pressure can reduce Si evaporation because when Si atoms desorbed from the surface, the Si atoms have a possibility to crash with Ar atoms and reflect back to the surface. The reduction of Si evaporation increases time to improve the surface before graphitization. Emtsev et al also measure the structural and electronic properties of Ar-grown graphene layers by using low-energy electron

diffraction (LEED), photoelectron spectroscopy and Raman spectroscopy. They found that although the process of Ar-grown epitaxial graphene on Si-face SiC results in an improvement in surface morphology, all other properties such as orientation with respect to the substrate, electronic structure and charge carrier density remain unchanged as compared to vacuum-grown layers. Namely, the structure of epitaxial graphene on Si-face SiC is still $6\sqrt{3} \times 6\sqrt{3}$ and has orientation difference of 30 degree from the SiC substrate. For the electronic structure of Ar-grown graphene, Dirac point is still lower Fermi level owing to electron doping from the substrate. Although the electronic properties of both process (Ar-grown and UHV-grown) are same, Emtsev et al also show that electronic qualities (such as electron mobility) are different due to the difference in surface roughness. The improvement of electron mobility in Ar-grown graphene is shown in Table 1.2.

Emtsev and co-worker show that annealing SiC under only high pressure of Ar gas (~900 mbar). This process can give us only graphene film with large domain and low roughness. In this thesis, we show the dependence of small graphene shape on inert gas pressure and annealing temperature. The SiC substrate will be annealed under various inert gas pressures and annealing temperature. Shape of small graphene with ring-shape, triangle-shape and stripe-shape will be shown clearly by using Atomic force microscopy (AFM) and scanning electron microscope (SEM). In addition, this process can keep intact edge of the small graphene due to the bottom-up growth. It is different from the growth of small graphene by cutting a large graphene sheet that destroys the graphene edge.

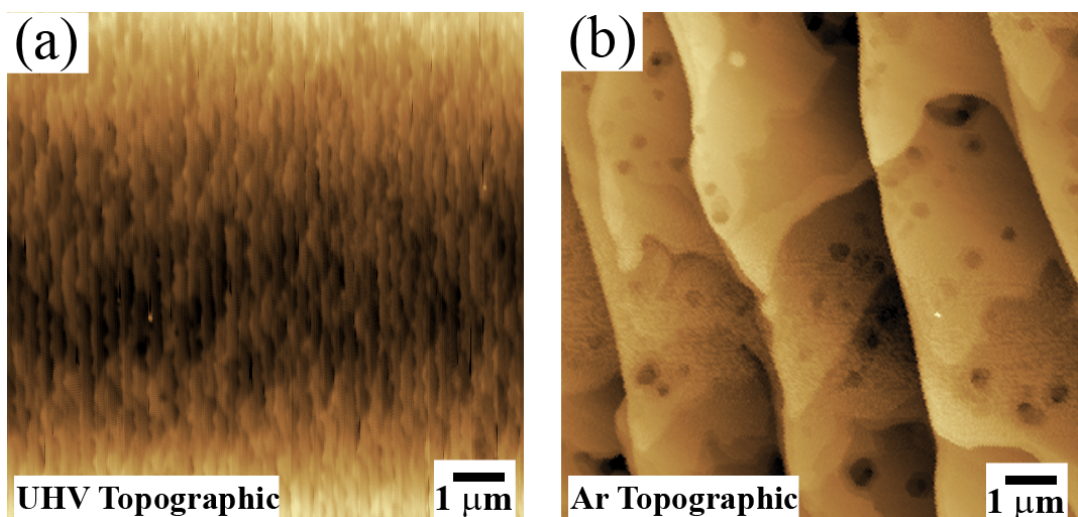


Figure 1.4. Morphology of graphene on SiC after annealing in (a) UHV and (b) argon pressure of 0.3 atm.

Table 1.2. electron mobilities (in $\text{cm}^2\text{V}^{-1}\text{s}^{-1}$) on UHV- and Ar-grown graphene measured at T= 300 and 27 K. This table is modified from [12]

Method	300 K	27 K
Ar	930	2000
UHV	550	710

1.6 Purpose of this study

This thesis is focus on the estimation of layer number of epitaxial graphene on SiC substrate and the growth of graphene on Si-terminated and C-terminated SiC by annealing the substrates under inert gas.

For the estimation of graphene layer number, there are many methods can be performed for determination of graphene layer number such as Auger electron spectroscopy (AES), X-ray photoelectron spectroscopy (XPS), angle-resolved photoemission spectroscopy (ARPES), surface X-ray diffraction (SXRD), scanning electron microscope (SEM) and low-energy electron microscope (LEEM). In the case of AES and XPS, a creation of model of the sample structure (graphene on SiC) is required. Moreover, knowledge of the inelastic mean free path of electrons in graphene layer is needed. In fact, it is not easy to understand the realistic model of the sample and accurate value of the inelastic mean free path of electrons. Therefore, it is difficult to obtain accurate information about graphene layer number from these methods. For SXRD method, it is a useful method which can estimate the film thickness but the acquirement of the accurate surface information is complicated and takes a long time. For the layer number estimation by LEEM, many researchers recently believed that the estimation of graphene layer number from this method is reliable. The layer number is determined from the number of minima in the LEEM spectra. Nevertheless, there is nobody proved that this method give us accurate information or not.

In this thesis, we offer a simple and accurate method for determining the layer number of graphene on SiC by using X-ray diffraction. The layer estimation methods by SEM, ARPES and Raman are also performed to confirm

the accuracy of this estimation method of graphene layer number. Moreover, in this thesis, we have studied the growth of graphene on Si-terminate and C-terminate SiC. In the case of graphene on Si-terminated SiC, we demonstrate the growth of epitaxial graphene in various shapes such as embedded and protrusive graphene stripes, graphene rings, and graphene triangles

1.7 Outline of this thesis

In this thesis, I study on the growth and layer estimation of epitaxial graphene on 6H-SiC. Thickness (or layer number) of the epitaxial graphene film on SiC is estimated by X-ray diffraction technique. In addition, I also study the growth of embedded and protrusive graphene stripes, graphene rings and graphene triangles on 6H-SiC. The followings show outline of the study in this thesis.

In chapter 1, Introduction including graphene and SiC structure, history of graphene synthesis and graphene properties are written in this chapter. Moreover, the basic knowledge about the improvement of graphene quality by annealing SiC substrate under Ar gas atmosphere is also described.

In chapter 2, the basic knowledge such as analytical instruments and X-ray diffraction is written concisely to understand the instrument and principle clearly.

In chapter 3, the experimental procedure is thoroughly written including synthesis and characterization of graphene.

It is important to know the layer number of graphene film since the electronic properties of graphene depend on graphene film thickness. In chapter 4, the efficient method to determine graphene film thickness on 6H-SiC by using X-ray diffraction is demonstrated. I offer a simple and effective master equation to estimate graphene film thickness on 6H-SiC. The accuracy of the results is confirmed by ultra-high vacuum scanning electron microscope (UHV-SEM) and angle-resolved photoemission spectroscopy (ARPES).

In chapter 5, I anneal C-face 6H-SiC (000 $\bar{1}$) substrates under argon gas to produce epitaxial graphene films with average thickness of 3 monolayers on the substrate. I also characterize the surface structure and morphology by reflection high-energy electron diffraction (RHEED) and atomic force microscopy (AFM). Moreover, Raman mapping measurement reveals that the graphene layer has high uniformity in doping concentration and strains. After graphitization I found that the step height of SiC surface is lower than 9 nm and graphene grows continuously across these steps to form large domains. AFM phase images indicate that the SiC surface is completely covered by graphene.

In chapter 6, I find the growth of protrusive striped graphene on Si-face 6H-SiC (0001) by annealing the SiC substrate under Ar gas. This result shows a strong contrast against the epitaxial graphene on SiC substrate grown in UHV; the epitaxial graphene is embedded in SiC surface with bonds between graphene edge and Si or C atoms of SiC substrate. For the graphene grown in Ar, the graphene edge structures approach free standing graphene because there is no bonding between graphene edge and SiC substrate.

In chapter 7, I display the growth of graphene rings on Si-face 6H-SiC (0001) since graphene rings have many attractive properties such as high electromagnetic confinement. This property implies that graphene rings are suitable for applying to optical antennas. Moreover, this growth method can preserve the structure of ring edges intact unlike electron-beam lithographic methods.

References for chapter 1

- [1] J. Hass, W. A. de Heer, and E. H. Conrad, "The growth and morphology of epitaxial multilayer graphene," *J. Phys: Condens. Matter*, 20, 323202 (18 July 2008).
- [2] Andronico, Michael. "5 Ways Graphene Will Change Gadgets Forever", <http://news.yahoo.com/5-ways-graphene-change-gadgets-155243022.html>. (14 April 2014).

- [3] F. Varchon, R. Feng, J. Hass, X. Li, B. Ngoc Nguyen, C. Naud, P. Mallet, J.-Y. Veuillen, C. Berger, E. H. Conrad, and L. Magaud, “Electronic Structure of Epitaxial Graphene Layers on SiC: Effect of the Substrate”, 99, 126805 (2007)
- [4] K. S. Novoselov, A. K. Geim, S. V. Morozov, D. Jiang, Y. Zhang, S. V. Dubonos, I. V. Grigorieva and A. A. Firsov. “Electric Field Effect in Atomically Thin Carbon Films”, Science 306, 666.
- [5] D. R. Dreyer, R. S. Ruoff, C. W. Bielawski, “From Conception to Realization: An Historical Account of Graphene and Some Perspectives for Its Future”, Angew. Chem. Int. Ed. 49, 9336 (2010).
- [6] A. Ismach, C. Druzgalski, S. Penwell, A. Schwartzberg, M. Zheng, A. Javey, J. Bokor, Y. Zhang, “Direct chemical vapor deposition of graphene on dielectric surfaces”, Nano Lett. 10, 1542 (2010).
- [7] J. Tian, H. Cao, W. Wu, Q. Yu, Y. P. Chen, “Direct imaging of graphene edges: atomic structure and electronic scattering”, Nano Lett. 11, 3663 (2011).
- [8] L. Jiao, L. Zhang, X. Wang, G. Diankov, and H. Dai, “Narrow graphene nanoribbons from carbon nanotubes”, nature 458, 877 (2009).
- [9] J. S. Moon, D. Curtis, M. Hu, D. Wong, C. McGuire, P. M. Campbell, G. Jernigan, J. L. Tedesco, B. VanMil, R. Myers-Ward, C. Eddy, Jr., and D. K. Gaskill, “Epitaxial-Graphene RF Field-Effect Transistors on Si-Face 6H-SiC Substrates,” IEEE electron device Lett., 30, 650 (2009).
- [10] P. Liu, W. Cai, L. Wang, X. Zhang, J. Xu, Tunable terahertz optical antennas based on graphene ring structures, Appl. Phys. Lett. 100, 153111 (2012).
- [11] W. Voegeli, “Structure and initial oxidation of the SiC (0001) surface”, Ph.D thesis, Department of Quantum Engineering, Nagoya University, (2007).
- [12] K. V. Emtsev et al., “Towards wafer-size graphene layers by atmospheric pressure graphitization of silicon carbide”, Nature Mat. 8, 203 (2009).

Chapter 2

Experimental Method

2.1 Basic principle of analytical methods

2.1.1 Atomic force microscopy

AFM Topographic image

Atomic force microscopy (AFM) is a type of microscopy which can show the resolution on the order of nanometer. The AFM consists of a laser beam, cantilever and position detector (as shown in Figure 2.1). The force between the tip and the sample is given from the Hooke's law

$$F = -kz, \quad (\text{eq. 2.1})$$

where

F is the force;

k is stiffness of the cantilever;

and z is the distance from equilibrium point of cantilever.

The AFM can measure morphology by maintaining a constant force. Moreover, AFM can distinguish the materials which have different viscosity and hardness by using phase imaging.

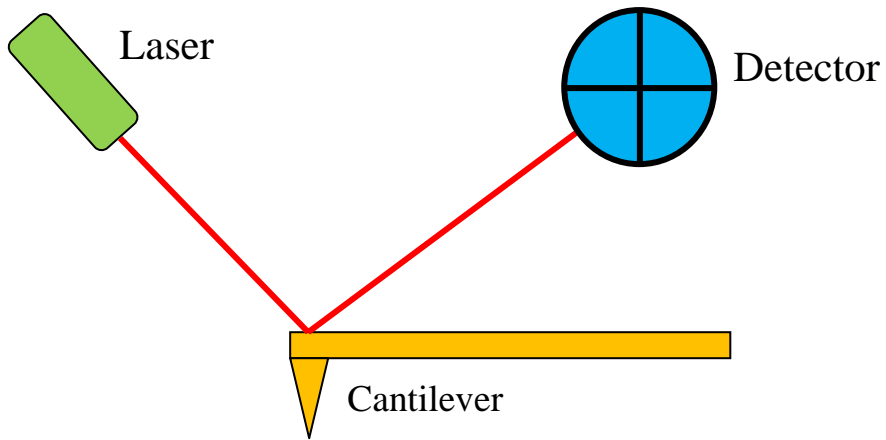


Figure 2.1. Systematic setup of AFM components.

AFM Phase image

For our experiments, SPM-9600 AFM which purchased from Shimadzu Corporation is carried out. AFM tapping mode is set up in this instrument. AFM phase imaging is a function in tapping mode of AFM. Therefore, it is possible to measure the morphology and phase image at same position and time. Phase imaging is created from the phase shift of the oscillating cantilever. The phase shift is originated from a delay in oscillation of the cantilever as shown in Figure 2.2. This delay is correlative with the viscosity and hardness of the material. Therefore, AFM phase imaging can distinguish materials on the sample surface. Figure 2.3 shows an example of phase image. This image displays two different contrasts (bright and dark brown) revealing there are 2 types of material. These two types of material are proved in Chapter 4, these are graphene (bright regions) and buffer layer (dark regions). In this thesis, we use the phase imaging to distinguish the graphene material from the buffer layer and SiC substrate.

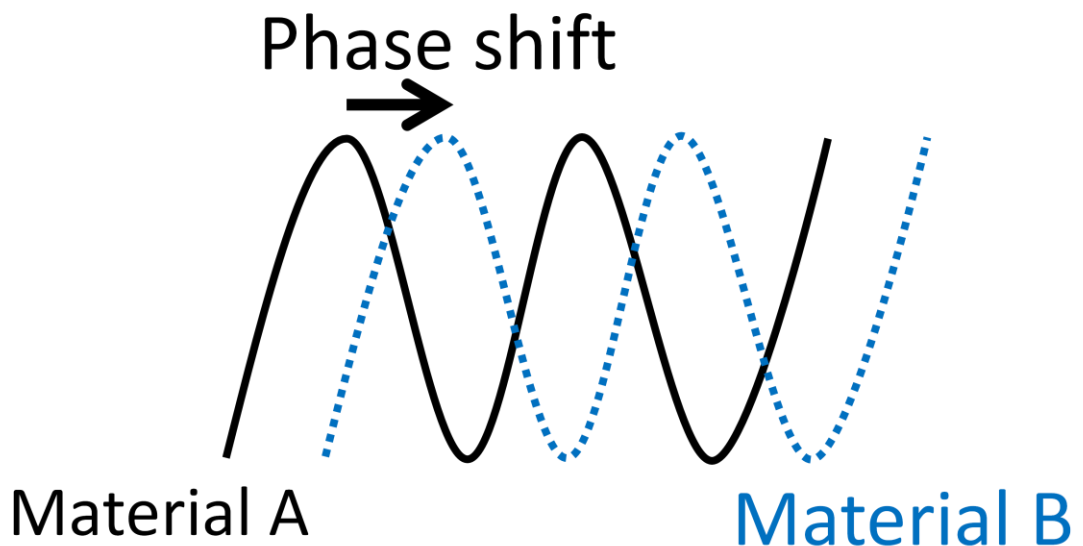


Figure 2.2. Phase shift originated from delay of cantilever when it measured on the different material.

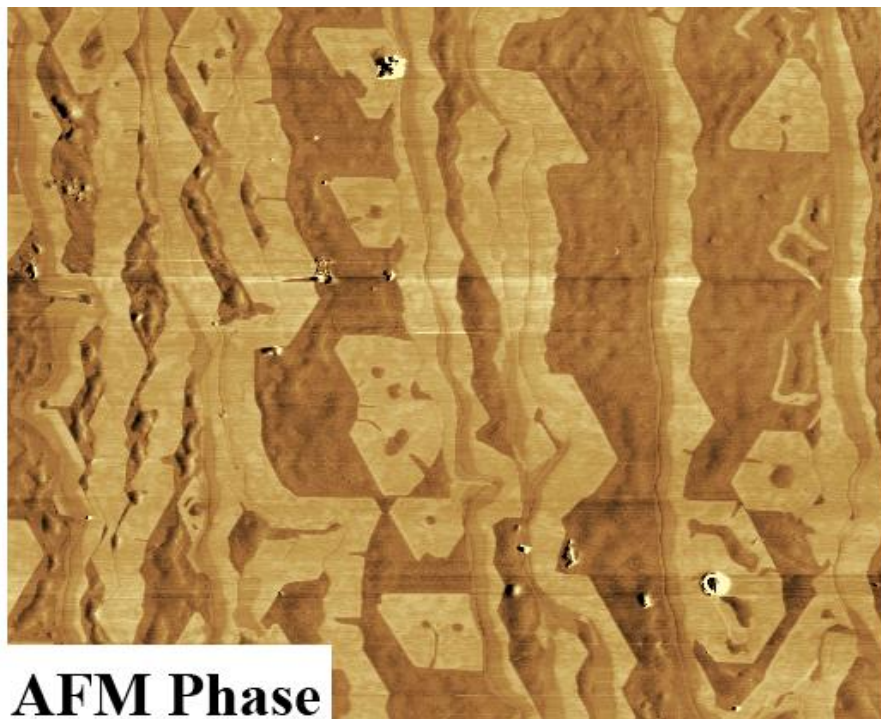


Figure 2.3. $10 \times 10 \mu\text{m}^2$ AFM phase image measured on the sample which contains graphene on SiC substrate.

2.1.2 Angle resolved photoemission spectroscopy

Angle resolved photoemission spectroscopy (ARPES), also known as ARUPS (angle-resolved ultraviolet photoemission spectroscopy), is an experimental technique for observing the energy dispersion of the electrons. ARPES makes use of the photoelectric effect by striking a monochromatized ultraviolet on a sample surface and counting the photoelectrons which leave the surface by an electron energy analyzer. This analyzer can measure the kinetic energy (E_{kin}) of electrons emitted into a given direction. Using the kinetic energy, we can estimate the wave vector of the electron in the matter in the extended scheme by

$$K_x = \frac{1}{\hbar} \sqrt{2mE_{kin}} \sin \vartheta \cos \phi$$

$$K_y = \frac{1}{\hbar} \sqrt{2mE_{kin}} \sin \vartheta \sin \phi$$

$$K_z = \frac{1}{\hbar} \sqrt{2m(E_{kin} + \varphi)} \cos \vartheta , \quad (\text{eq. 2.2})$$

where ϑ and ϕ are the polar and azimuthal emission angles (as shown in Figure 2.4), m is electron mass, φ is the work function and \hbar is the Planck constant divided by 2π .

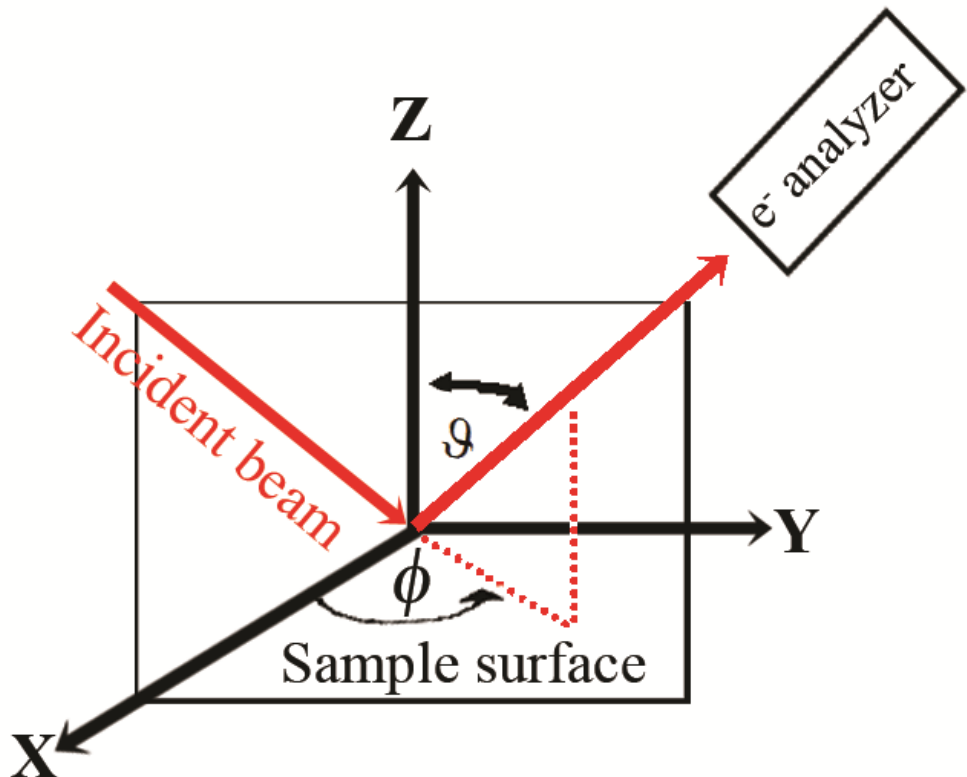


Figure 2.4. Experimental setup of ARPES.

2.1.3 Reflection high-energy electron diffraction

Reflection high-energy electron diffraction (RHEED) is a technique for examining the surface of materials. A RHEED system consists of electron source (electron gun), detector screen and the clean surface sample, as shown in Figure 2.5. The incident electron beam from the electron gun approaches the sample at small angle θ . Then the diffracted electrons reach the detector screen and form a diffraction pattern.

Azimuthal angle is an angle between the direction of an incident electron beam and the ordered crystal lattice direction (Figure 2.6 shows an example of RHEED scans at the azimuthal angle difference of 90 degrees). The most RHEED system is equipped with a sample holder that can rotate the sample around the surface perpendicular axis. The RHEED scan has to carry out at least 2 different azimuthal angles for the reliable characterization of a crystal structure.

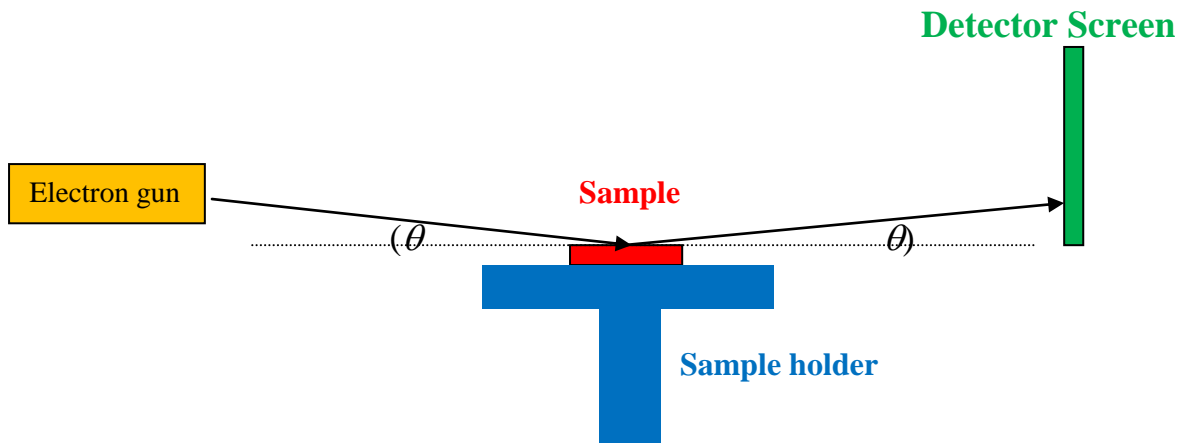


Figure 2.5. Systematic setup of RHEED components.

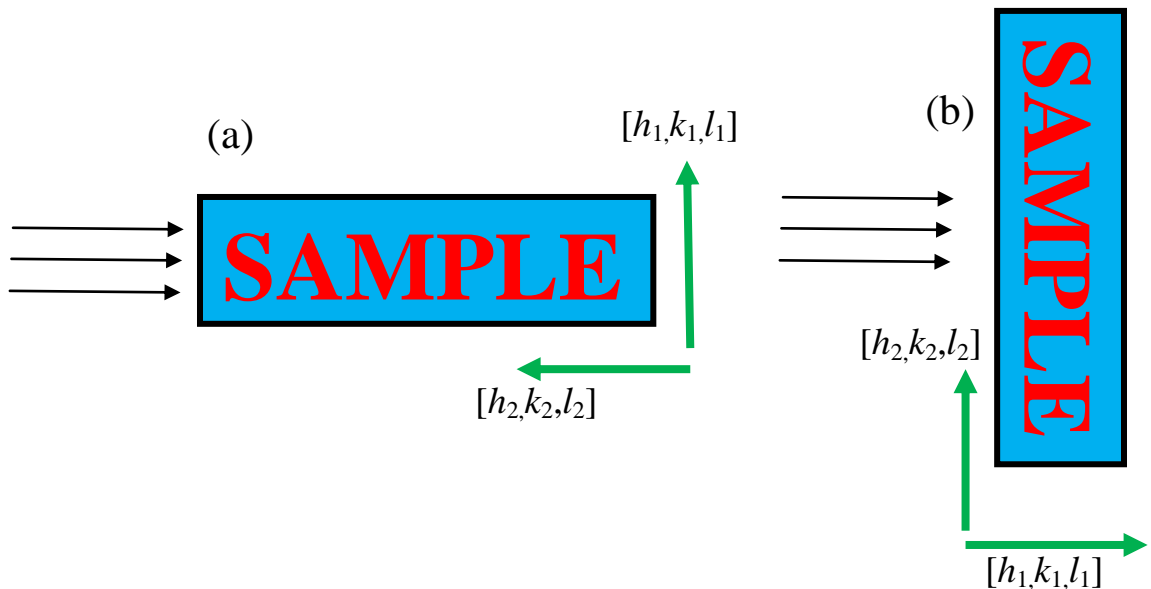


Figure 2.6. The electron beam incidents on the sample surface at a different azimuthal angle of 90 degrees.

2.1.4 X-ray diffraction

X-ray diffraction (XRD) is a non-destructive technique that reveals the crystallographic structure. The simple XRD system requires an X-ray source,

detector and clean surface sample as shown in Figure 2.7 (a). The diffraction will occur when Bragg's condition (see below) is satisfied. XRD profiles can give us the information about interlayer spacing by calculation from the Bragg's equation.

When an X-ray beam shines on the sample surface, the atoms on the surface play the part of scattering centers and emit scattered x-ray waves. The intensity of the scattered wave relates to the phase difference. If the phase difference is not equal to integer multiple of wavelength, the scattered wave will be absent due to the cancelation of each scattered wave. Therefore the scattered wave appear only in the case of phase difference is equal to integer multiple of wavelength. Figure 2.7 (b) shows the path difference = $\overline{AB} + \overline{BC} = 2d\sin\theta$. Hence the reflected wave occurs when

$$2d\sin\theta = n\lambda \quad (\text{Bragg's equation}) \quad (\text{eq. 2.3})$$

where n is an integer, λ is an X-ray wavelength, d is a lattice spacing perpendicular to the surface and θ is the angle between the incident beam and the scattering planes.

In this thesis, the XRD is employed to study the SiC (0001) spacing, interface-graphene and graphene-graphene spacing. The XRD profiles will be calculated for graphene thickness estimation.

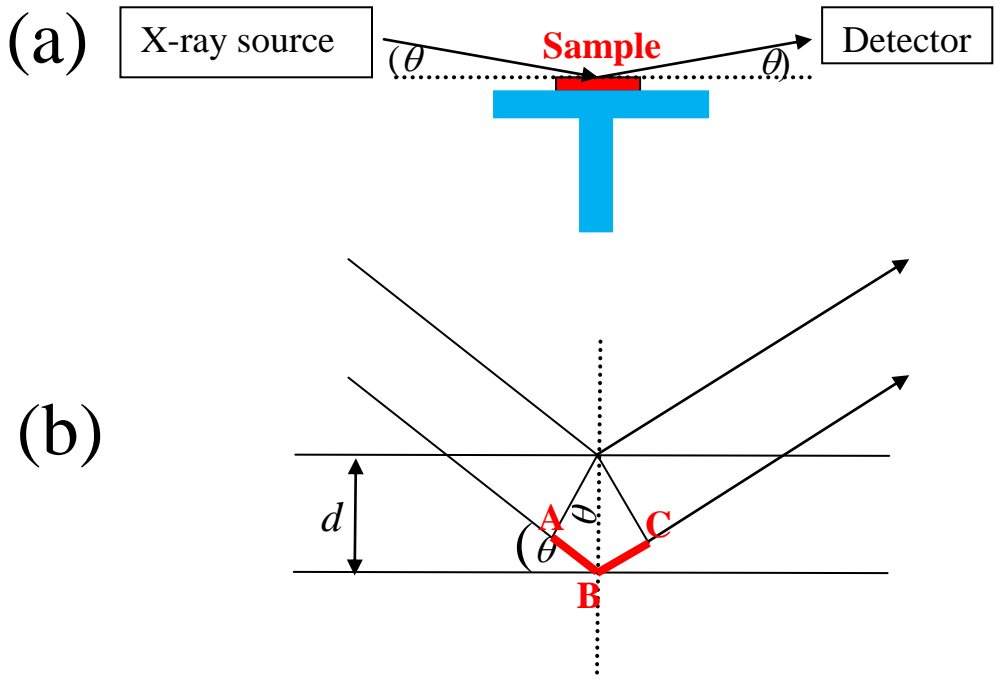


Figure 2.7. Schematic of a setup of XRD (a) and diffraction on the sample surface (b).

2.2 Basic principle for X-ray diffraction

X-rays is a name of electromagnetic radiation which has a wavelength in the range of 0.01 to 10 nm. X-ray diffraction is a common technique to study the crystal structures of solids. In this thesis, X-ray diffraction technique is used to determine layer spacing and graphene film thickness on 6H-SiC (0001). In this section we describe the intensity of X-ray diffraction at observation point from the fundamental concept. The major contents in this section are made brief and modified from Ref [14].

2.2.1 Classic scattering from a free electron

When the monochromatic X-rays shine on a sample, atoms on the sample will scatter the beam. In this section we consider the scattering of X-ray by a free electron. For the classic scattering, when an X-ray beam hits an atom, an

electric field from the X-ray beam will force an electron to move with acceleration. The movement of an electron with acceleration releases electromagnetic wave which has a same frequency as the incident radiation.

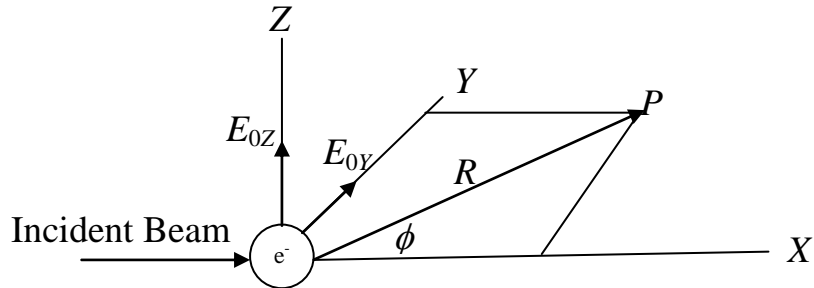


Figure 2.8 Classical scattering by a free electron

Figure 2.8 shows a schematic of classical scattering by a free electron. When an X-ray incident beam hits the electron, the instantaneous values of the electric fields in y and z components at the position of the electron are

$$\varepsilon_{0Y} = E_{0Y} \sin 2\pi \nu t, \quad \varepsilon_{0Z} = E_{0Z} \sin 2\pi \nu t \quad (\text{eq. 2.4})$$

where, E_{0Y} and E_{0Z} are amplitude of electric field of the incident beam in y and z components, respectively. ν is frequency of incident beam. t is time. After the beam hit the electron, the electron is moved by the force from the above electric field with acceleration of

$$a_y = \frac{f_y}{m} = \frac{eE_{0Y}}{m} \sin 2\pi \nu t \quad (\text{eq. 2.5})$$

$$a_z = \frac{f_z}{m} = \frac{eE_{0Z}}{m} \sin 2\pi \nu t \quad (\text{eq. 2.6})$$

From the electromagnetic theory, the electric field (ε) at point P can be calculated by

$$\varepsilon = \frac{q a \sin \alpha}{c^2 R} \quad (\text{eq. 2.7})$$

where, c is velocity of light, a is electron acceleration, R is distance from electron to point P . α is an angle between a and R .

In the case of y -component with acceleration of $a_y = \frac{eE_{0Y}}{m} \sin 2\pi \nu t$, the electric field (ε) at point P is given by

$$\varepsilon_Y = \frac{e^2 E_{0Y}}{mc^2 R} \sin 2\pi \nu t \cos \phi. \quad (\text{eq. 2.8})$$

In a similar process, the electric field (ε) at point P in the z -component is given by

$$\varepsilon_Z = \frac{e^2 E_{0Z}}{mc^2 R} \sin 2\pi \nu t. \quad (\text{eq. 2.9})$$

The amplitudes of electric field (ε) at point P for the both components are

$$E_Y = \frac{e^2 E_{0Y}}{mc^2 R} \cos \phi \quad (\text{eq. 2.10})$$

$$E_Z = \frac{e^2 E_{0Z}}{mc^2 R}. \quad (\text{eq. 2.11})$$

Therefore, the resultant amplitude E at the point P is

$$E^2 = E_Z^2 + E_Y^2 = \frac{e^4}{m^2 c^4 R^2} (E_{0Z}^2 + E_{0Y}^2 \cos^2 \phi). \quad (\text{eq. 2.12})$$

Since the electric vector from the incident beam takes with equal probability in all orientations in the YZ -plane, i.e.,

$$\langle E_{0Y}^2 \rangle = \langle E_{0Z}^2 \rangle. \quad (\text{eq. 2.13})$$

Considering the averages

$$\langle E_{0Y}^2 \rangle + \langle E_{0Z}^2 \rangle = \langle E_0^2 \rangle, \quad (\text{eq. 2.14})$$

We have

$$\langle E_{0Y}^2 \rangle = \langle E_{0Z}^2 \rangle = \frac{1}{2} \langle E_0^2 \rangle. \quad (\text{eq. 2.15})$$

Therefore,

$$\langle E^2 \rangle = \frac{e^4}{m^2 c^4 R^2} \left(\frac{1}{2} \langle E_0^2 \rangle + \frac{1}{2} \langle E_0^2 \rangle \cos^2 \phi \right) \quad (\text{eq. 2.16})$$

$$\langle E^2 \rangle = \langle E_0^2 \rangle \frac{e^4}{m^2 c^4 R^2} \left(\frac{1+\cos^2 \phi}{2} \right). \quad (\text{eq. 2.17})$$

We can calculate the intensity at point P by using the following equation

$$I = \frac{c}{8\pi} \langle E^2 \rangle. \quad (\text{eq. 2.18})$$

After the substitution of $\langle E^2 \rangle$, the intensity at the point P is given by

$$I = \frac{c}{8\pi} \langle E_0^2 \rangle \frac{e^4}{m^2 c^4 R^2} \left(\frac{1+\cos^2 \phi}{2} \right) \quad (\text{eq. 2.19})$$

$$I = I_0 \frac{e^4}{m^2 c^4 R^2} \left(\frac{1+\cos^2 \phi}{2} \right) \quad (\text{eq. 2.20})$$

where $I_0 = \frac{c}{8\pi} \langle E_0^2 \rangle$. The factor $\left(\frac{1+\cos^2 \phi}{2} \right)$ is called the polarization factor.

2.2.2 Scattering from several electrons

In the previous section we showed the scattering by a free electron. In this section, we consider the case of the scattering from many electrons. Figure 2.9 shows the condition of a plane wave shines on the electrons (circle). The scattering takes place from the electrons to observation point P .

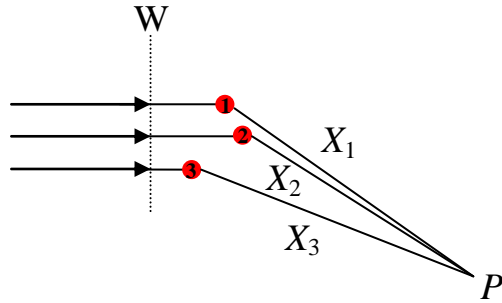


Figure 2.9 Scattering of a plane incident beam by many electrons. Circles represent scattering electrons. The integer numbers (1, 2, 3, ..., n) in circles indicate the number of scattering electrons. X_1 , X_2 , X_3 , ..., X_n are the total distances between wave front W to the point P .

The instantaneous value of the electric field at point P in each scattered wave is given by

$$\varepsilon_n = E_n \cos \left(2\pi v t - \frac{2\pi X_n}{\lambda} \right), \quad (\text{eq. 2.21})$$

where ν is the frequency, λ is the wavelength and E_n is the amplitude from each scattering electron. If we expanded the equation, we can obtain

$$\varepsilon_n = E_n \left(\cos(2\pi\nu t) \cos\left(\frac{2\pi X_n}{\lambda}\right) + \sin(2\pi\nu t) \sin\left(\frac{2\pi X_n}{\lambda}\right) \right). \quad (\text{eq. 2.22})$$

Therefore, the resultant instantaneous electric field at point P is

$$\varepsilon = \sum \varepsilon_n = \cos(2\pi\nu t) \sum E_n \cos\left(\frac{2\pi X_n}{\lambda}\right) + \sin(2\pi\nu t) \sum E_n \sin\left(\frac{2\pi X_n}{\lambda}\right). \quad (\text{eq. 2.23})$$

Let

$$\sum E_n \cos\left(\frac{2\pi X_n}{\lambda}\right) = E \cos \phi \quad (\text{eq. 2.24})$$

$$\sum E_n \sin\left(\frac{2\pi X_n}{\lambda}\right) = E \sin \phi, \quad (\text{eq. 2.25})$$

And hence

$$\varepsilon = \cos(2\pi\nu t) E \cos \phi + \sin(2\pi\nu t) E \sin \phi \quad (\text{eq. 2.26})$$

$$\varepsilon = E \cos(2\pi\nu t - \phi). \quad (\text{eq. 2.27})$$

2.2.3 Scattering by an atom

In the case of scattering from many electrons (previous case), we know the instantaneous value of the electric field is

$$\varepsilon_n = E_n \cos\left(2\pi\nu t - \frac{2\pi X_n}{\lambda}\right). \quad (\text{eq. 2.28})$$

We have already proven (in the case of scattering by a free electron) that after a free electron was accelerated, E_n equals to $\frac{e^2 E_0}{mc^2 R}$. Therefore, the instantaneous value of the electric field becomes

$$\varepsilon_n = \frac{e^2 E_0}{mc^2 R} \cos\left(2\pi\nu t - \frac{2\pi X_n}{\lambda}\right). \quad (\text{eq. 2.29})$$

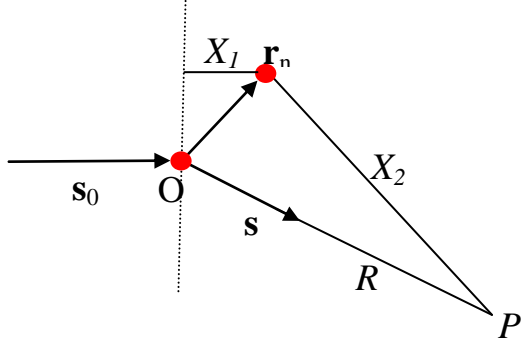


Figure 2.10 Scattering of a group of electron around an atom

In this case we consider the scattering by an atom. The distances from atom to electrons have to be considered. Figure 2.10 shows the scattering of this condition. The incident beam with amplitude E_0 hits an atom at point O. \mathbf{r}_n represents the position of each electron related to the atom. X_1 , X_2 and R are the distance between wave front-electron, electron-point P and atom-point P , respectively. \mathbf{s}_0 and \mathbf{s} are unit vectors pointing to incident beam and R direction, respectively.

The total path from wave front to point P is X_1+X_2 . Therefore the instantaneous value of the electric field at point P is

$$\varepsilon = \sum \varepsilon_n = \sum \frac{e^2 E_0}{mc^2 X_2} \cos \left(2\pi \nu t - \frac{2\pi(X_1+X_2)}{\lambda} \right) \quad (\text{eq. 2.30})$$

Since $X_1 = \mathbf{r}_n \cdot \mathbf{s}_0$ and $X_2 = R - (\mathbf{r}_n \cdot \mathbf{s})$,

$$X_1+X_2 = \mathbf{r}_n \cdot \mathbf{s}_0 + R - (\mathbf{r}_n \cdot \mathbf{s}) = R - (\mathbf{s} - \mathbf{s}_0) \cdot \mathbf{r}_n. \quad (\text{eq. 2.31})$$

So,

$$\varepsilon = \sum \frac{e^2 E_0}{mc^2 X_2} \cos \left(2\pi \nu t - \frac{2\pi(R - (\mathbf{s} - \mathbf{s}_0) \cdot \mathbf{r}_n)}{\lambda} \right) \quad (\text{eq. 2.32})$$

is derived. Using exponential expression,

$$\varepsilon = \frac{e^2 E_0}{mc^2 X_2} \sum e^{i(2\pi \nu t - \frac{2\pi(R - (\mathbf{s} - \mathbf{s}_0) \cdot \mathbf{r}_n)}{\lambda})} \quad (\text{eq. 2.33})$$

$$\varepsilon = \frac{e^2 E_0}{mc^2 X_2} e^{i(2\pi \nu t - \frac{2\pi R}{\lambda})} \sum e^{i(\frac{2\pi(\mathbf{s} - \mathbf{s}_0) \cdot \mathbf{r}_n}{\lambda})}. \quad (\text{eq. 2.34})$$

Generally, the distance from the atom to the observation point P and that from electrons to the point P are approximately same ($X_2 \approx R$). Hence

$$\varepsilon = \frac{e^2 E_0}{mc^2 R} e^{i2\pi(\nu t - \frac{R}{\lambda})} \sum e^{i\frac{2\pi}{\lambda}((s - s_0) \cdot r_n)}. \quad (\text{eq. 2.35})$$

The term $\sum e^{i\frac{2\pi}{\lambda}((s - s_0) \cdot r_n)}$ is called atomic scattering factor.

2.2.4 Diffraction by graphene on SiC (0001)

In the previous section, we showed the instantaneous value of the electric field at point P by the diffraction from an atom. In this section, we focus on the intensity of the diffraction from the graphene on SiC (0001) at the observation point P . First, we consider an incident beam with intensity I_0 and wavelength λ shines on the graphene on Si-face 6H-SiC (0001). The conditions are demonstrated by Figure 2.11. The point O represents a crystal origin. The position of atom is indicated by vector $\mathbf{R}_m^n = m_1 \mathbf{a}_1 + m_2 \mathbf{a}_2 + m_3 \mathbf{a}_3 + \mathbf{r}_n$.

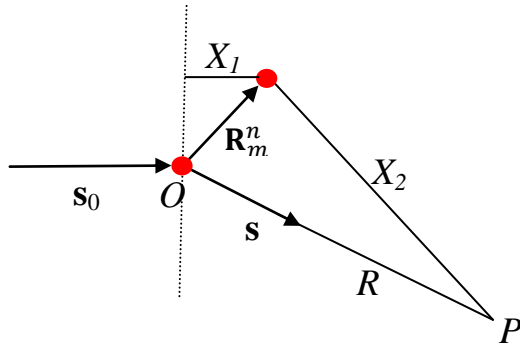


Figure 2.11 Diffraction by a small crystal

By modifying the instantaneous value of the electric field at point P by the diffraction from an atom (eq. 2.35), the instantaneous value of the electric field at point P by the diffraction from a small crystal is given by

$$\varepsilon_p = \frac{e^2 E_0}{mc^2 R} f_n e^{i2\pi(\nu t - \frac{R}{\lambda})} \sum e^{i\frac{2\pi}{\lambda}((s - s_0) \cdot \mathbf{R}_m^n)} \quad (\text{eq. 2.36})$$

where f_n is an atomic scattering factor. After substituted $\mathbf{R}_m^n = m_1\mathbf{a}_1 + m_2\mathbf{a}_2 + m_3\mathbf{a}_3 + \mathbf{r}_n$ we get

$$\varepsilon_p = \frac{e^2 E_0}{mc^2 R} f_n e^{i2\pi(\nu t - \frac{R}{\lambda})} \sum e^{i\frac{2\pi}{\lambda}((\mathbf{s}-\mathbf{s}_0) \cdot (m_1\mathbf{a}_1 + m_2\mathbf{a}_2 + m_3\mathbf{a}_3 + \mathbf{r}_n))} \quad (\text{eq. 2.37})$$

$$\begin{aligned} \varepsilon_p &= \frac{e^2 E_0}{mc^2 R} e^{i2\pi(\nu t - \frac{R}{\lambda})} \sum f_n e^{i\frac{2\pi}{\lambda}((\mathbf{s}-\mathbf{s}_0) \cdot \mathbf{r}_n)} \\ &\times \sum_{m_1=0}^{N_1-1} e^{i\frac{2\pi}{\lambda}((\mathbf{s}-\mathbf{s}_0) \cdot m_1\mathbf{a}_1)} \sum_{m_2=0}^{N_2-1} e^{i\frac{2\pi}{\lambda}((\mathbf{s}-\mathbf{s}_0) \cdot m_2\mathbf{a}_2)} \sum_{m_3=0}^{N_3-1} e^{i\frac{2\pi}{\lambda}((\mathbf{s}-\mathbf{s}_0) \cdot m_3\mathbf{a}_3)} \quad (\text{eq. 2.38}) \end{aligned}$$

The term of $\sum f_n e^{i\frac{2\pi}{\lambda}((\mathbf{s}-\mathbf{s}_0) \cdot \mathbf{r}_n)}$ is called structure factor (F). From the 3 Laue conditions

$$a_1 \cdot \Delta\mathbf{k} = h \quad (\text{eq. 2.39})$$

$$a_2 \cdot \Delta\mathbf{k} = k \quad (\text{eq. 2.40})$$

$$a_3 \cdot \Delta\mathbf{k} = l \quad (\text{eq. 2.41})$$

where $\Delta\mathbf{k} = \frac{1}{\lambda}(\mathbf{s} - \mathbf{s}_0)$ is the change between incident and scattered wave vectors. Since we are considering on the graphene film on SiC (0001) where Miller indices of h and k are zero, therefore the instantaneous value of the electric field can be reduced to

$$\varepsilon_p = \frac{e^2 E_0}{mc^2 R} e^{i2\pi(\nu t - \frac{R}{\lambda})} F N_1 N_2 \sum_{m_3=0}^{N_3-1} e^{i2\pi l m_3}, \quad (\text{eq. 2.42})$$

where N_3 is a number of graphene layer.

The intensity of the field at the observation point P is given by

$$I = \frac{c}{8\pi} \langle E^2 \rangle = \frac{1}{8\pi} \frac{e^4 E_0^2}{m^2 c^3 R^2} \left| e^{i2\pi(\nu t - \frac{R}{\lambda})} \right|^2 |F|^2 N_1^2 N_2^2 \left| \sum_{m_3=0}^{N_3-1} e^{i2\pi l m_3} \right|^2 \quad (\text{eq. 2.43})$$

$$I \propto \left(\frac{1+\cos^2 2\theta}{2} \right) |F|^2 \left| \sum_{m_3=0}^{N_3-1} e^{i2\pi l m_3} \right|^2, \quad (\text{eq. 2.44})$$

References for chapter 2

- [13] A Damascelli, Physica Scripta. 109, 61 (2004).
- [14] B.E. Warren, “X-ray diffraction”, Dover publication (1968), Inc., New York, Chapter from 1 to 3.

Chapter 3

Synthesis and Characterization of Epitaxial Graphene on 6H-SiC (0001)

3.1 Graphene synthesis

3.1.1 SiC single crystalline substrate

High-quality n-doped Si-terminated and C-terminated 6H-SiC substrates for our experiments were purchase from Crystal Base company with the sizes of $12 \times 3 \times 0.25$ mm and $25 \times 3 \times 0.235$ mm. All 6H-SiC substrates are polished one face from the company. The orientations of the Si-terminated and C-terminated 6H-SiC are (0001) and (000 $\bar{1}$), respectively. The degree of hardness, band gap and electronic conductivity of these 6H-SiC are 13, 3.93 eV and $0.076 \Omega/\text{cm}$, respectively.

3.1.2 Thermal treatment of SiC

Precleaning of a 6H-SiC substrate was carried out by ultrasonic in acetone for about 6 minutes. After acetone was evaporated, the substrate was immediately mounted on the sample holder and put to an exchange chamber (right part in Figure 3.1). After that, air in the exchange chamber is evacuated until the background pressure reaches $\sim 10^{-6}$ Pa. A gate valve between the exchange and the main chambers is opened followed by transferring the sample into the main chamber with the base pressure of $\sim 10^{-8}$ Pa by using a transfer rod. Then the gate valve is closed. Next, Si atoms from Si source are deposited on the substrate with the Si thickness of ~ 2 layers. Si deposition process is

expressed by a simple schematic in Figure 3.2. First, the filament is heated by applying an electrical current to emit electrons. Then, the emitted electrons are confined by electric field to strike the Si wafer. Some emitted Si atoms will deposit on the surface of SiC substrate. In the case of annealing the SiC substrate under UHV condition, the substrate is annealed in this main chamber. For annealing the SiC substrate under inert gas conditions, the substrate is transferred to the exchange chamber by the transfer rod again without exposure to air. After the transfer, the gate between both chambers is closed followed by inert gas introduction. The samples were named by using the gas type and value of gas pressure where they were annealed in. The sample is annealed by resistive heating method (Figure 3.3) where the sample is connected with 2 electrodes. The direct current (I) is flowed into the SiC substrate to increase the substrate temperature. The annealing temperature was in a range from ~ 900 °C to graphitization temperature in steps of approximately 100 °C. The annealing time was about 10-15 minutes per step to produce a few layered graphene. The annealing temperature is measured by detecting the thermal radiation from the sample using a pyrometer.

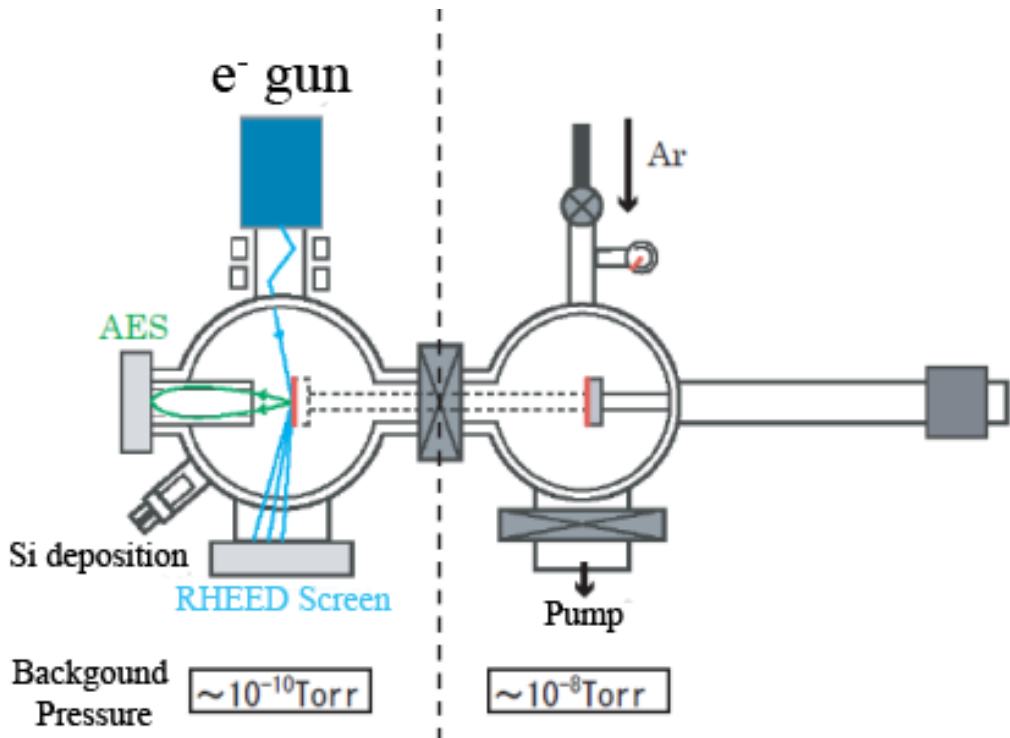


Figure 3.1. Experimental setup shows the whole view which consists of main (left part) and exchange (right part) chamber. The base of the pressure of the main and exchange chamber are $\sim 10^{-10}$ and $\sim 10^{-8}$ torr, respectively.

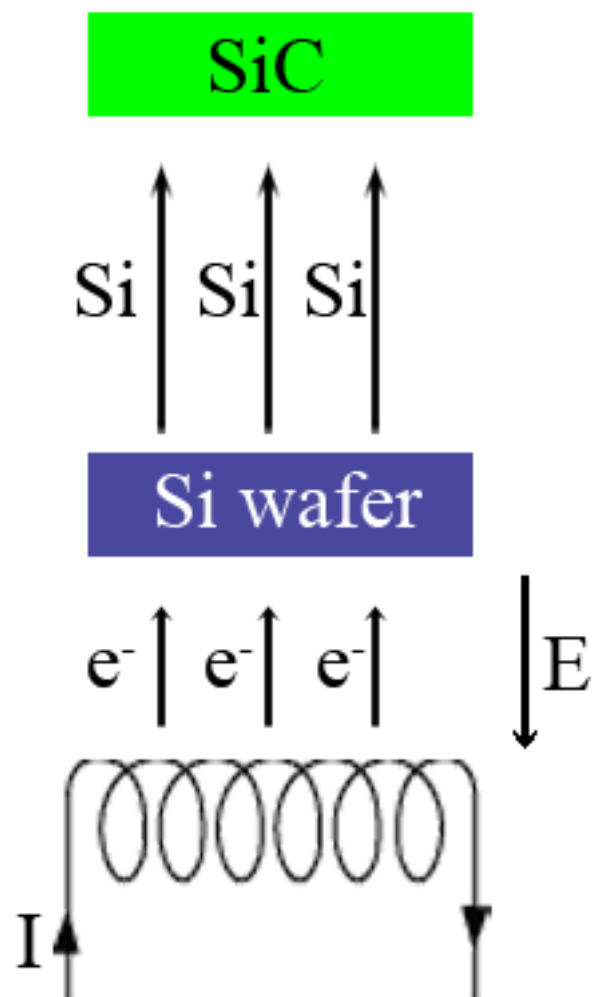


Figure 3.2. Schematic of Si deposition process.

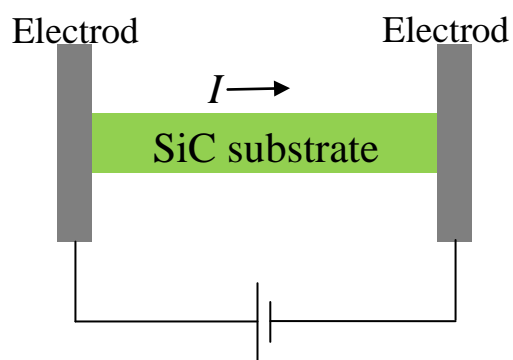


Figure 3.3. Schematic of resistive heating system.

3.2 Characterization of epitaxial graphene on 6H-SiC (0001)

3.2.1 Reflection high-energy electron diffraction (RHEED)

After annealing, the sample was transferred back to the main chamber by the transfer rod to measure the surface structure by RHEED which has an electron gun generating an incident electron beam with energy of 10kV hits on the sample surface with a small incident angle between beam and sample surface. The RHEED patterns which reveal the surface structure of the sample are projected onto the screen as shown in Figure 3.4. These RHEED patterns were recorded by a CCD camera. In order to measure RHEED patterns from different azimuths the sample can be rotated by rotating the manipulator on top.

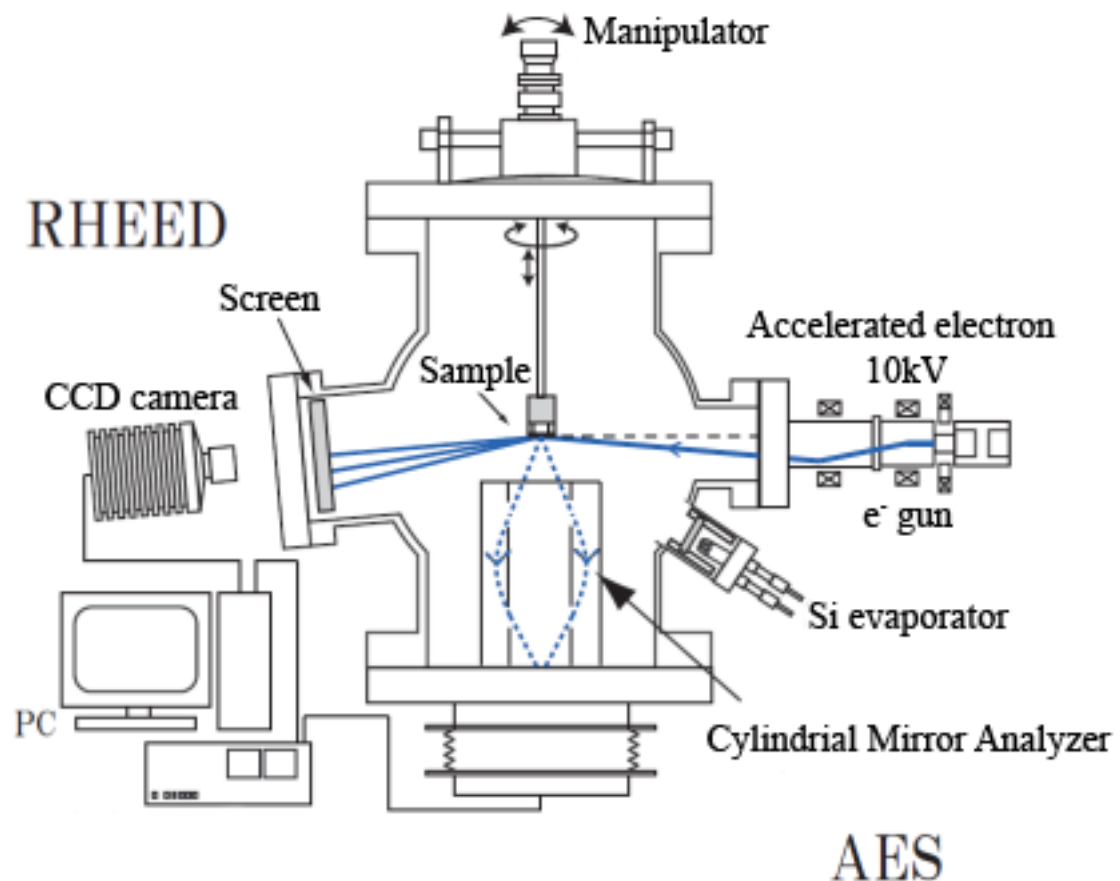


Figure 3.4. Schematic of systematic setup insides the main chamber.

3.2.2 Synchrotron X-ray diffraction (XRD)

An *ex-situ* XRD measurement is carried out at the beam line 4C, Photon Factory, KEK (Tsukuba, Japan). The sample is put on the sample holder which can move in horizontal and vertical directions. The sample holder also can be rotated around itself (r direction) and experimental circumference (R direction) as shown in Figure 3.5. In our experiment, an X-ray detector which can be rotated around experimental circumference (R direction) is performed to collect the diffracted X-ray. Diffraction data were collected at X-ray energy of 10.2 keV and incident beam size of 1 mm at room temperature.

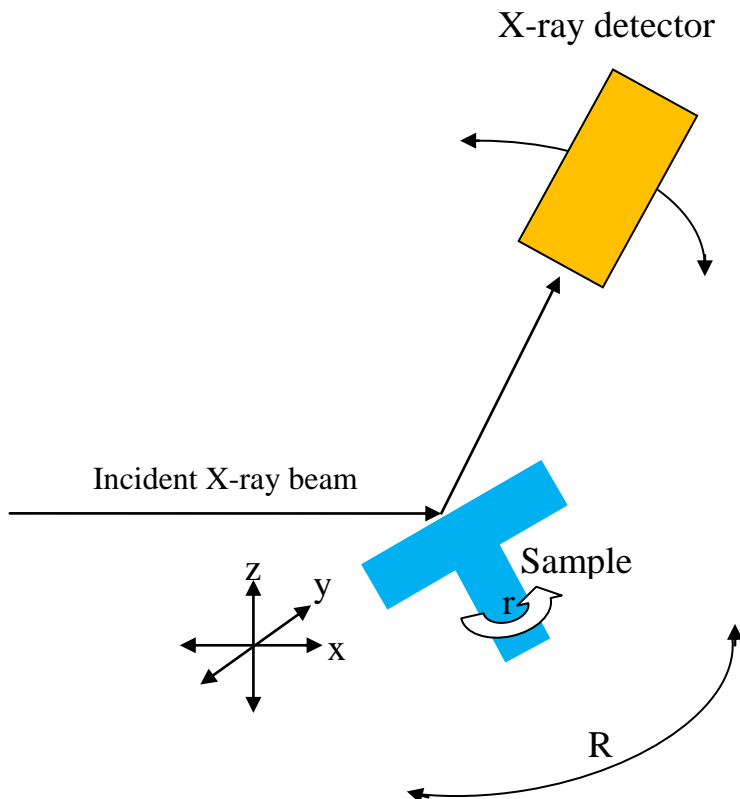


Figure 3.5. Schematic of X-ray diffraction system.

3.2.3 Angle-resolved photoemission spectroscopy (ARPES)

An ARPES measurement was conducted at room temperature at the beam line 5U of UVSOR-II in the Institute for Molecular Science, Okazaki, Japan. The excitation photon with energy of 80 eV shines on the sample. The emitted

valence electrons are collected and analyzed by lens and hemispherical analyzer as shown in Figure 3.6. Namely, after the sample was shined by ultraviolet, photoelectrons emit from the sample surface and are collected by a special lens. This lens can resolve the electron momenta, i.e., it can send electrons which have the same momenta to the same location at the exit aperture of the lens. Electrons with different momenta and energy will enter the entrance slit and go out of the exit slit of the hemispherical analyzer at different position. Figure 3.7 shows the electron path in the case of the two electrons which have same kinetic energy but different momenta. In addition, the hemispherical analyzer was applied by two different potential, V_1 and V_2 , at the inner and outer hemispherical to alter the electron's trajectory. Figure 3.8 show the path of photoelectron which contain a same momentum, inside the hemispherical analyzer. Fast electrons which contain high kinetic energy will follow a larger radius of circular trajectory (blue trajectory). On the other hand, slow electrons which contain lower kinetic energy will follow a small radius of the circular trajectory (red trajectory). Therefore the 3D mapping which contain momentum, kinetic energy and intensity of the photoelectrons can be created by this instrument.

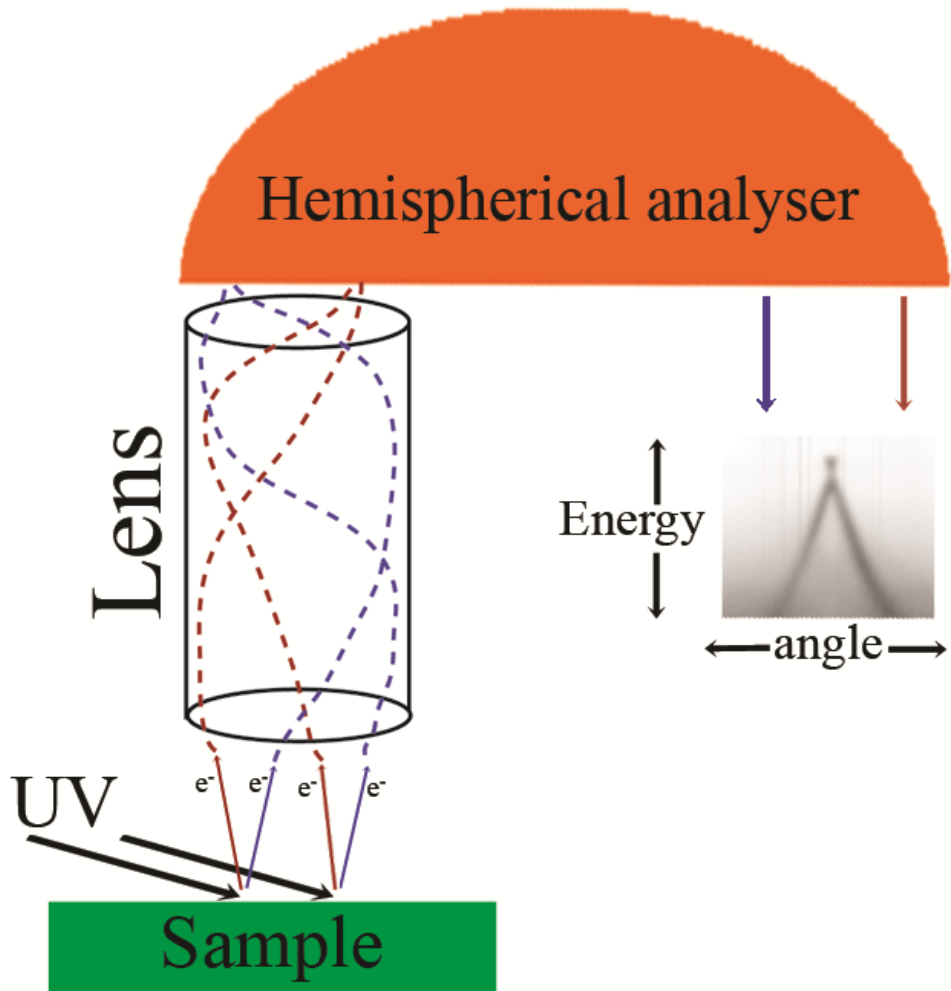


Figure 3.6. Schematic of angle-resolved photoemission spectroscopy system

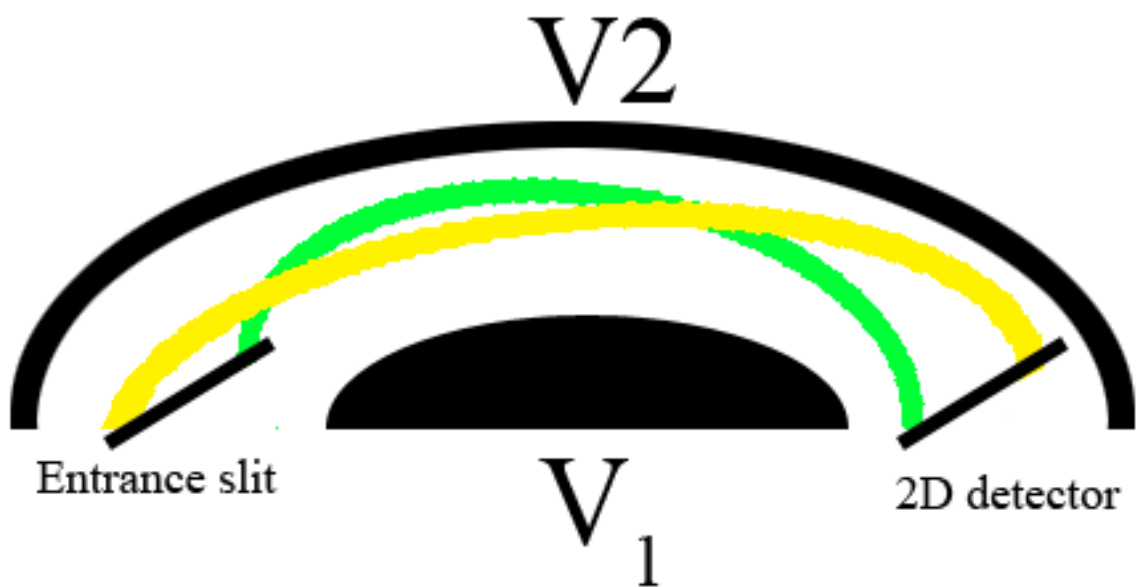


Figure 3.7 Schematic of electron path inside the hemispherical detector in the case of same kinetic energy but different momentum.

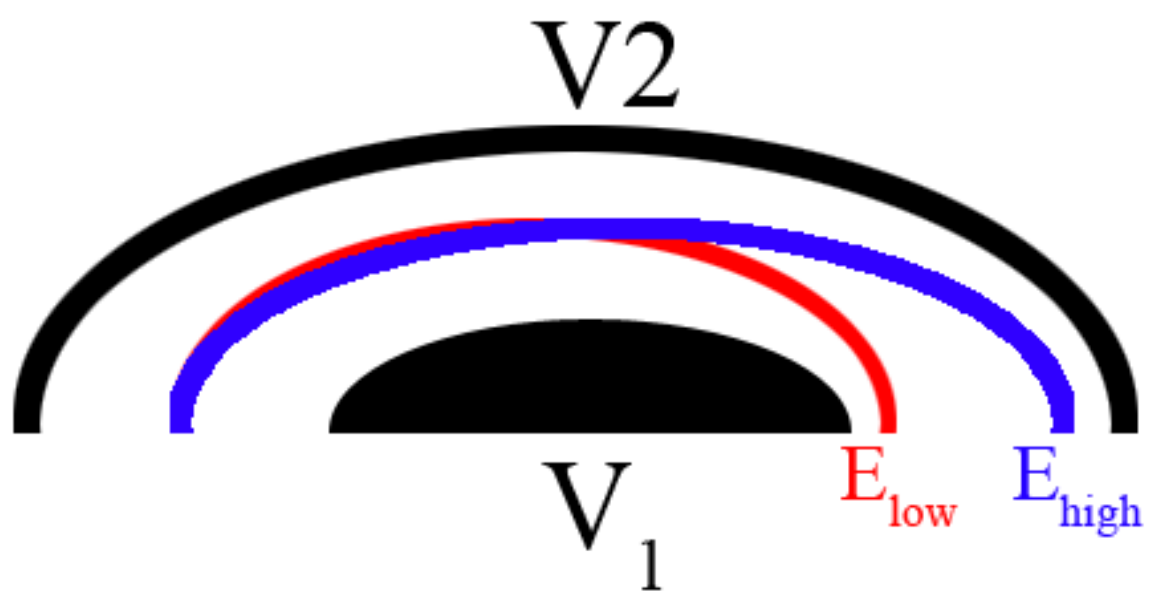


Figure 3.8. Schematic of electron path inside the hemispherical detector.

Chapter 4

Graphene Film Thickness Estimation by X-ray Diffraction (XRD)

The estimation of the graphene film thickness on SiC substrate is vitally important since the properties of graphene depend on its thickness. In general, there are several techniques, such as scanning electron microscope (SEM) [17], Auger electron spectroscopy (AES) [18, 19], X-ray photoelectron spectroscopy (XPS) [20], attenuation of substrate Raman intensity [20], angle-resolved photoemission spectroscopy (ARPES) [15] and surface X-ray diffraction (SXRD) [21, 22] to determine the layer number of graphene grown on SiC. For the AES and XPS, the thickness determination relies on the Si/C intensity ratio and the model which assumes that graphene is grown uniformly on SiC substrate. Their accuracy could suffer from the unrealistic model and the inaccurate knowledge of the inelastic mean free path of electrons [18-20, 23]. In the case of the estimation by attenuation of substrate Raman intensity, the accuracy depends on the Raman intensity of SiC which varies in position. In the case of ARPES, it can reveal the graphene band structure which implies only the combination of graphene layer but not respective coverages. Low accelerating voltage SEM is a technique which can locally distinguish the relative graphene thickness regions by difference in contrast but it cannot exhibit the absolute graphene thickness unless contrast-thickness relation for each sample is obtained. The SXRD is a wonderful method which can estimate the film thickness. Charrier et al. demonstrates the determination of graphene thickness by using SXRD [24]. They measured the structure factor along the graphite rod versus the l (coordinate in the reciprocal space) and then fit a simulated Structure factor to the experimental data. Since the Structure factor at each l obtains by calculation from a rocking scan (intensity Vs diffraction angle θ measurement), it is take time to obtain the data of rocking scan for all l . In addition, the simulation for fitting the structure factor data is complicate. Therefore the acquirement of the accurate surface information by using the

SXRD method is more complicated and takes a long time than our XRD method which uses a simple equation and takes a few minute to obtain experiment XRD data.

In this chapter, we have determined the layer thickness of non-uniform graphene on SiC substrate by the X-ray diffraction (XRD). The surface information, such as layer spacing and the graphene thickness distribution, is obtained by using a simple equation. The results are also confirmed by ARPES and ultra-high vacuum scanning electron microscope (UHV-SEM).

4. 1 Experimental

N-type Si-terminated 6H-SiC (0001) substrates were first deposited by silicon about 2 layers then annealed under argon gas with a pressure of 0.05, 0.3 and 0.5 atm. The annealing temperature was in a range from ~900 °C to graphitization temperature (1550 °C for the 0.05 atm sample, 1675 °C for the 0.3 atm sample and 1700 °C for the 0.5 atm sample) with increasing temperature by ~100 °C. The annealing time was about 10-15 minutes at each temperature to produce a few layered graphene. The sample heating was carried out by direct current through the sample. The samples were named as the value of argon pressure where they were annealed in and their graphitization temperature; e.g. 0.05 atm 1550 °C sample means a SiC substrate was annealed under argon pressure of 0.05 atm at graphitization temperature of 1550 °C.

After annealing, an *ex-situ* XRD measurement was carried out at the beam line 4C, Photon Factory, KEK (Tsukuba, Japan). Diffraction data were collected at X-ray energy of 10.2 keV and incident beam size of 1 mm at room temperature. An ARPES measurement was also conducted at room temperature at the beam line 5U of UVSOR-II in the Institute for Molecular Science, Okazaki, Japan. The excitation photon energy was set to 80 eV. An Ultra-High Vacuum (UHV)-SEM (Omicron Nano Technology) observation with incident beam of 1.7-2.2 keV was also carried out.

4.2 Thickness estimation by XRD method

For demonstrating the graphene film thickness estimation by XRD methods, we choose samples which annealed under argon pressure of 0.05, 0.3 and 0.5 atm with graphitization temperature of 1550 °C, 1675 °C, 1700 °C, respectively. Figure 4.1 shows XRD profiles of (a) 0.05 atm 1550 °C sample, (b) 0.3 atm 1650 °C sample and (c) 0.5 atm 1700 °C sample. As indicated in the figure, diffraction peaks of graphene and SiC are observed at ~20 ° and 27.8 °, respectively. The d -spacings can be calculated from the peak position using Bragg's equation. In this experiment, the X-ray wavelength (λ) of 1.21553 Å is used.

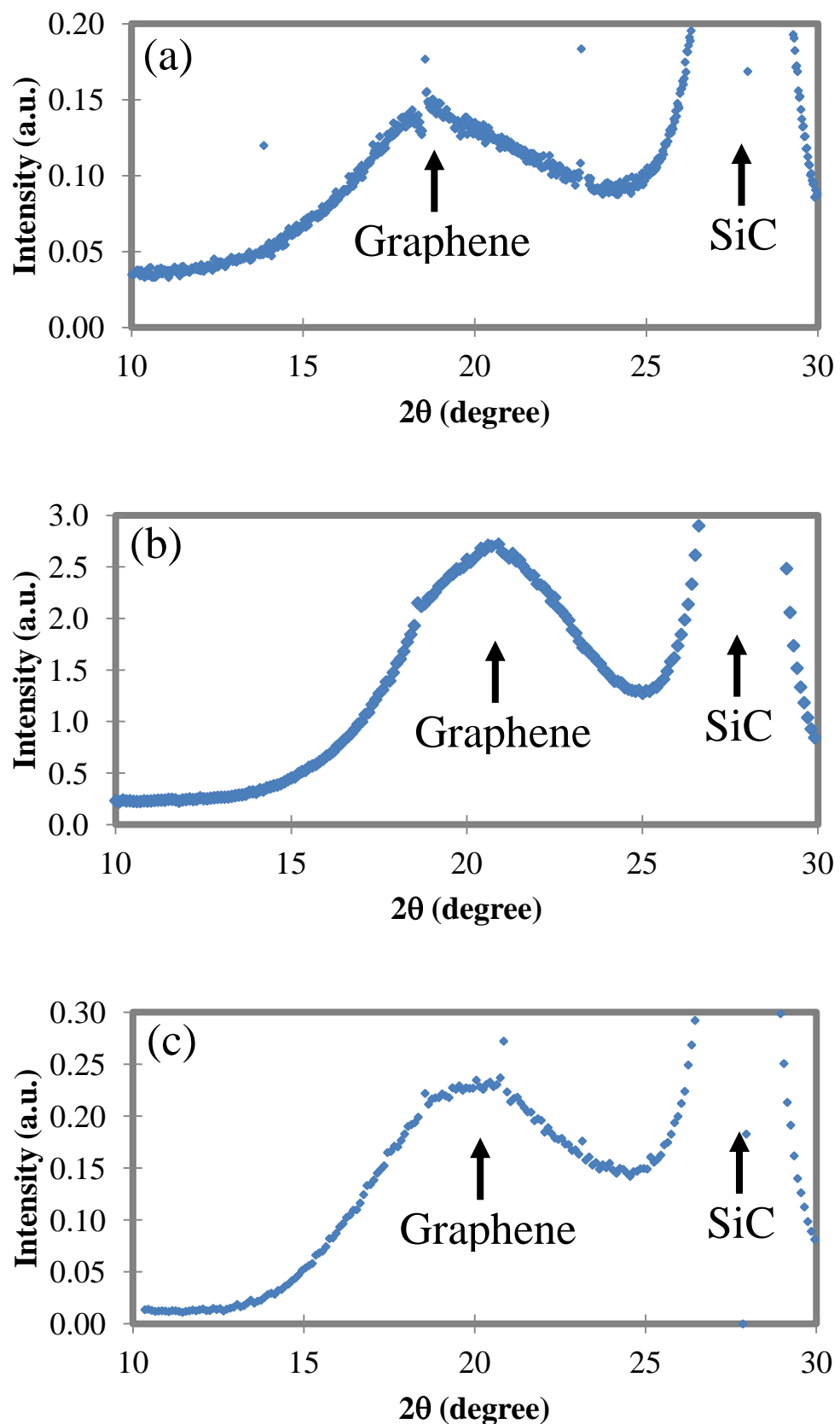


Figure 4.1. XRD experimental data of the samples annealed under Ar pressure of (a) 0.05 atm, (b) 0.3 atm and (c) 0.5 atm.

4.2.1 Calculation method for graphene thickness estimation

To estimate graphene thickness from XRD profiles, the Laue diffraction function was used. At first, a simple model was assumed that the graphene was grown uniformly on SiC substrate as shown in Figure 4.2. Under this assumption, the total scattering amplitudes is $A(\mathbf{k}) = \sum_{j=0}^N e^{-\mathbf{k}aj}$ using the summation of geometric series ($S_n = \frac{a_1(1-r^n)}{1-r}$) we can obtain $A(\mathbf{k}) = \frac{1-e^{-i(N+1)\mathbf{k}a}}{1-e^{-i\mathbf{k}a}}$ and the intensity (I) of the XRD diffraction is

$$I \propto |F|^2 \propto \frac{(\sin(N\mathbf{k} \cdot a/2))^2}{(\sin(\mathbf{k} \cdot a/2))^2} \quad (\text{eq. 4.1})$$

Here, F is a structure factor, N is the number of graphene layer and $\mathbf{k}a = (4\pi d \sin \theta)/\lambda$ where d is a lattice spacing perpendicular to the surface, θ is an angle between the incident ray and the scattering planes, λ is a wavelength of X-ray. The calculated curve using this uniform model (Figure 4.3) shows that the full width at half maximum (FWHM) will get smaller in case of higher layer number. On the other hand, if the layer number is smaller, the FWHM will increase. Moreover, this model is useless in the case of the single carbon layer (only buffer layer). The atomic scattering factor term is also added in (eq. 4.1) for the better fitting as

$$I \propto |f(\theta)|^2 \left| \sum_{j=0}^N e^{i\mathbf{k}aj} \right|^2 \quad (\text{eq. 4.2})$$

where $f(\theta)$ is an atomic scattering factor of carbon which can be taken from ref [25].

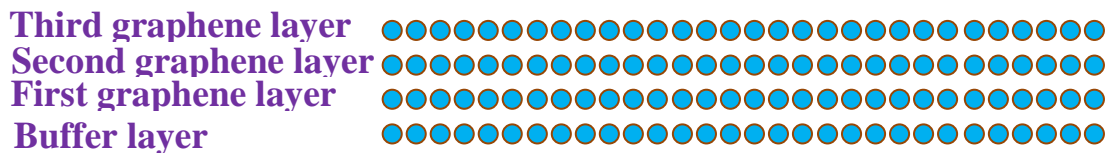


Figure 4.2. The model showing graphene grown uniformly on SiC. The number of carbon atoms (blue circle) is equal in every graphene layer.

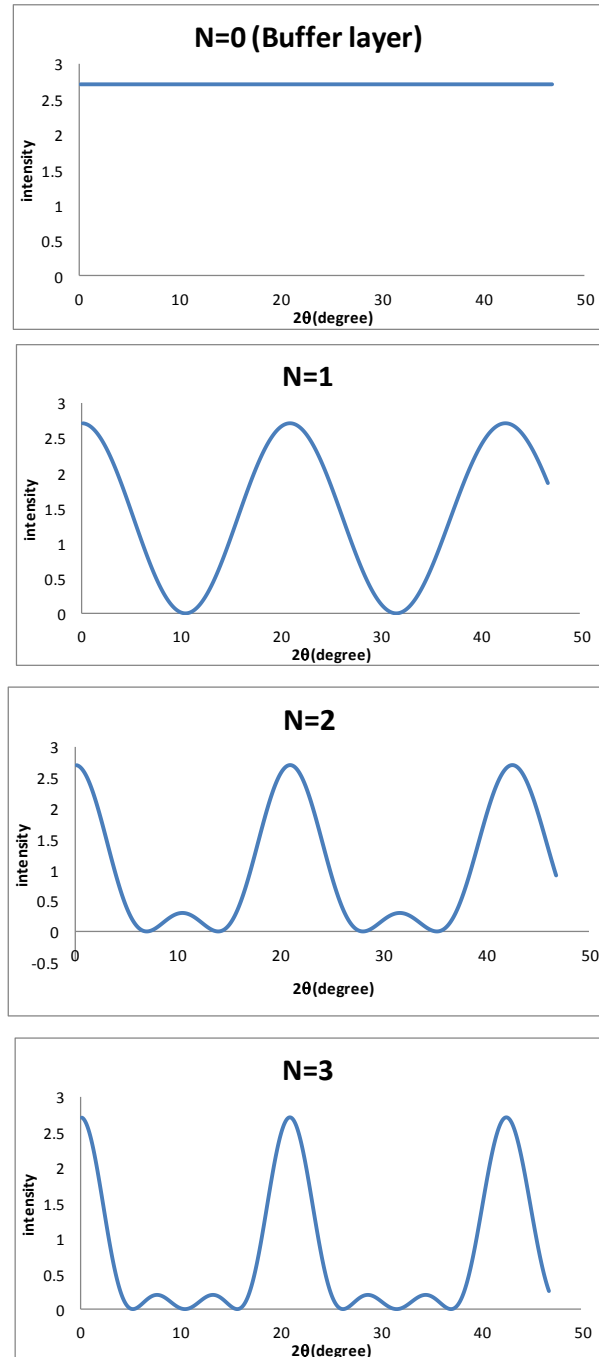


Figure 4.3. Calculated curves with various graphene thicknesses obtained from the uniform graphene model.

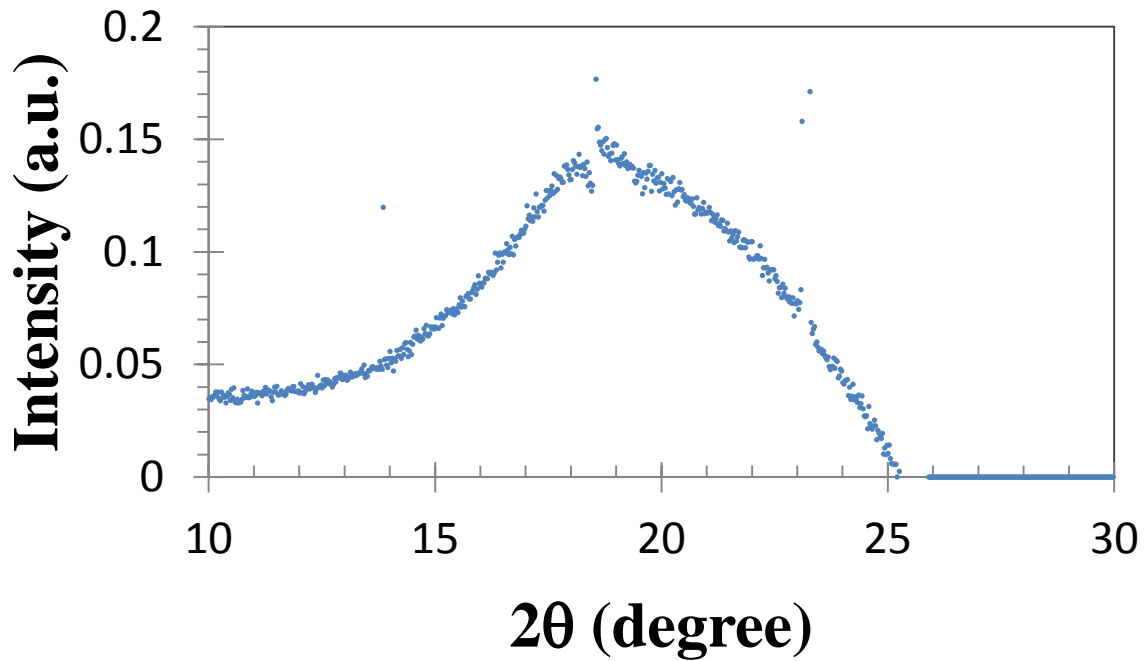


Figure 4.4. Experimental XRD data after subtracted SiC and buffer layer peak.

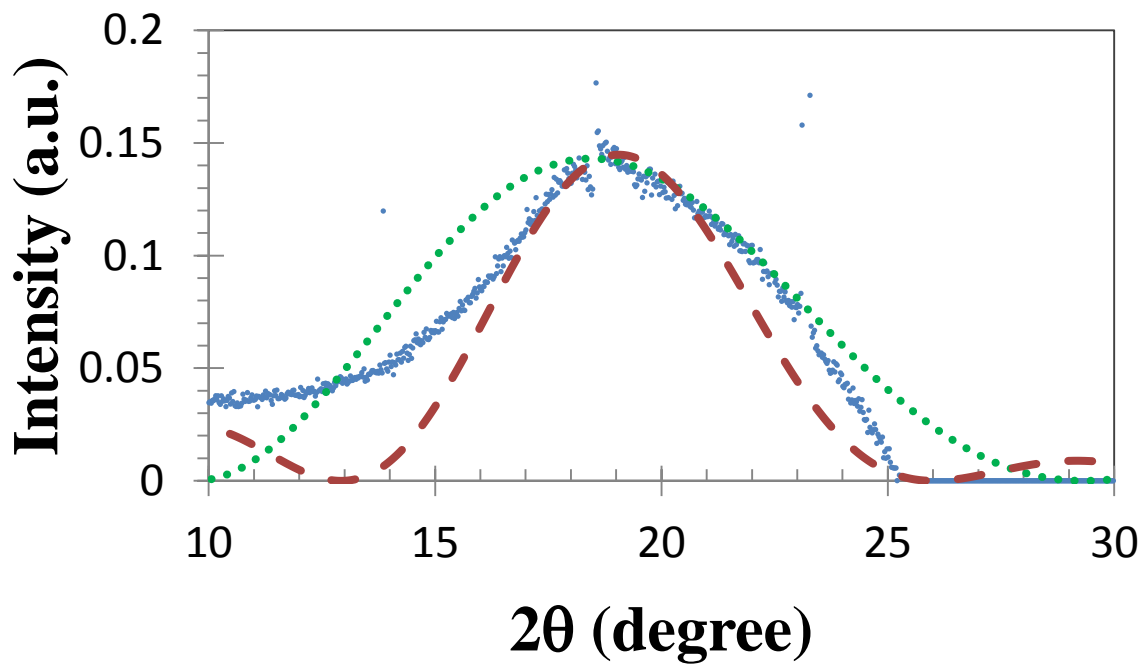


Figure 4.5. Calculated curve fitting on the graphene peak of experimental XRD profile (blue dots) of 0.05 atm 1550 °C sample. Green dot and red dash calculated curves originate from uniform model with the thickness parameters (N) are 1 and 2 layers, respectively.

4.2.2 Fitting calculated curve with uniform model on XRD experimental data

Figure 4.4 shows experimental XRD profile of 0.05 atm 1550 °C after subtracted SiC peak and SiC-buffer peak. Figure 4.5 shows the simulated curves fit on the graphene peak of this XRD profile. Green dotted line and red broken line in Figure 4.5 are calculated curves from (eq. 4.2) with graphene layer number (N) of 1 and 2, respectively. The spacing d of 3.60 Å was employed. As shown in the figure, there are large discrepancy between the calculated curve and the experimental one, i.e., too broad for $N = 1$ or too narrow for $N = 2$. This suggests that the number of graphene layers on the SiC substrate is not uniform, but has a distribution.

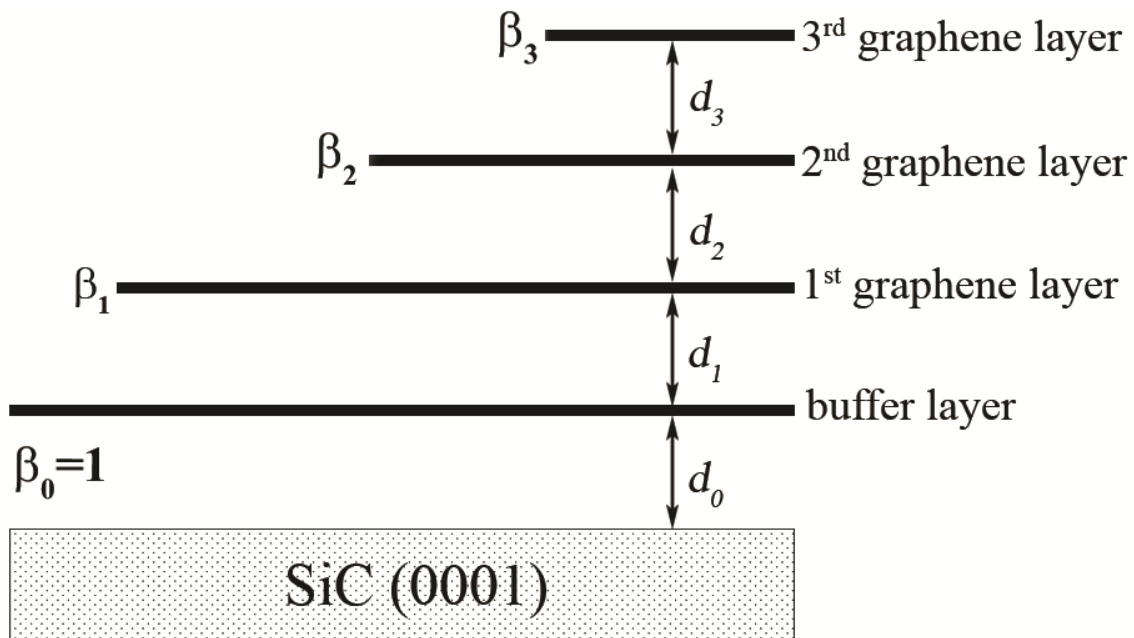


Figure 4.6. Schematic of thickness distribution model used in (eq. 4.3). β_0 is assumed as 1.

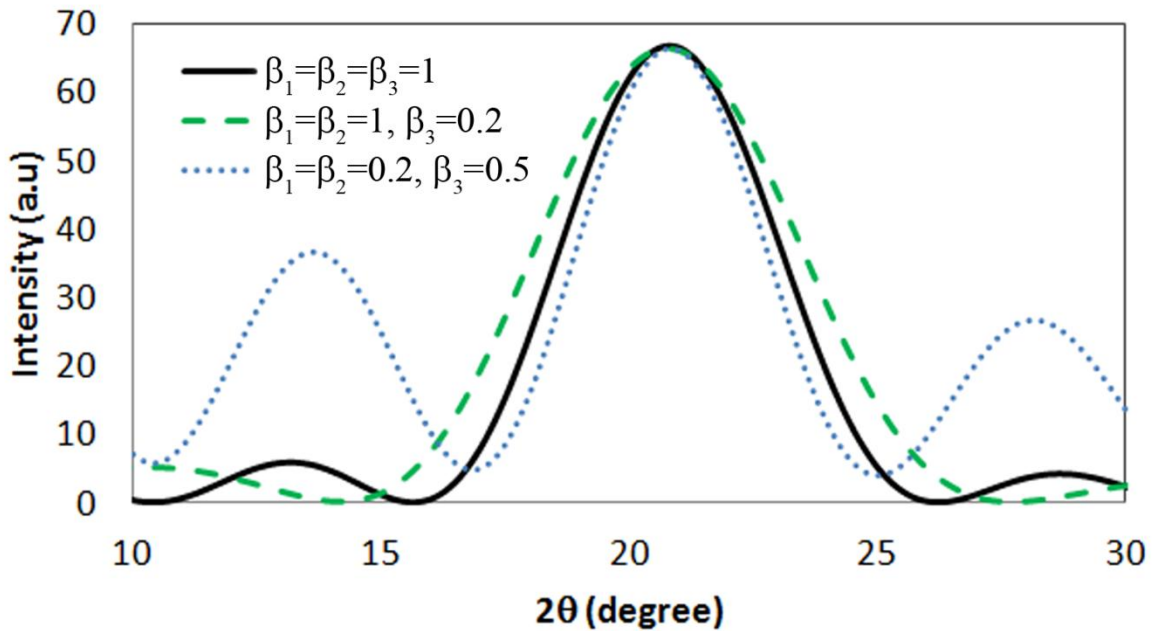


Figure 4.7. Calculated curves based on the non-uniform model with $\beta_1=\beta_2=\beta_3=1$ (black solid curve), $\beta_1=\beta_2=1, \beta_3=0.2$ (green broken curve), $\beta_1=\beta_2=0.2, \beta_3=0.5$ (blue dot curve).

4.2.3 Fitting curves calculated from non-uniform model on XRD experimental data

In order to improve the fitting, another model which includes graphene thickness distribution was introduced as shown in Figure 4.6. With this model and the Laue functions, XRD intensity can be calculated as

$$I \propto |f(\theta)|^2 \left| \sum_{j=0}^N \beta_j e^{i\mathbf{k}a_j j} \right|^2 \quad (\text{eq. 4.3})$$

where β_j is a occupancy of j -th graphene layer (its value is between 0 and 1). $\mathbf{k}a_j = (4\pi d_j \sin \theta)/\lambda$ where d_j is a lattice spacing (between j^{th} and $(j-1)^{\text{th}}$) perpendicular to the surface. Figure 4.7 shows the example of calculated curves which

originated from the non-uniform model (eq. 4.3) focusing on a region around the graphene peak. The black solid curve is a calculated intensity of graphene peak in the case of trilayer graphene with uniform thickness ($\beta_1=\beta_2=\beta_3=1$). By using the non-uniform model, the peak width of the calculated curve can be controlled by adjusting the graphene layer number, i.e. we can expand the peak width by decreasing the occupancy of 3th graphene layer as shown by the green broken curve ($\beta_1=\beta_2=1, \beta_3=0.2$). The curve can also be lifted up by decreasing occupancy of the base layer as demonstrated by blue dot curve ($\beta_1=\beta_2=0.2, \beta_3=0.5$). Note that the case of ($\beta_1=\beta_2=0.2, \beta_3=0.5$) is not practical. It is used to clearly demonstrate the lift of simulation curve.

Figure 4.8 (a)-(c) show fitting of simulated curves which calculated from (eq. 4.3). Spacing parameters (d_j) used in those calculations are shown in Table 4.1. The experimental curve in Figure 4.5 is between the simulated curves calculated from uniform model with $N=1$ and $N=2$, implying that the graphene film thickness on this sample is about 1 or 2 graphene layers. Figure 4.8 (a) shows the calculated curve with occupancy $\beta_1=1$ and $\beta_2=0.14$ fits on the data profile. Although the fitting is better than the case of uniform model, there is a large discrepancy around $2\theta=10-13^\circ$. Figure 4.8 (b) shows the calculated curve with occupancy $\beta_1=0.7$ and $\beta_2=0.14$. Decrease in β_1 can lift up the calculated curve around $2\theta=10-13^\circ$. We find that the parameters $\beta_1=0.47$ and $\beta_2=0.14$ are the best fitting for this data as shown in Figure 4.8 (c). The graphene thickness of two samples which were annealed under argon pressure of 0.3 atm and 0.5 atm were also estimated by the same method as demonstrated in Figure 4.9 (a) and (b), respectively. The fitting parameters were summarized in Table 4.1. Figure 4.10 (a)-(c) shows simulated curves (red curves) fitting on the experimental profile on 0.05 atm 1550 °C sample, 0.3 atm 1650 °C sample and 0.5 atm 1700 °C sample, respectively. These simulated curves originate from the superposition of Graphene (black), SiC (green), and SiC-buffer (blue) curves. SiC and SiC-buffer curves are calculated by using Gaussian function. The SiC-buffer peak positions are 24.7, 25.2 and 24.8 for Figure 4.10 (a)-(c), respectively implying that the spacing between SiC and buffer layers are 2.84 Å, 2.79 Å and 2.83 Å, respectively (eq. 2.3). χ^2 ($= \sum(O-E)^2/E$; O is intensity from the calculation, E is that from experiment) dependences on β_j and d_j parameter change are shown in Figure 4.11 and Figure 4.12, respectively. Please note that, in order to avoid the effect of SiC substrate, the fitting was operated in the range of 2θ from 10 to 22°. The χ^2 curves reveal steep valley, which suggests the

fitting resolution is good enough. For the interlayer spacings d_j , there is one thing to point out. d value for bulk graphite is known as 3.35 Å and the fitting results for 0.3 and 0.5 atm samples agree with this value. While for 0.05 atm sample, calculated d values are about 3.5 Å and about 5% larger than that of the bulk value. The reason for the increase in interlayer spacing of this sample is not clear but similar values were also obtained by Weng group measured by a high-resolution high-angle annular-dark-field (HAADF) scanning TEM (STEM) [27]. Coverages of n -layer graphene regions (θ_n) can be calculated from β values as $\theta_n = \beta_n - \beta_{n+1}$, and those results are shown in the “by XRD” line in Table 4.2.

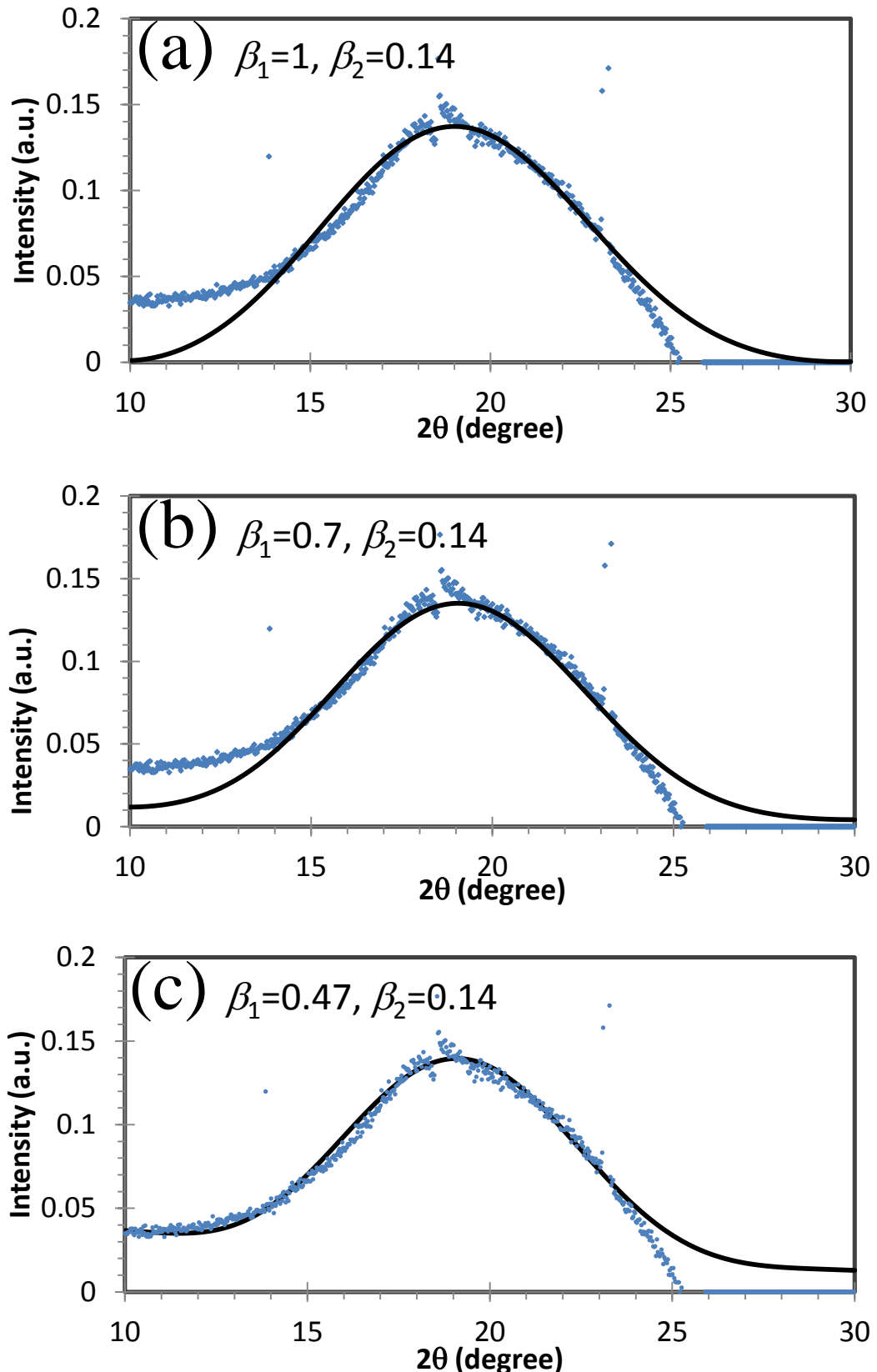


Figure 4.8. Calculated curve (black solid curve) which originated from non-uniform model fits on the graphene peak of experimental XRD profiles (blue dots) of 0.05 atm 1550 °C sample.

Table 4.1. XRD fitting parameters, d_j 's (inter layer spacing) and β_j 's (occupancy of j -th graphene layer).

Ar Pressure	0.05 atm		0.3 atm			0.5 atm	
j	1	2	1	2	3	1	2
d (\AA)	3.55 ± 0.05	3.50 ± 0.05	3.30 ± 0.05	3.30 ± 0.05	3.30 ± 0.05	3.40 ± 0.10	3.40 ± 0.05
β (%)	47 ± 2	14 ± 2	75 ± 5	35 ± 5	10 ± 5	90 ± 5	36 ± 5

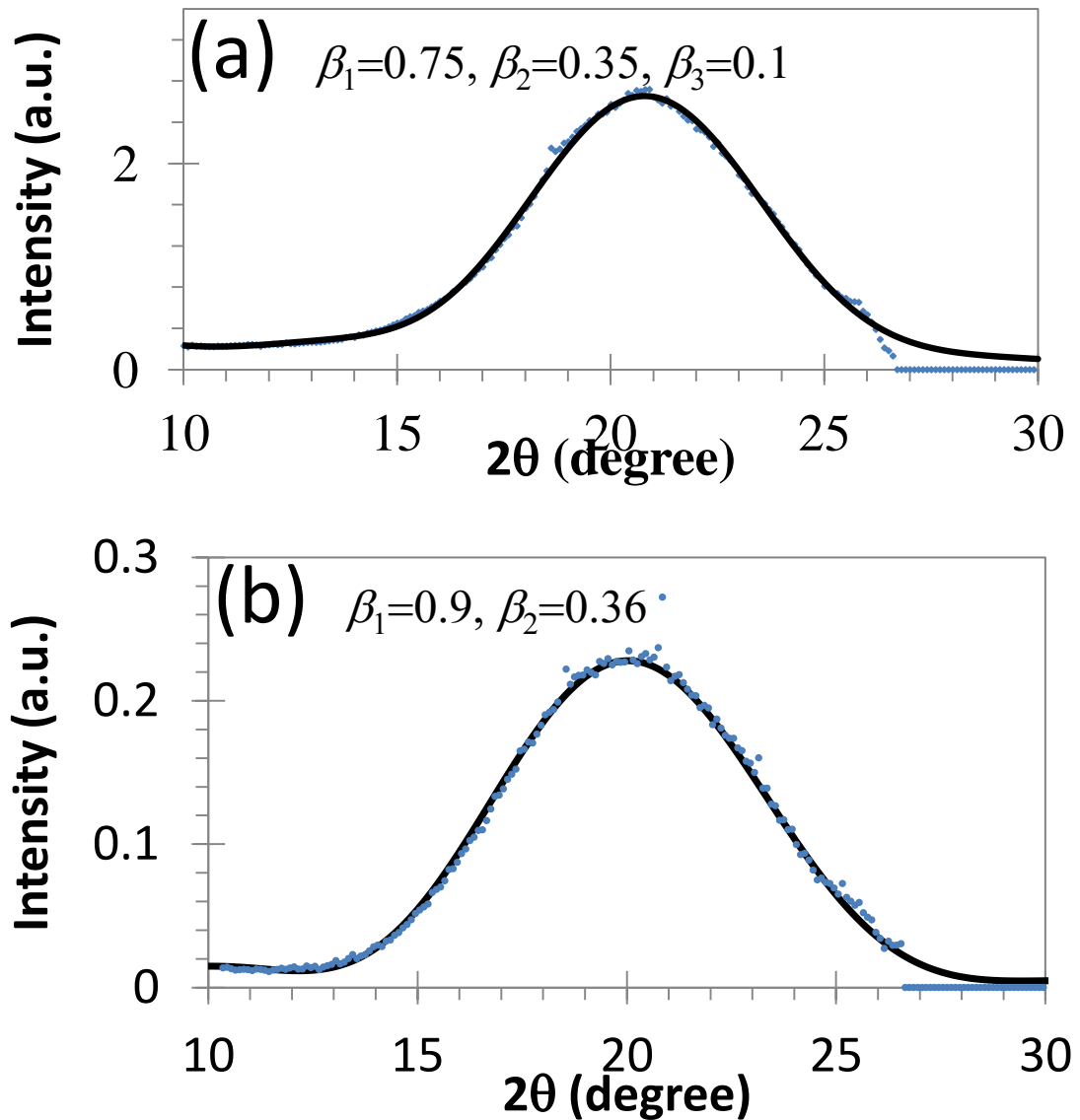


Figure 4.9. Calculated curve (black solid curve) which originated from non-uniform model fits on graphene peak of experimental XRD profiles of (a) 0.3 atm 1650 °C and (b) 0.5 atm 1700 °C.

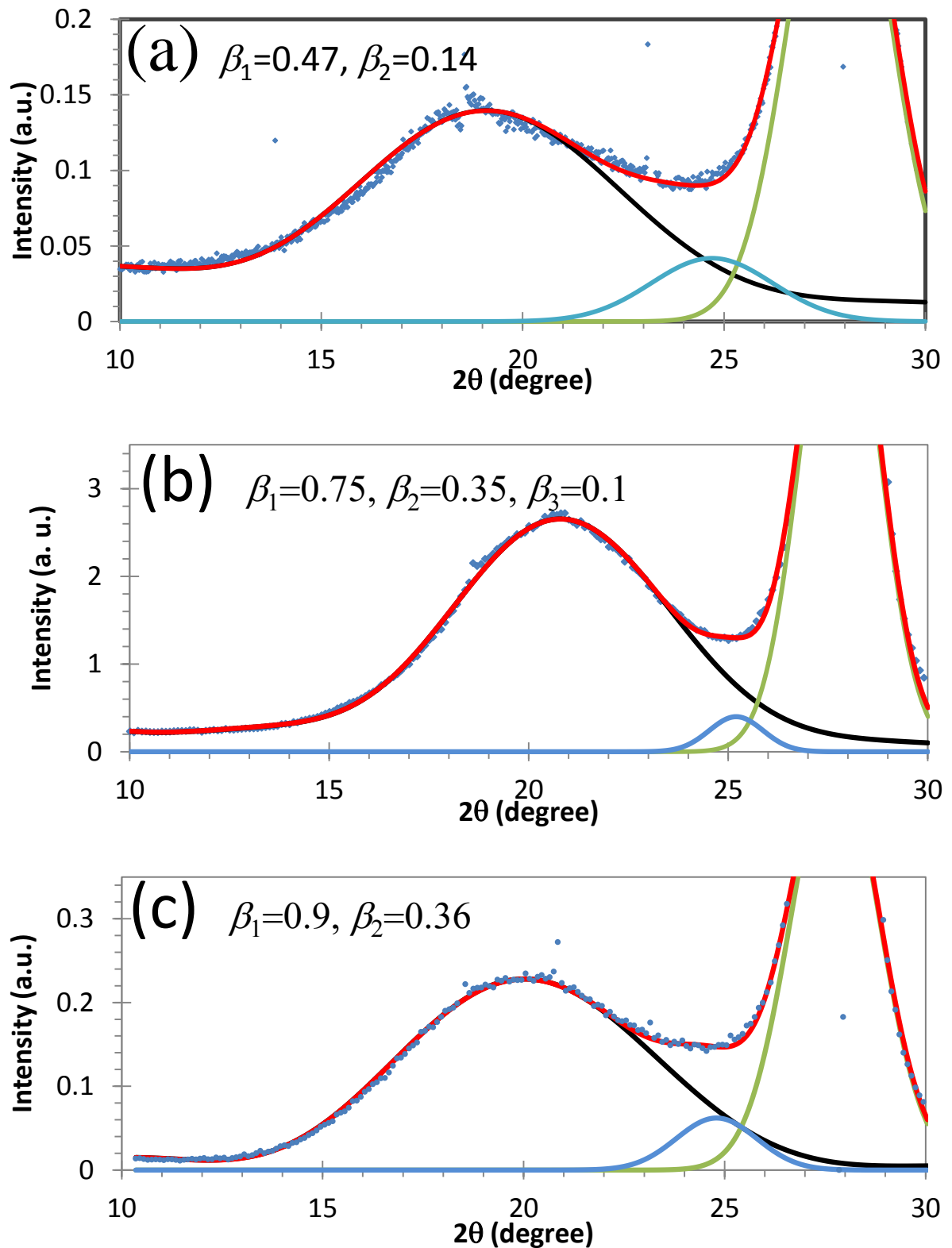


Figure 4.10. Simulation curve (red curve) fits on experimental XRD profile of (a) 0.05 atm 1550 °C sample, (b) 0.3 atm 1650 °C sample and (c) 0.5 atm 1700 °C sample. Black, green and blue curves originate from graphene layer, SiC bilayer and SiC-buffer layer, respectively. Simulation black curve is calculated from (eq. 4.3). Green and blue curves are calculated from Gaussian function.

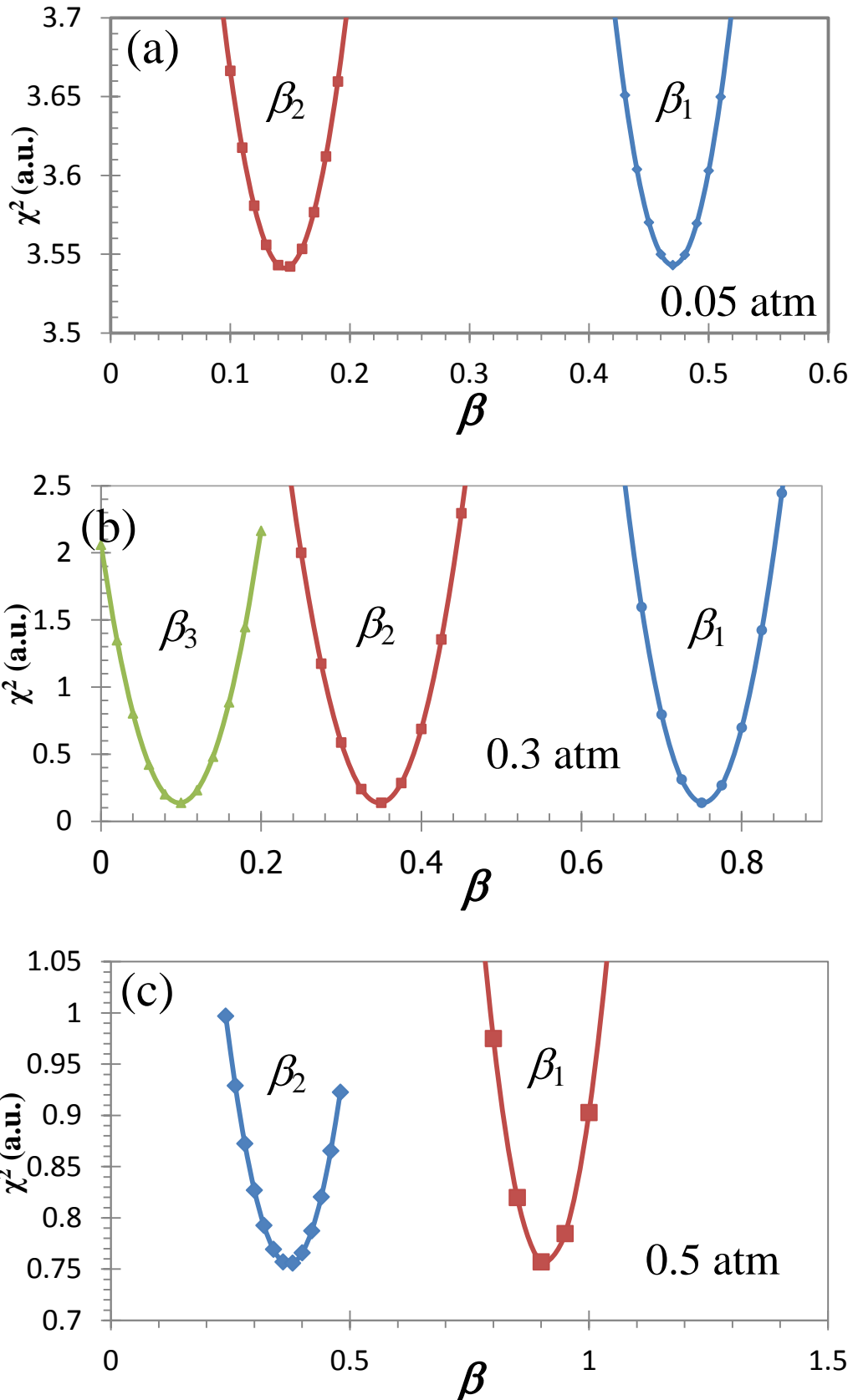


Figure 4.11. The chi-squared (χ^2) dependence on β_j parameters for (a) 0.05 atm 1550 °C sample, (b) 0.3 atm 1650 °C sample and (c) 0.5 atm 1700 °C sample. The other fitting parameters (except β_j) are taken from Table 4.1.

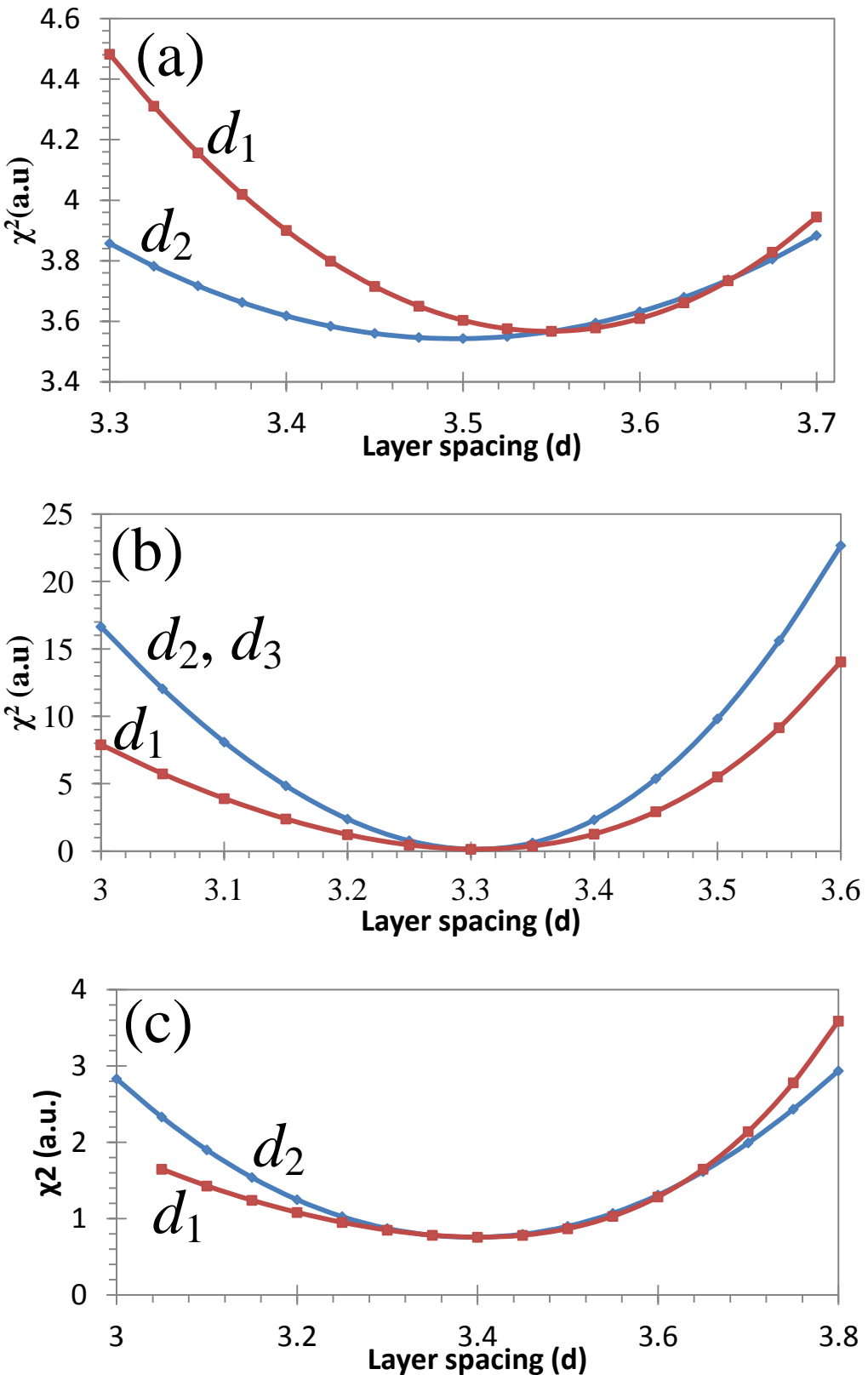


Figure 4.12. The chi-squared (χ^2) dependence on layer spacing (d_j) parameters for (a) 0.05 atm 1550 °C sample, (b) 0.3 atm 1650 °C sample and (c) 0.5 atm 1700 °C sample. The other fitting parameters (except d_j) are taken from Table 4.1.

4.3 Confirmation of the thickness estimation by SEM

Scanning electron microscope (SEM) is an electron microscope which focuses an electron beam and scans on the sample to produce its images by detecting secondary electrons from the sample surface. In the case of different graphene film thickness on SiC, the intensity of secondary electron emitted from the sample is distinct as shown in Figure 4.13. Namely, the secondary electron intensity of the thicker graphene area is higher than that of thinner region.

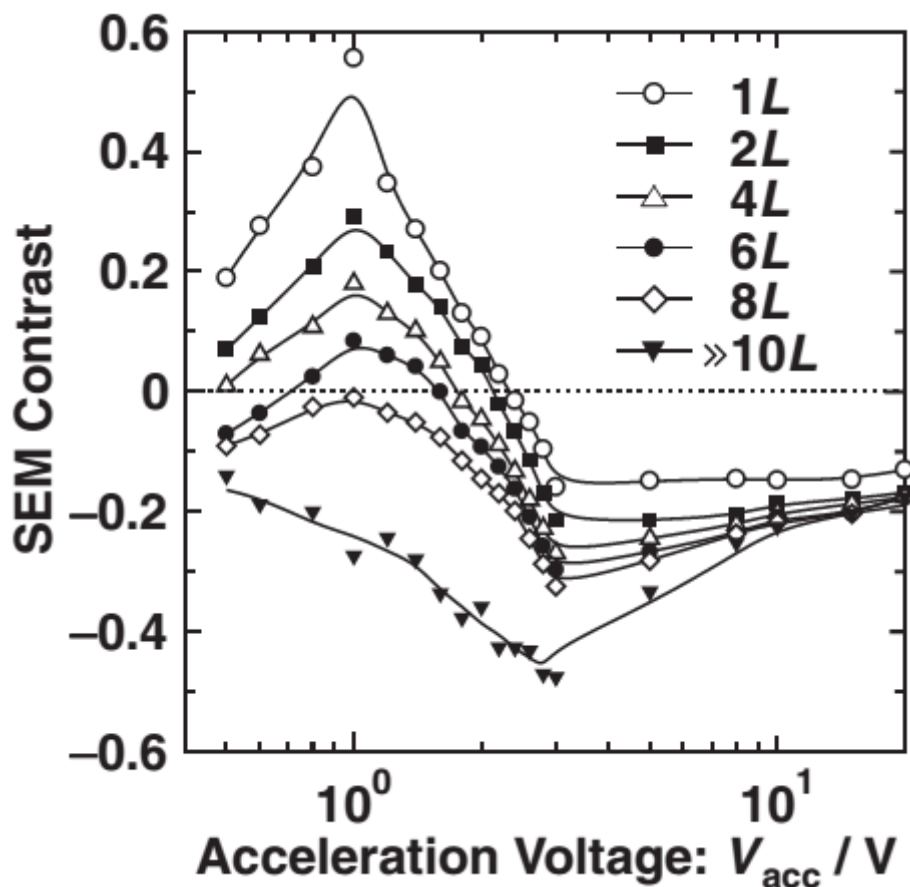


Figure 4.13. Dependence of SEM contrast on the primary electron acceleration voltage for 1, 2, 4, 6, 8 and 10 graphene layers (this figure reprint from Ref [26]). Unit of the horizontal axis should be corrected to kV, though the figure is reproduced without modification here. Copyright (2010) The Japan Society of Applied Physics.

To confirm the layer number distribution obtained by XRD analysis, low acceleration UHV-SEM experiments were carried out. Figure 4.14 shows respective SEM images for 0.05 atm 1550 °C sample, 0.3 atm 1650 °C sample and 0.5 atm 1700 °C sample. As shown in the figures, there are clear contrasts on the sample surfaces (indicated by 0, 1, and 2 in the figure). The contrast in SEM images reflects the number of layer of graphene. However, absolute values of the layer number cannot be determined. To overcome this weakness, the following procedure was carried out. Samples used in this experiment were heated by direct current, so that sample area near electrode could not be heated as high as graphitization temperature. Thus, SiC surface remains in this area. Therefore, continuous observation from the SiC area to the graphitized area gives a relationship between contrast and layer number for each sample. As a result, it was confirmed that the area 0, 1 and 2 in SEM images correspond to buffer layer, monolayer and bilayer graphene regions, respectively. Unfortunately, it was impossible to distinguish more than 2 layers region from bilayer region under our experimental condition (acceleration voltage, S/N ratio etc.). It is also a problem to compare XRD and SEM results, since observation area is different, ~1 mm for XRD and ~10 μm for SEM. Therefore, SEM measurements were carried out at several points within XRD measurement area, and area of each contrast was summed up. Coverages of n -layer graphene regions derived from SEM images are listed in “by SEM” line in Table 4.2. As shown in the table, coverages determined by XRD analysis are in good agreement with those measured by SEM.

Table 4.2. Coverages of n -layer graphene regions determined by XRD and SEM.

Ar Pressure	0.05 atm			0.3 atm				0.5 atm		
	Layers (n)	Buffer (0)	Monolayer (1)	Bilayer (2)	Buffer (0)	Monolayer (1)	Bilayer (2)	Trilayer (3)	Buffer (0)	Monolayer (1)
by XRD	53%	33%	14%	25%	40%	25%	10%	10%	54%	36%
by SEM	53%	41%	6%	25%	48%		27%	4%	58%	38%

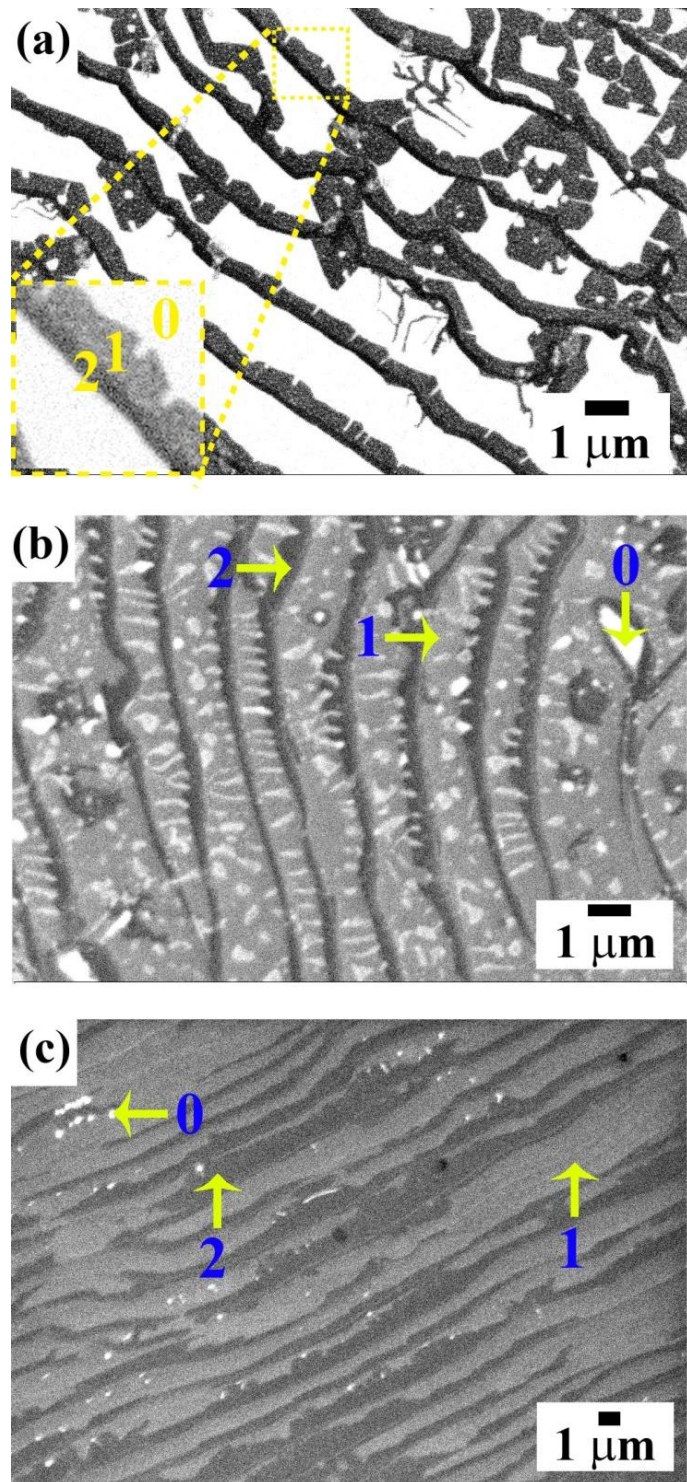


Figure 4.14. Low accelerating voltage UHV-SEM images of (a) 0.05 atm 1550 °C sample, (b) 0.3 atm 1650 °C sample and (c) 0.5 atm 1700 °C sample taken with accelerating voltage of 2.2, 2.2 and 1.7 kV, respectively. There are 3 contrast levels in these images, bright (indicated 0 in the figure), dark gray (1), and black (2), corresponding to buffer layer, monolayer and at least bilayer graphene, respectively. Inset figure in (a) is the magnified image in the broken line square. The image contrast was adjusted to make a distinction of graphene thickness clearly.

4.4 Confirmation of the thickness estimation by ARPES

ARPES (angle-resolved photoemission spectroscopy) is one of techniques for estimating layer number of epitaxial graphene since the number of π bands increases with the number of layers. Figure 1.2 shows calculated band structures of the interface (buffer), 1 and 2 graphene layers. At the interface layer (left panel), there is no π band near E_F at the K point. The monolayer (middle) and bilayer (right) show one and two π bands, respectively near E_F around the K point. Figure 4.15 (a)-(d) show the experimental data from reference [28] corresponding to the graphene band structures of 1-4 graphene layers.

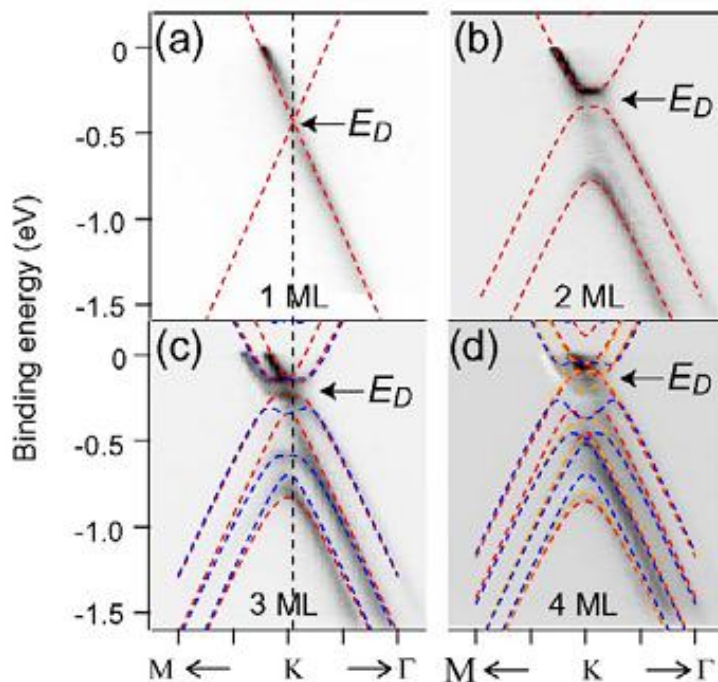


Figure 4.15. ARPES band structure of the π and π^* bands near E_F and K-point. (a)-(d) are the data corresponding to graphene the band structure of 1-4 graphene layers. Reprinted with permission from [29]. Copyright (2007) by the American Physical Society.

For qualitative inspection, ARPES experiment was also carried out and its result is shown in Figure 4.16. The sample used in this experiment is graphene grown under 0.05 atm of Ar pressure, which was determined as

mixture of 33% monolayer and 14% bilayer graphene using the XRD analysis. Here, the origin of the energy axis is taken at the Fermi energy E_F . The inset curves at the bottom of Figure 4.16 display intensities of photoelectrons with energies of -1.5, -2 and -2.5 eV as a function of wave number (the momentum distribution curve). The intensity profile was fitted by Gaussian functions, and the results were shown by broken lines. In this fitting noise peaks indicated by vertical arrows were ignored. The electronic band obtained by the ARPES measurement consists of a single branch as shown by the fitting result, which implies this sample consists of monolayer graphene [15]. However, the band apparently shows a band gap (~ 0.3 eV) and binding energy shift (~ 0.4 eV), which is different from free standing graphene monolayer [16]. It is considered that the band gap opening and the energy shift are caused by interaction (strain and/or doping) between monolayer graphene and the substrate [30]. Since ARPES evaluates only graphene layers (but not a buffer layer). It can be said that the graphene region is dominated by monolayer region. However, it is very difficult to obtain quantitative values of the layer distribution. The XRD analysis delivers that 70% ($33/(33+14)$) of graphene region of this sample is monolayer, which is qualitatively consistent with the ARPES result.

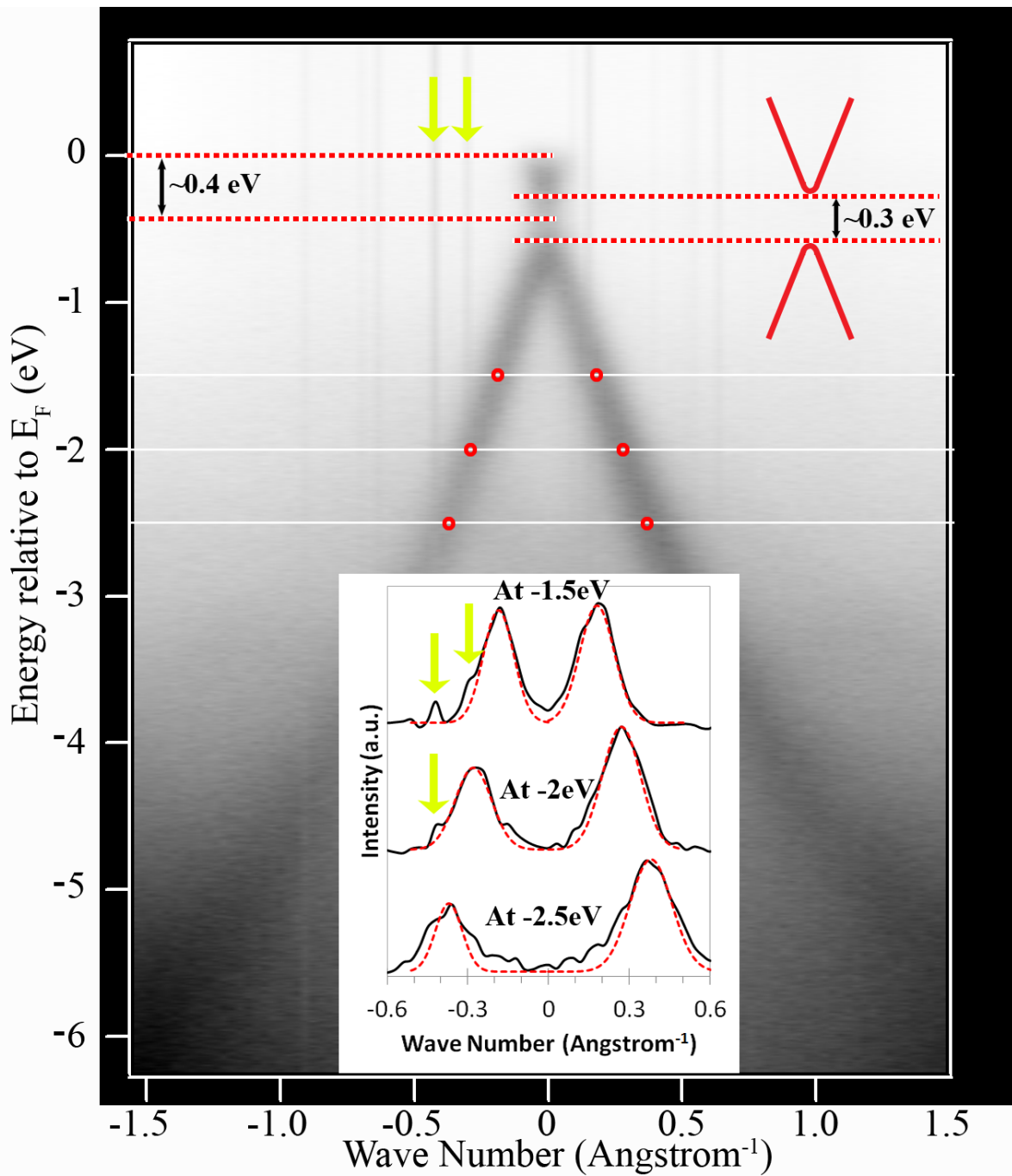


Figure 4.16. ARPES spectra of the 0.05 atm 1550 °C sample around the K point of graphene. Upper right illustration represents a schematic electronic band structure which originated from a graphene monolayer. The band gap between valence and conduction bands may originate from the interaction between graphene and SiC substrate. An inset at the bottom shows momentum distribution curves of photoelectrons at the energies of -1.5, -2 and -2.5 eV. Broken lines in the graph show the components of the monolayer electronic structures fitted using Gaussian functions. Vertical arrows indicate two of noise signal lines (both in ARPES mapping and the inset graph).

4.5 Confirmation of the thickness estimation by Raman

Raman spectroscopy is another method for estimating the layer number of few-layer graphene on SiC. Since the electron band structure of graphene monolayer and bilayer near K point are different as shown in Figure 1.2, the shapes of 2D peak of the graphene monolayer and bilayer are also different, i.e., there is a single 2D peak for the graphene monolayer but in case of graphene bilayer, this 2D peak splits in 4 component curves [31]. Figure 4.17 (a) shows Raman spectra of 0.05 atm 1550 °C sample, 0.3 atm 1650 °C sample and 0.5 atm 1700 °C sample. Figure 4.17 (b)-(d) show the simulation curves fitting on the experimental data around 2D peak of 0.05 atm 1550 °C sample, 0.3 atm 1650 °C sample and 0.5 atm 1700 °C sample, respectively. In the case of 0.05 atm 1550 °C sample (Figure 4.17 (b)) the 2D peak can be fit by a single curve but for 0.3 atm 1650 °C and 0.5 atm 1700 °C sample, the 2D peak can be fit by 4 component curves. These imply that at the Raman measurement area, graphene layer numbers of 0.05 atm 1550 °C sample, 0.3 atm 1650 °C sample and 0.5 atm 1700 °C sample are monolayer, bilayer and bilayer, respectively. These are corresponding with XRD, SEM and ARPES.

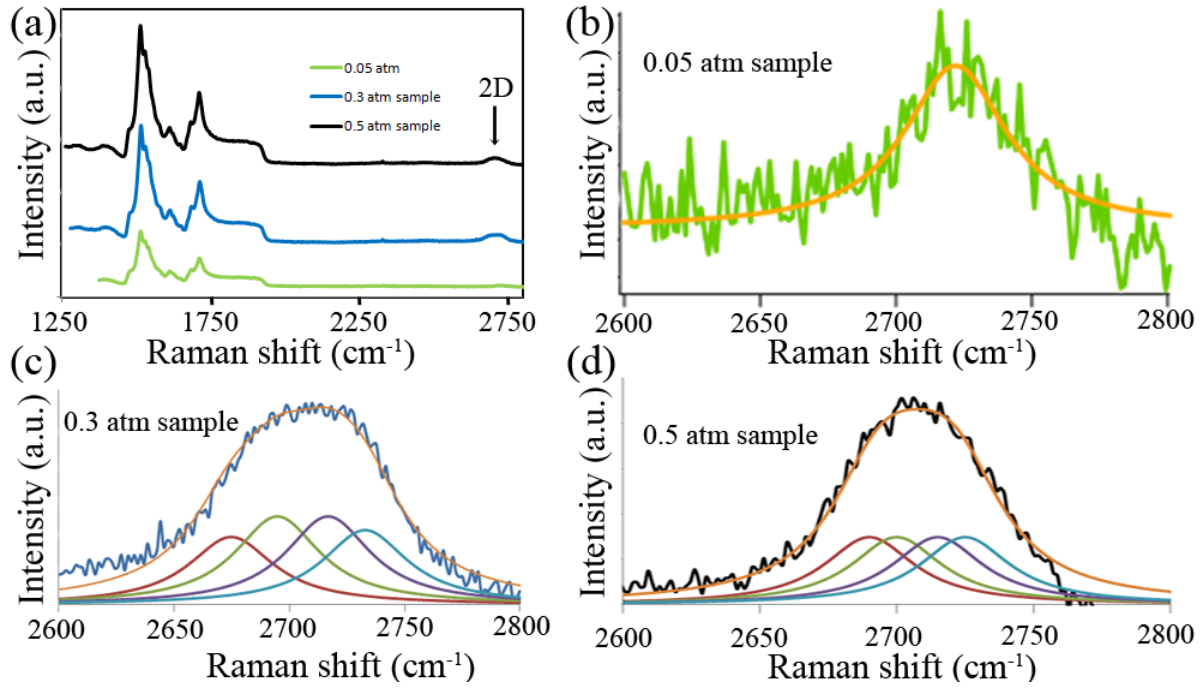


Figure 4.17. (a) Raman spectra of 0.05 atm 1550 °C sample (green), 0.3 atm 1650 °C sample (blue) and 0.5 atm 1700 °C sample (black). (b)-(c) Raman spectra at 2D peak of (b) 0.05 atm 1550 °C sample, (c) 0.3 atm 1650 °C sample and (d) 0.5 atm 1700 °C sample. Orange curves are simulation curves fitting on the 2D peaks data curves. Small red, green, violet and blue curves in (c) and (d) are the component curves of the simulation ones. All component curves are calculated from Lorentzian function.

4.6 Conclusion

In this section I offer the new and simple method to deliver absolute and reliable information on graphene thickness distribution on SiC substrate using XRD experiments and Laue function. Unlike other methods like low acceleration SEM, this is a standardless method, i.e., you don't need a standard or a known sample to determine absolute values of layer number distributions. This approach is, therefore, suitable for the sample on which at least 1 carbon layer (buffer layer) covers the whole area shone by an X-ray beam.

References for chapter 4

- [15] J. Hass, W. A. de Heer, E. H. Conrad, The growth and morphology of epitaxial multilayer graphene, *J. Phys.: Condens. Matter* 20, 323202 (2008).
- [16] A.K. Geim and A. H. MacDonald, 5 Graphene: Exploring carbon flatland, *Physics Today* 60, 35 (2007).
- [17] H. Hiura, H. Miyazaki, K. Tsukagoshi, determination of the number of graphene layers: discrete distribution of the secondary electron intensity stemming from individual graphene layers, *appl. phys. express* 3, 095101 (2010).
- [18] Luxmi, S. Nie, P. J. Fisher, R. M. Feenstra, G. Gu and Y. Sun, Temperature dependence of epitaxial graphene formation on SiC(0001), *J. Electronic Matt.* 38, 718 (2009).
- [19] W. A. de Heer, C. Berger, X. Wu, P. N. First, E. H. Conrad, X. Li, T. Li, M. Sprinkle, J. Hass, M. L. Sadowski, M. Potemski and G. Martinez, Epitaxial graphene, *Solid state Com.* 143, 92 (2007).
- [20] S. Shivaraman, M.V.S. Chandrashekhar, J. J. Boeckl and M. G. Spencer, Thickness Estimation of Epitaxial Graphene on SiC Using Attenuation of Substrate Raman Intensity, *J. Electronic Matt.* 38, 725 (2009).
- [21] J. Hass, R. Feng, J. E. Millan-Otoya, X. Li, M. Sprinkle, P. N. First, W. A. de Heer, and E. H. Conrad, Structural properties of the multilayer graphene/4H-SiC (0001) system as determined by surface x-ray diffraction, *Phys. Rev. B* 75 214109 (2007).
- [22] I. K. Robinson, Crystal truncation rods and surface roughness, *Phys. Rev. B* 33, 3830 (1986).
- [23] H. Hibino, H. Kageshima, M Nagase, Epitaxial few-layer graphene: towards single crystal growth, *J. Phys. D: Appl. Phys.* 43, 374005 (2010).
- [24] A. Charrier et al., “Solid-state decomposition of silicon carbide for growing ultra-thin heteroepitaxial graphite films”, *J. Appl. Phys.* 92, 2479 (2002).
- [25] P. Brown, A. Fox, E. Maslen, M. O'Keefe and B. Willis, International Tables for Crystallography, Vol. C, 6, 554, (2004),
<http://dx.doi.org/10.1107/97809553602060000600>.
- [26] H. Hiura, H. Miyazaki, K. Tsukagoshi, “Determination of the Number of Graphene Layers: Discrete Distribution of the Secondary Electron Intensity Stemming from Individual Graphene Layers”, *Applied Physics Express* 3, 095101 (2010).
- [27] X. Weng, J. A. Robinson, K. Trumbull, R. Cavalero, M. A. Fanton and D. Snyder, Structure of few-layer epitaxial graphene on 6H-SiC (0001) at atomic resolution, *Appl. Phys. Lett.* 97, 201905 (2010).
- [28] J Hass, W A de Heer and E H Conrad, *J. Phys.: Condens. Matter* 20, 323202 (2008).

- [29] T. Ohta, A. Bostwick, J. L. McChesney, T. Seyller, K. Horn and E. Rotenberg, “Interlayer Interaction and Electronic Screening in Multilayer Graphene Investigated with Angle-Resolved Photoemission Spectroscopy”, Phys. Rev. Lett. 98, 206802 (2007).
- [30] Z. H. Ni, T. Yu, Y. H. Lu, Y. Y. Wang, Y. P. Feng and Ze Xiang Shen, “Uniaxial Strain on Graphene: Raman Spectroscopy Study and Band-Gap Opening”, ACS Nano 2, 2301 (2008).
- [31] A. C. Ferrari, J. C. Meyer, V. Scardaci, C. Casiraghi, M. Lazzeri, F. Mauri, S. Piscanec, D. Jiang, K. S. Novoselov, S. Roth and A. K. Geim, “Raman Spectrum of Graphene and Graphene Layers”, Phys. rev. lett. 97,187401 (2006).

Chapter 5

Growth of Epitaxial Graphene with Large Domain on C-terminated 6H-SiC (000 $\bar{1}$)

Graphene is attracting considerable attention from the physics, chemistry, materials science, and electrical engineering communities. It is considered as a viable candidate for all-carbon post complementary metal-oxide-semiconductor electronics. To this end, wafer-size graphene is desired to be grown on an insulating or semiconducting substrate while preserving the unique electronic properties. Although, large-sized graphene can be produced through chemical vapor deposition (CVD) on metals, after transferring to an insulating substrate, the CVD-grown graphene presents quite low carrier mobility because the impurity atoms or clusters are introduced inevitably into the film [32]. The growth of epitaxial graphene on high resistive SiC, without any transferring process, is considered as a promising approach to the graphene-based electronics [33]. The surface free energies of SiC are different at the two polar surfaces, 2220 erg/cm² for the Si-terminated surface and 300 erg/cm² for the C-face [34]. The C-terminated surface graphitizes at a higher rate compared with the opposite one [35] and always forms multilayer epitaxial graphene. From the viewpoint of transistor application, thin graphene layers are desired to effectively switch the on/off current. Up to now, it is still challenging to produce few-layer graphene (FLG) on the C-face SiC. Importantly, graphene on C-face possesses unprecedented carrier mobility ($>200,000\text{ cm}^2\text{ V}^{-1}\text{ s}^{-1}$) [36], making an excellent choice for high-performance transistor.

Graphene epitaxially grown on SiC was generally accomplished in ultrahigh vacuum (UHV). The synthesis conditions can be precisely controlled, and the growth can be *in situ* monitored by techniques such as reflection high-energy electron diffraction (RHEED) and angle-resolved photoemission

spectroscopy. The UHV-grown graphene consists of small-sized domains and considerable defects, and the carrier mobility is not as high as expected. Recently, it has been reported that a dense argon gas used during graphene growth can create large domains on the Si-face of SiC [37, 38]. This method has been seldom used on the C-face of SiC because the effect of high-temperature annealing results in the fast formation of thick graphene layers. In this chapter, an Ar-mediated rapid heating method developed to prepare high quality graphene on C-face SiC is reported. This method reduces the soak time at high temperature and thus provides the formation of FLG with uniform thickness distribution. The surface step height is lower than 9 nm, so that the graphene layers can grow continuously over these steps to form large-sized domains.

5.1 Experimental

Few-layer graphene was prepared on commercial n-type 6H-SiC (0001) ($\rho = 0.076 \Omega \text{ cm}$) substrates. The synthesis was carried out in a double-chamber vacuum system, in which the sample can be studied by RHEED and AES without exposure to air. To remove the surface oxides, we deposited 2 monolayers (ML) of Si on the SiC surface in UHV, followed by heating at 1000 °C for 10 min. Then, the SiC was heated up to 1650 °C with a heating rate of about 30 °C/s in 0.05 atm Ar. The soak time at the annealing temperature was 10 s. After heating, the sample was rapidly cooled down. Micro-Raman spectroscopic analyses were performed on a Renishaw inVia Reflex Raman microscope. The excitation source was a 532-nm laser. Atomic force microscopy (AFM) measurements were carried out in air using a Shimadzu SPM-9600 scanning probe microscope (Shimadzu Corp., Kyoto, Japan).

5.2 Structure of graphene on C-face SiC measured by RHEED

The surface structure was investigated by RHEED. The as-received SiC substrate gives the SiC (1 × 1) structure, as shown in Figure 5.1 (a and b). The

RHEED patterns after heating in Ar ambience at 1650 °C are shown in Figure 5.1 (c and d). In each azimuth, the diffraction spots (or strips) originated from graphene lattices are denoted with G and G*. The coexistence of G and G* in one azimuth indicates the existence of the rotated graphene domains. The other diffraction spots are attributed to the SiC (3 × 3) reconstruction. When heated in UHV, a SiC (3 × 3) reconstruction is usually observed prior to the graphitization on the C-face SiC [40]. Hieber et al. have reported two graphene domains that grow on the neighboring SiC (3 × 3) and (2 × 2) reconstructions, respectively [41]. The absence of SiC (2 × 2) reconstruction, as shown in Figure 5.1, signifies that the graphene layers are of high uniformity in phase. Figure 5.1 (e) schematizes the combined reciprocal lattice of SiC/graphene.

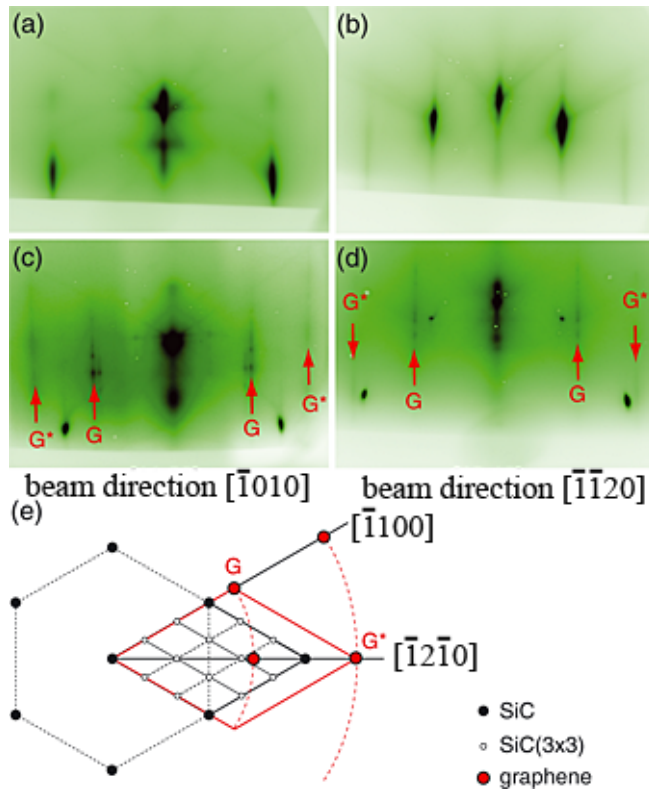


Figure 5.1. Reflection high-energy electron diffraction patterns of SiC before (a, b) and after graphitization (c, d). Azimuth of the incident beam are $\bar{1}010$ (a, c) and $\bar{1}\bar{1}20$ (b, d); (e) illustrates the reciprocal lattices of SiC, including the 3×3 surface reconstruction, and of the rotated graphene.

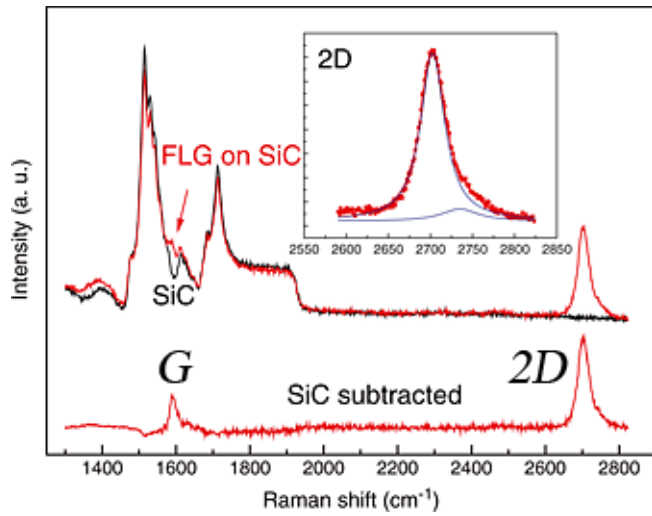


Figure 5.2. Raman spectra of SiC (0001) before and after the few-layer graphene (FLG) growth (top spectra). The bottom shows the FLG spectrum after SiC subtracting. Inset: the Lorentz fitting of the 2D band.

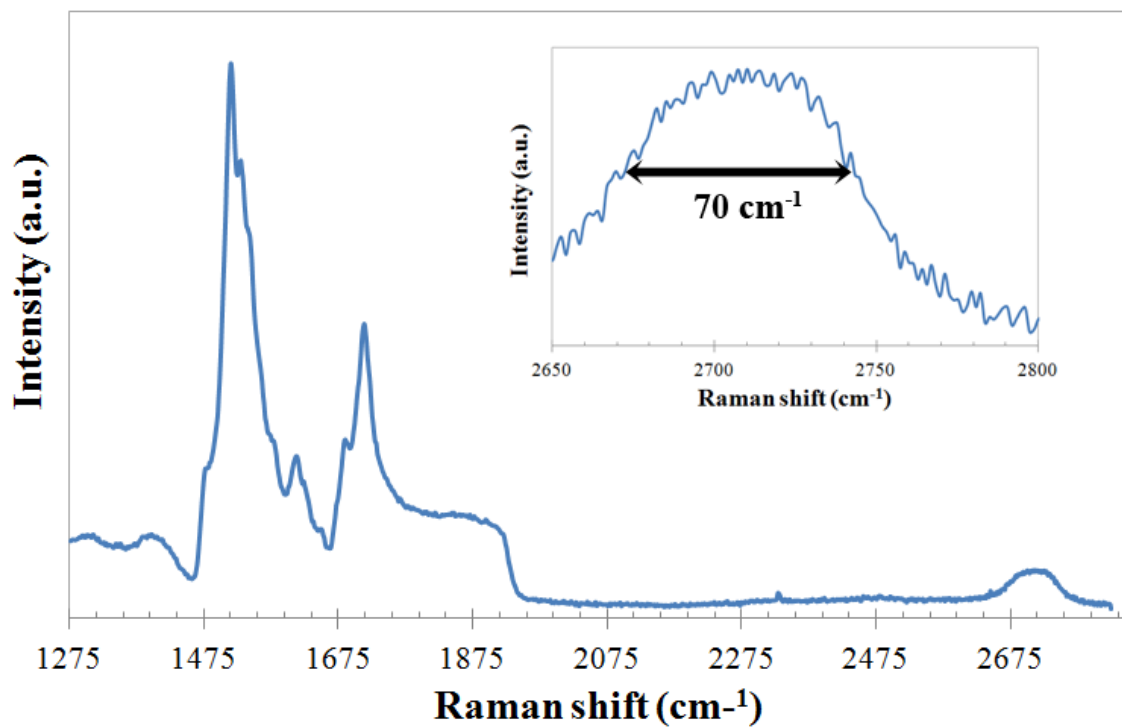


Figure 5.3. Raman spectra of few-layer graphene on Si-face SiC (0001). Inset: the magnified image around 2D peak position showing the full-width at half-maximum of 2D peak is about 70 cm⁻¹.

5.3 Graphene properties characterized by Raman

The Raman spectra of C-face SiC (000 $\bar{1}$) before and after the heating are shown by black and red lines, respectively on the upper side in Figure 5.2. A red line under side in Figure 5.2 presents the Raman spectra of graphene on SiC (000 $\bar{1}$) after subtracting SiC signal. After graphitization, the 2D band of FLG is clearly detected around 2700 cm $^{-1}$, whereas the peak of G band is not so sharp due to the background from the SiC substrate. When the spectrum from SiC is subtracted, the G peak, roughly 1/2 the height of the 2D peak, is apparently observed at 1585 cm $^{-1}$, as shown in the bottom spectrum. In addition, the D band (around 1350 cm $^{-1}$) is nearly invisible, indicating that the graphene has large-sized domains and contains few defects or sp 3 carbon. The shape of the 2D peak is related to the graphene structure. It is widely known that the 2D band of monolayer graphene shows a sharp, single Lorentz peak. In the AB Bernal stacking, it contains multiple components. For instance, the 2D peak of graphite consists of two components [42], whereas in few-layer graphene on the Si-face of SiC, it shows a broad peak with four comparable components [43]. Figure 5.3 shows the Raman spectra of few-layer graphene on Si-face SiC (0001) with the full-width at half-maximum of 2D peak of about 70 cm $^{-1}$. It is obviously exhibiting broader than the case of few-layer graphene on C-face SiC (0001). The 2D band of C-face graphene is fitted by Lorentz peaks (see Figure 5.2 inset). It contains an intense peak located at 2702 cm $^{-1}$, whose intensity is 16 times larger than the weaker one at 2739 cm $^{-1}$. As the intensity of the two components is not comparable, the sharp 2D peak is different from that of AB stacked graphene layer, but is more semblable to the single 2D peak of turbostratic graphite [43]. There are 2 types of rotated graphene planes on C-face SiC, i.e., AB stacking and turbostratic graphite. The significant intensity difference between two 2D components implies that the fraction of AB stacking is not as much as expected. This can be assigned to the interlayer expansions caused by the interference of π^* states between adjacent planes, which makes the FLG analogous isolated sheets in behavior [44].

Owing to the different work functions between graphene and SiC, the as-grown epitaxial graphene is usually n-doped [45], and the electron concentration in graphene layers decays rapidly with graphene thickness. Das *et al.* reported that the Raman intensity ratio of 2D to G peak is greatly influenced by the electron concentration of graphene [46]. The neutral graphene has the

highest I_{2D}/I_G ratio about 3.2, which decreases with p or n-type doping concentration. The I_{2D}/I_G mapping therefore signals the thickness distribution of graphene layers. In Figure 5.4 (a), the ratio is predominantly in a narrow range of 1.4-2.5, covering more than 95% on the surface. The C-face graphene gives larger I_{2D}/I_G ratio, compared with the FLG (2.7 and 3.3 ML in thickness) on the Si-face SiC, which exhibit the $I_{2D}/I_G < 1.0$ [15]. It is likely that the decoupling of C-face graphene layers by the rotational configuration reduces the electron doping.

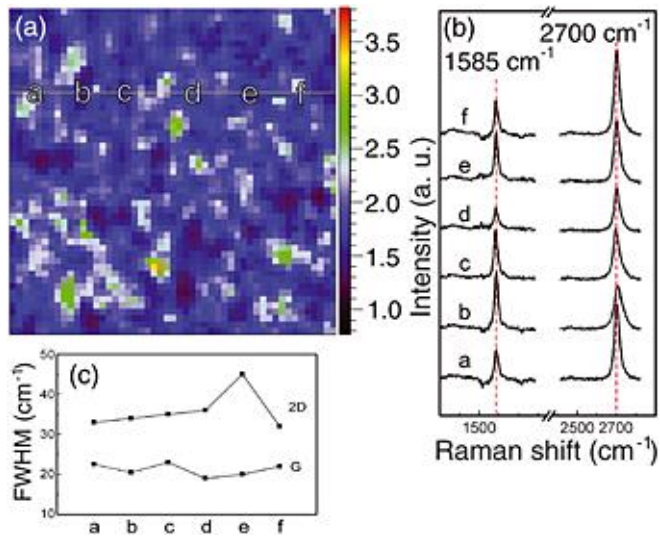


Figure 5.4. (a) $100 \times 100 \mu\text{m}^2$ Raman spectral mapping for 2D/G peak ratio. (b) Raman spectra taken at different positions along a line in (a). (c) Full-width at half-maximum (FWHM) of G and 2D peaks of (b).

Unlike Das's electrolyte/graphene/SiO₂ layered structure, the epitaxial graphene on SiC presents compressive strains resulted from the different coefficients of thermal expansion between SiC and graphene during cooling. It was found that the I_{2D}/I_G ratio of Si-face epitaxial graphene hardly changed with strains despite the significant shift of the peak positions (both G and 2D) [48]. Additionally, the strains in C-face graphene are partially relaxed by forming graphene ridges (unlike graphene on Si-face SiC which rarely contains graphene ridges as shown in Figure 5.6) and expected to be smaller than those on the Si-face.

Figure 5.4 (b) shows the variation of Raman spectra taken from different locations a–f in Figure 5.4 (a). In general, the G and 2D peak positions remain unchanged at approximately 1585 cm^{-1} (G) and 2700 cm^{-1} (2D), respectively. The Raman shift, especially for the G peak, is also sensitive to doping concentration [46, 49]. The invariance of the peak positions means that the FLG has high uniformity in doping concentration and strain distribution. The full-width at half-maximum (FWHM) of G and 2D peak are listed in Figure 5.4 (c). FWHM of G is in the range between 19 and 23 cm^{-1} and that of 2D varies around 35 cm^{-1} . The peak widths are obviously smaller than these in the Si-face FLG [47], but are very close to those of exfoliated neutrality graphene [46]. The peak widths further confirm that the C-face FLG is less doped.

5.4 Surface morphology

The morphology of SiC surfaces was investigated using AFM in tapping mode, which simultaneously provides the topographic and phase images. The as-received SiC, which is mechanically polished, contains considerable wire-like scratches, and the surface roughness is within 4 nm. After graphitization, AFM images of the sample are displayed in Figure 5.5. In the topographic image (Figure 5.5 (a)), it can be seen that the original scratch damages vanished after the graphene growth, and the rough surface contains irregular 3–9-nm steps. The bright, giraffe-patterned stripes are the graphene ridges, with height < 6 nm, which are usually observed in C-face graphene. It should be mentioned that the surface morphology is nearly uniform throughout the graphene region. The phase mapping of AFM can detect variations in composition, adhesion, friction, and viscoelasticity. In the case of epitaxial graphene on SiC, the contrast in phase image originates from both the surface morphology and the material hardness [50]. Figure 5.5 (b) shows the phase image of Figure 5.5 (a). By comparison with the topographic images, the contrast is correlated to the surface morphology, corresponding to graphene ridges (arrow R) and SiC steps (arrow S), respectively. A phase image taken at SiC/graphene boundary is shown in Figure 5.5 (c). The graphene region that contains giraffe pattern is significantly different from the SiC area. From this, we can confirm that the surface in Figure 5.5 (a) is completely covered with graphene.

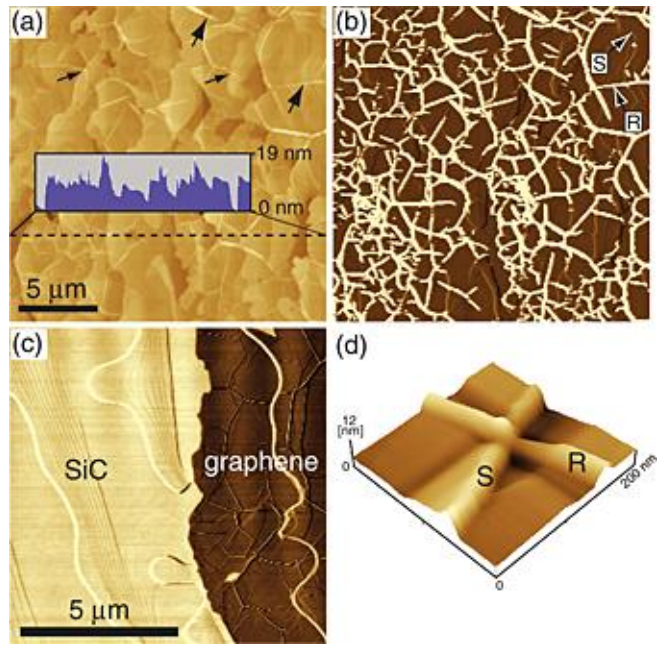


Figure 5.5. Atomic force microscopy images of few-layer graphene (FLG) on 6H-SiC(000–1). (a, b) topographic and corresponding phase images of the surface with fully covered FLG. Inset in (a) shows a height profile along the dotted line. In (b), the arrows indicate the graphene ridges(R) and surface steps (S), respectively. (c) A phase image taken at the SiC/graphene boundary. (d) 3D topographic image of a graphene ridge across a 6-nm step.

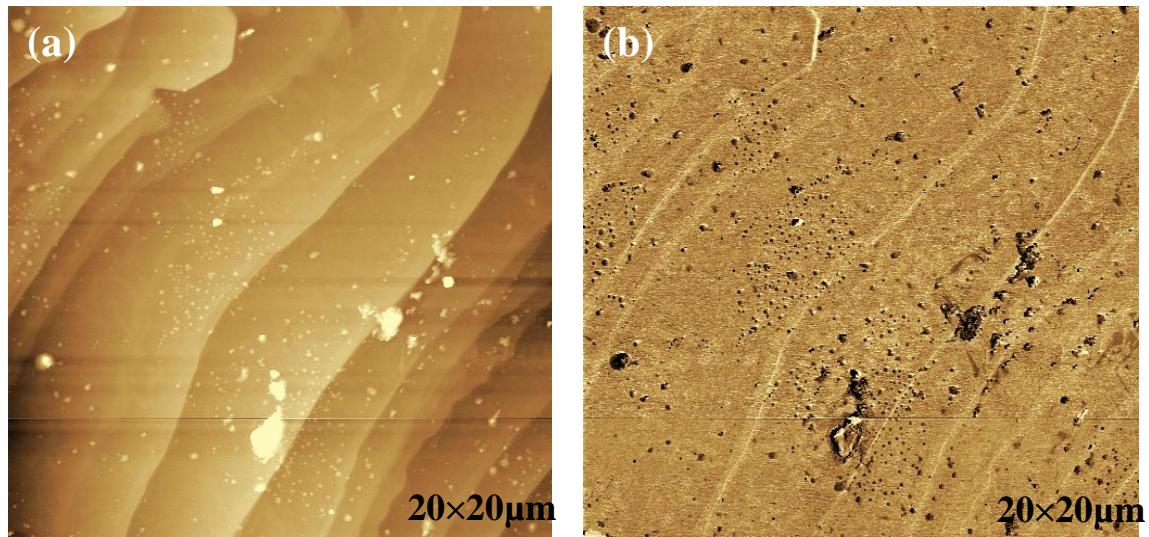


Figure 5.6. AFM topographic (a) and phase (b) images measured on the graphene area above Si-face SiC (0001). The sample was prepared by annealing Si-face SiC (0001) under Ar pressure of 0.3 atm with the graphitization temperature of 1675 °C.

Since the SiC substrate is covered with a few layers of graphene, the surface steps originate mainly from the underlying SiC substrate. Large steps are expected to obstruct the continuous growth, leading to discrete graphene layers. The electrical properties of epitaxial graphene affected by SiC steps have been experimentally verified [51]. For the growth of high-performance graphene, the formation of the large step should be controlled. The decomposition of SiC that generates carbon atoms available to grow graphene results in the SiC depression [52-53]. The local SiC depression leaves behind surface steps, their height being commonly within several nanometers. When annealed under Ar ambience, however, large-height steps are generally observed. Even the growth of monolayer graphene from atomically flat surface causes steps 8-15 nm height [38]. A single layer of graphene requires only 3.14 SiC bilayers to provide carbon atoms [52]. The large-height steps cannot be simply attributed to the SiC depletion, even taking into account the broadened terrace after graphitization. To investigate the effects of Ar-mediated annealing on the surface roughness, we annealed a SiC substrate at 1400 °C under the same Ar pressure for 30 min. Although this annealing temperature is too low to graphitize the SiC, surface steps with height > 10 nm were formed [39]. The Si–C bond can be broken at temperature as low as 1100 °C to form graphene [40]. At higher temperature, which is not enough to graphitize the SiC in the presence of Ar, the SiC surface is in dynamic equilibrium, i.e., the released Si and C atoms recombine on the SiC surface. In minimizing the surface free energy, the self-assembly of Si and C atoms to form SiC results in the formation of broad terraces, and accordingly, the step height increases. A short-time soak at high-temperature region is therefore performed in the present work via the rapid annealing strategy. Although the graphene grown contains few-layer graphene, the surface steps are not higher than those of Si-face monolayer graphene obtained by a long-time annealing [38]. In addition, the graphene ridges climb over the surface steps, as indicated by arrows in Figure 5.5 (a). A three-dimensional (3D) AFM topographic image is shown in Figure 5.5 (d), in which a ridge forms through an 8-nm height step. This suggests that the graphene layers consist of large domains and grow continuously across the steps.

5.5 Conclusions

High quality FLG has been grown on the C-face of 6H-SiC using an Ar-mediated rapid heating method. The graphene layers are of high uniformity with an average thickness of 3 ML. Raman spectra of FLG measured at different locations show that the peak positions remain invariable at 1585 cm^{-1} (G band) and 2700 cm^{-1} (2D band). The values of I_{2D}/I_G ratio almost invariant, i.e. they are in the narrow range between 1.4 and 2.5. After the graphene growth, the surface is modified by wide terraces with 3–9-nm height steps, and the FLG continuously extends across the steps to form large-scaled grains.

References for chapter 5

- [32] Z. Sun, Z. Yan, J. Yao, E. Beitler, Y. Zhu, J. M. Tour, *Nature*, 468, 549 (2010).
- [33] P. Sutter, *Nat. Mater.*, 8, 171 (2009).
- [34] E. Pearson, T. Takai, T. Halicioglu, W. A. Tiller, *J. Cryst. Growth*, 70, 33 (1984).
- [35] L. Muehlhoff, W. J. Choyke, M. J. Bozack, J. T. Yates, *J. Appl. Phys.*, 60, 2842 (1986).
- [36] D. L. Miller, K. D. Kubista, G. M. Rutter, M. Ruan, W. A. de Heer, P. N. First, J. A. Stroscio, *Science*, 324, 924 (2009).
- [37] K. V. Emtsev, A. Bostwick, K. Horn, J. Jobst, G. L. Kellogg, L. Ley, J. L. McChesney, T. Ohta, S. A. Reshanov, J. Rohrl, E. Rotenberg, A. K. Schmid, D. Waldmann, H. B. Weber, T. Seyller, *Nat. Mater.*, 8, 203 (2009).
- [38] C. Virojanadara, M. Syvajarvi, T. Yakimova, L. I. Johansson, *Phys. Rev. B*, 78, 245403 (2008).
- [39] H. Hu, A. Ruammaitree, H. Nakahara, K. Asaka, Y. Saito, *Surf. Interface Anal.*, 44, 793 (2012).
- [40] I. Forbeaux, J.-M. Themlin, J.-M. Debever, *Surf. Sci.*, 442, 9 (1999).
- [41] F. Hiebel, P. Mallet, F. Varchon, L. Magaud, J.-Y. Veuillen, *Phys. Rev. B*, 78, 1533412 (2008).

- [42] R. J. Nemanich, S. A. Solin, Phys. Rev. B, 20, 392 (1979).
- [43] A. C. Ferrari, J. C. Meyer, V. Scardaci, C. Casiraghi, M. Lazzeri, F. Mauri, S. Piscanec, D. Jiang, K. S. Novoselov, S. Roth, A. K. Geim, Phys. Rev. Lett., 97, 187401 (2006).
- [44] J. Hass, F. Varchon, J. E. Millan-Otoya, M. Sprinkle, N. Sharma, W. A. de Heer, C. Berger, P. N. First, L. Magaud, E. H. Conrad, Phys. Rev. Lett., 100, 125504 (2008).
- [45] C. Riedl, C. Coletti, T. Iwasaki, A. A. Zakharov, U. Starke, Phys. Rev. Lett., 103, 246804 (2009).
- [46] A. das, S. Pisana, B. Chakraborty, S. Piscanec, S. K. Saha, U. V. Waghmare, K. S. Novoselov, H. R. Krishnamurthy, A. K. Geim, A. C. Ferrari, A. K. Sood, Nat. Nanotech., 3, 210 (2008).
- [47] N. Sharma, D. Oh, H. Abernathy, M. Liu, P. N. First, T. M. Orlando, Surf. Sci., 604, 84 (2010).
- [48] N. Ferralis, R. Maboudian, C. Carraro, Phys. Rev. Lett., 101, 156801 (2008).
- [49] J. Yan, Y. Zhang, P. Kim, A. Pinczuk, Phys. Rev. Lett., 98, 166802 (2007).
- [50] F. J. Ferrer, E. Moreau, D. Vignaud, D. Deresmes, S. Godey, X. Wallart, J. Appl. Phys., 109, 054307 (2011).
- [51] M. K. Yakes, D. Gunlycke, J. L. Tedesco, P. M. Campbell, R. L. Myers-Ward, C. R. Eddy Jr., D. K. Gaskill, P. E. Sheehan, A. R. Laracuente, Nano Lett., 10, 1559 (2010).
- [52] J. Hass, W. A. de Heer, E. H. Conrad, J. Phys. Condens. Matter, 20, 323202 (2008).
- [53] J. L. Tedesco, G. G. Jernigan, J. C. Culbertson, J. K. Hite, Y. Yang, K. M. Daniels, R. L. Myers-Ward, C. R. Eddy Jr., J. A. Robinson, K. A. Trumbull, M. T. Wetherington, P. M. Campbell, D.K. Gaskill, Appl. Phys. Lett., 96, 222103 (2010).

Chapter 6

Growth of Embedded and Protrusive Striped Graphene on Si-terminated 6H-SiC (0001)

The formation of epitaxial graphene was originally accomplished by annealing the Si-face 6H-SiC in ultrahigh vacuum (UHV). It is already known that the growth of epitaxial graphene under this condition gives us the embedded graphene in SiC substrate. Kageshima *et al.* [54] show that an embedded structure is energetically preferable by using a first-principle calculation method. In addition, the edges of graphene islands with this embedded structure have no broken dangling bonds. Namely, C atoms at graphene edge bond with Si or C atoms of the SiC substrate. In this chapter, we have demonstrated the growth of embedded and protrusive striped graphene on Si-terminated 6H-SiC (0001) by annealing the SiC substrates under Ar atmosphere. This method can keep the graphene edge intact. In addition, carrier concentration and strain of graphene film are characterized by Raman and angle-resolved photoemission spectroscopy.

6.1 Experimental

N-type Si-terminated 6H-SiC (0001) substrates were employed and first cleaned by ultrasonic precleaning with acetone. After that the substrates were put in a main chamber with the base pressure of $\sim 10^{-8}$ Pa and deposited by Si atoms around 2 layers. Then the substrates were transferred, without exposure to air, to another annealing chamber, and annealed by resistive heating under Ar

gas pressure of 0.05 and 0.3 atm. The annealing temperature was in a range from ~900 to graphitization temperature (1550 °C for 0.05 atm sample and 1675 °C for 0.3 atm sample) with steps of ~100 °C (10~15 minutes per each step). The annealing temperature was measured by an optical pyrometer.

After annealing, reflection high-energy electron diffraction (RHEED) which has incident beam energy of 10 kV was employed to measure the structure of SiC surface in the main chamber (base pressure of ~ 10^{-8} Pa). The topography of samples was measured by atomic force microscopy (AFM) in air. An ultra-high vacuum scanning electron microscope (UHV-SEM) which has incident beam of 2.2 keV was performed to confirm the shape and position of graphene. Raman spectroscopy was performed at room temperature with the 532 nm excitation laser. Angle-resolved photoemission spectroscopy (ARPES) measurement was conducted at room temperature at the beam line 5U of UVSOR-II in the Institute for Molecular Science, Okazaki, Japan. The excitation photon energy was set to 80 eV.

6.2 Structure of graphene on Si-face 6H-SiC (0001) measured by RHEED

After annealing, the samples were transferred to measure the evolution of the surface structure by RHEED. The results show that in the case of the sample which annealed under Ar pressure of 0.05 atm (0.05 atm sample) the structure of SiC (0001) evolves from $1\times1 \rightarrow \sqrt{3}\times\sqrt{3} \rightarrow 6\times6$ reconstruction at the annealing temperature of 1500 °C and 1550 °C, respectively, as shown in Table 6.1. Figure 6.1 shows RHEED patterns after annealing the sample at 1100°C ((a) and (b)), 1500°C ((c) and (d)) and 1550°C ((e) and (f)). Figure 6.2 shows schematics of RHEED patterns in a unit cell before the graphitization. In the case of 1×1 reconstruction (Figure 6.2 (a)), diffraction spots appear only at the SiC spots (00), (01), (10) and (11). For the $\sqrt{3}\times\sqrt{3}$ reconstruction, there are two additional diffraction spots appearing between the (00) and (11) spots as shown in Figure 6.2 (b). Figure 6.3 (a) displays a large area of RHEED pattern measured after annealing at the graphitization temperature (1550 °C). RHEED patterns of graphene layer over the SiC (Figure 6.1 (e) and (f) and Figure 6.3 (a)) reveal that the reflections from graphene appears around (0.72, 0.72) and

$(\overline{0.72}, \overline{0.72})$ spots when the incident beam is applied in the $[\bar{1}010]$ direction [56]. In addition, when the sample is rotated by 30 degree ($[\bar{1}\bar{1}20]$ incidence), the reflections from graphene are observed near $(0, \pm 2)$ spots. Figure 6.3 (b) shows a schematic of the reciprocal lattice of 6×6 reconstruction where a green dash line rhombohedron represents a graphene unit cell which has the different angle of 30 degree from a SiC unit cell (black dot line).

In the case of annealing under Ar pressure of 0.3 atm (0.3 atm sample), the structure changes from $1\times 1 \rightarrow 3\times 3 \rightarrow 6\times 6$ reconstruction after annealing at the temperature of 1300 °C and 1675 °C, respectively, as shown in Table 6.1. Figure 6.4 shows RHEED results after annealing at 900°C ((a) and (b)), 1625°C ((c) and (d)) and 1675°C ((e) and (f)) under Ar pressure of 0.3 atm. In the case of 3×3 , there are 2 diffraction spots appearing between the (00) and (11) spots and between (00) and (01) spots as indicated by circles in Figure 6.4 ((c) and (d)). Table 6.1 also shows that the graphitization temperature of 0.3 atm sample is higher around 125°C than that of 0.05 atm sample. The shift of this graphitization temperature can be attributed to the reduction of Si sublimation. Namely, the presence of higher pressure of Ar gas increases probability of Si collision with Ar atoms, leading to the increase of the number of Si atoms reflecting back to the surface. Therefore, the higher annealing temperature is needed for the graphitization of 0.3 atm sample.

Table 6.1. Surface structures of Si-face SiC which was annealed under Ar pressure of 0.05 atm and 0.3 atm at each annealing temperature.

Temperature (°C)	Structure (Ar 0.05atm)	Structure (Ar 0.3atm)
900	(1×1)	(1×1)
1000	(1×1)	(1×1)
1100	(1×1)	(1×1)
1200	(1×1)	(1×1)
1300	(1×1)	(3×3)
1400	(1×1)	(3×3)
1500	$(\sqrt{3} \times \sqrt{3})$	(3×3)
1550	(6×6)	(3×3)
1575		(3×3)
1625		(3×3)
1675		(6×6)

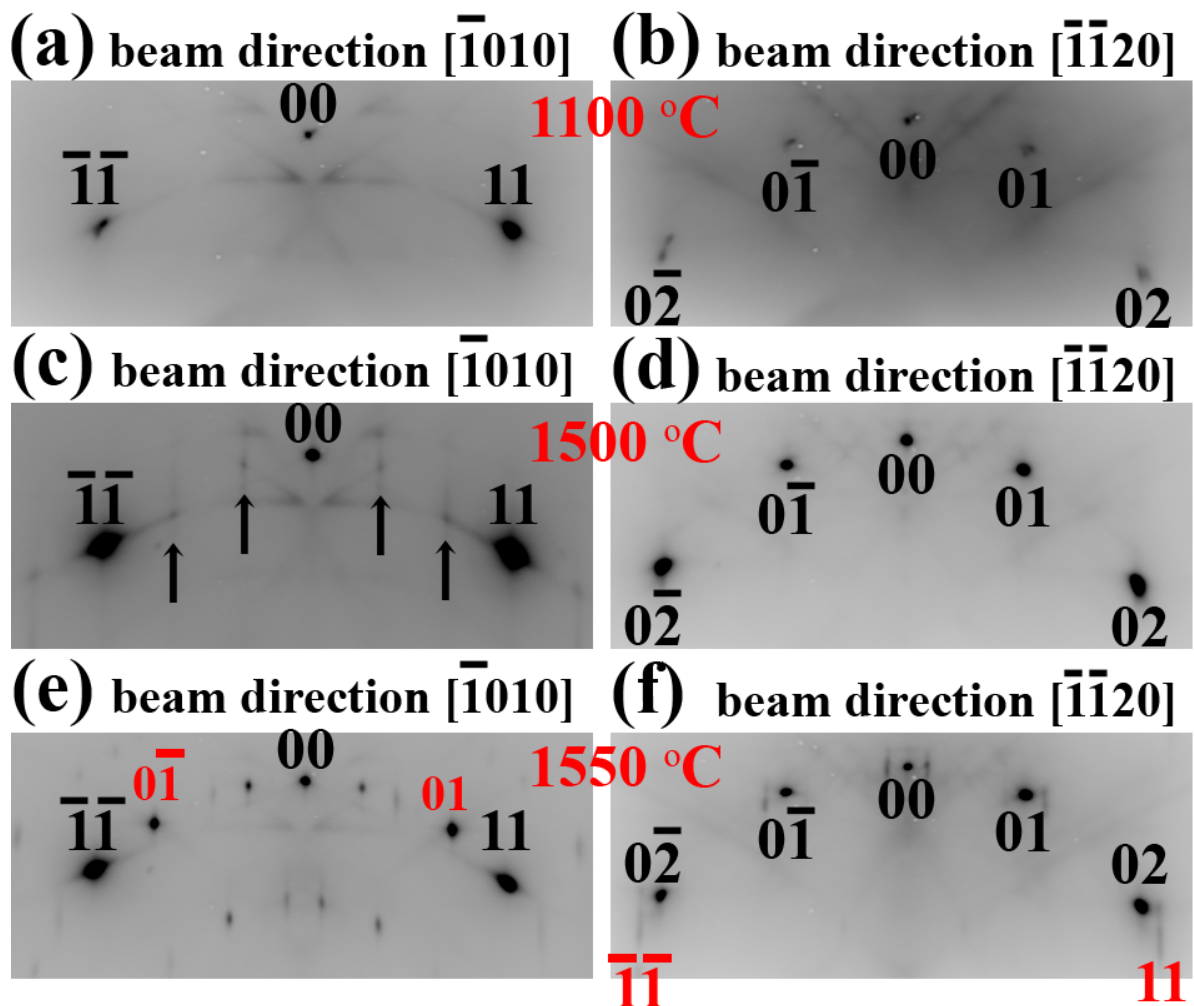


Figure 6.1. RHEED patterns from SiC (0001) which was annealed under Ar pressure of 0.05 atm at 1100 °C (a and b), 1500 °C (c and d) and 1550 °C (e and f) showing 1×1, $\sqrt{3} \times \sqrt{3}$ and 6×6 reconstruction (respectively) with the beam direction of $[\bar{1}010]$ (a, c and e) and $[\bar{1}\bar{1}20]$ (b, d and f). Red and black indexes indicate reflections from graphene and SiC substrate, respectively.

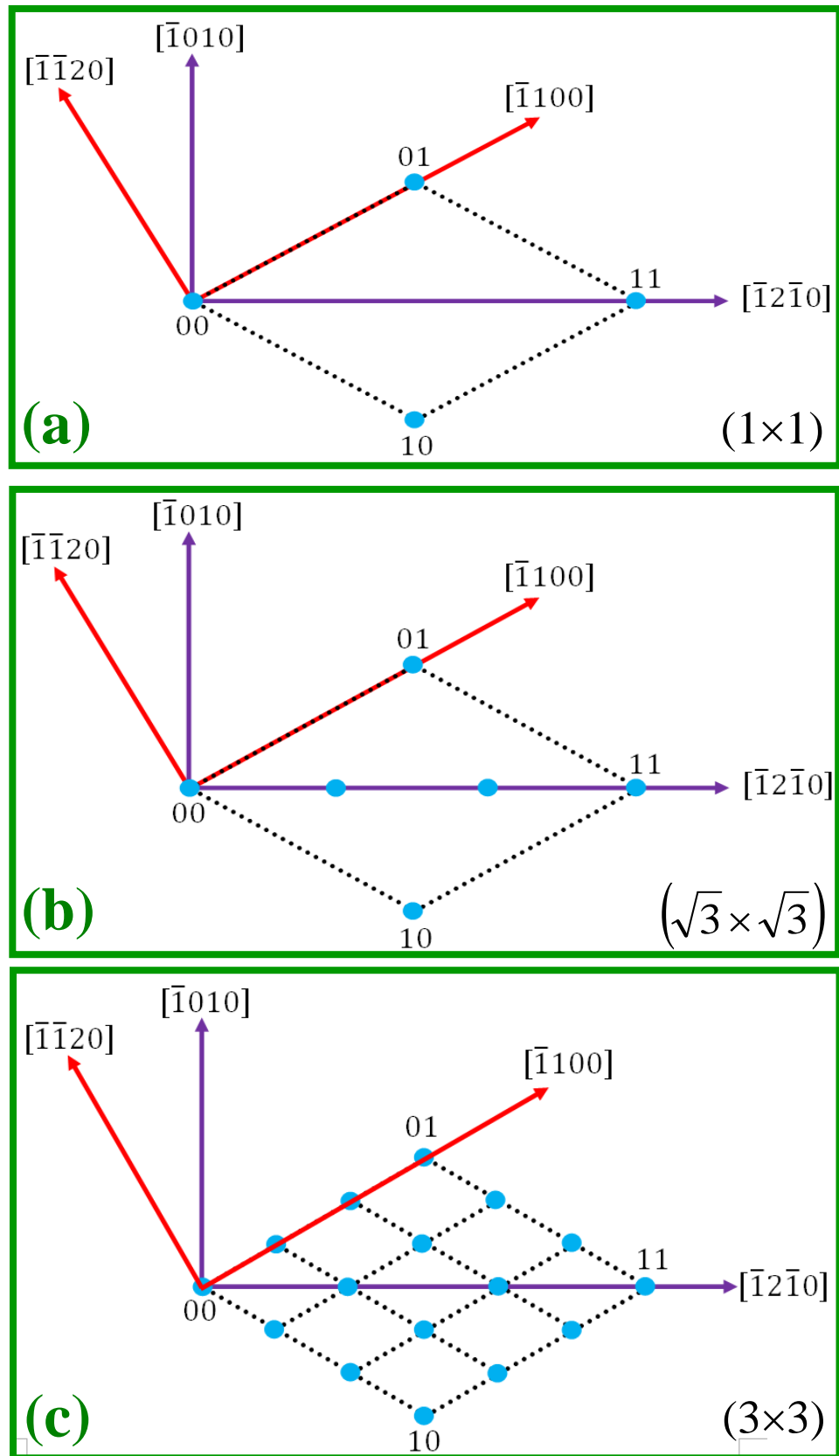


Figure 6.2. Schematics of RHEED patterns in the case of (a) 1×1 , (b) $\sqrt{3} \times \sqrt{3}$ and (c) 3×3 reconstruction. Blue balls represent reciprocal point.

Beam direction $[\bar{1}010]$

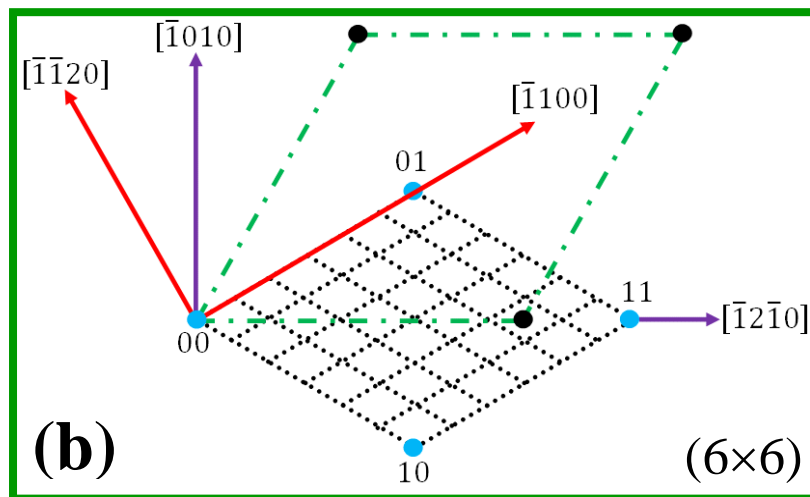
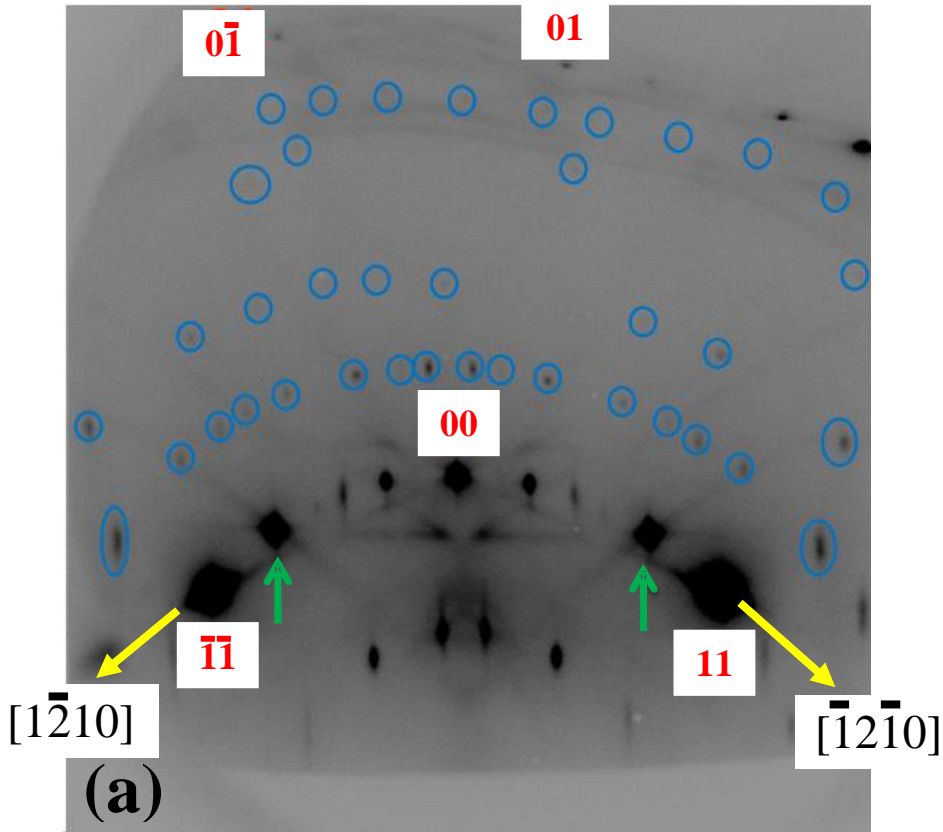


Figure 6.3. (a) RHEED patterns from the SiC (0001) which was annealed at graphitization temperature (1550 °C) under Ar pressure of 0.05 atm. Blue circles indicate superlattice reflection spots. Green arrows are pointing to the diffraction from graphene lattice. (b) Schematic of reciprocal lattices of 6×6 reconstruction. Blue and black balls represent reciprocal lattice point from 1×1 SiC and graphene surface, respectively.

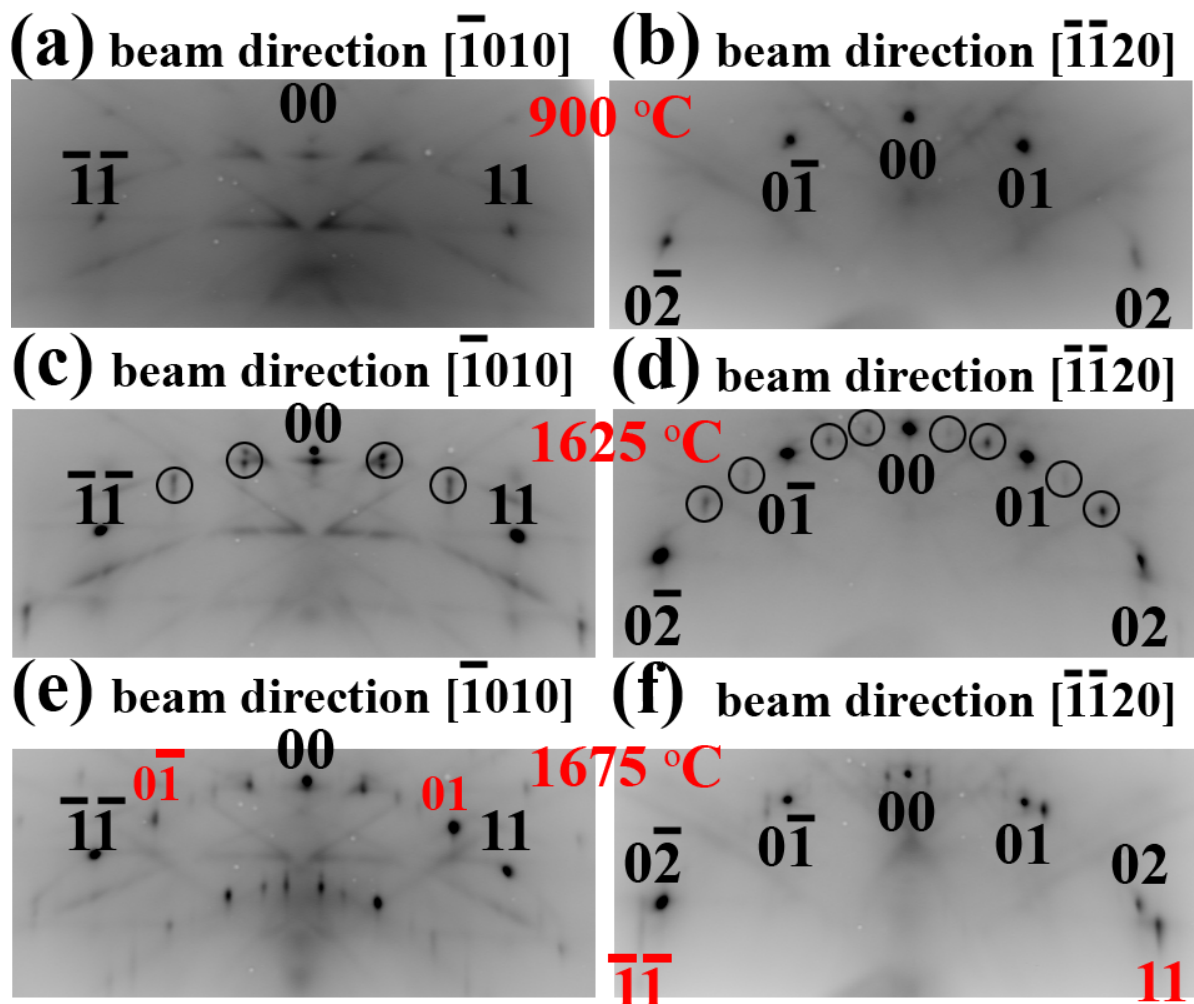


Figure 6.4. RHEED patterns from the SiC (0001) which was annealed under Ar pressure of 0.3 atm at 900 °C (a and b), 1625 °C (c and d) and 1675 °C (e and f) showing 1×1, 3×3 and 6×6 reconstruction, respectively. Azimuth of the incident beam are $[\bar{1}010]$ (a, c and e) and $[\bar{1}\bar{1}20]$ (b, d and f). Red and black indexes indicate the positions of reflections from graphene and SiC substrate, respectively.

6.3 Growth of embedded and protrusive striped graphene on Si-face SiC (0001)

In this study, we annealed the SiC substrates by resistive heating method. This method provides us with a non-uniform distribution of temperature on the SiC substrates, which leads to a systematic distribution of graphene thickness on the sample. This method also gives us opportunities for measuring the graphene morphology and shape from their initial state. Figure 6.5 shows AFM images of the 0.05 atm ((a) and (b)) and 0.3 atm samples ((c) and (d)). In the case of 0.05 atm sample, AFM topographic and phase images (Figure 6.5 (a) and (b), respectively) reveal that bright regions in Figure 6.5 (b) are the position of graphene regions. The graphene regions are lower than their terrace, as shown clearly by the line profiles along the black line (Figure 6.5 (a) inset). We also found that the graphene is first nucleated at the upper step edge. It is attributed to the SiC decomposition which prefers to occur at the step edge due to the instability of the step edge. SEM image (Figure 6.6 (a)) shows three distinctive SEM contrasts, i.e., bright, dark gray and black (narrow striped line) indicating buffer layer, monolayer and bilayer graphene, respectively [57]. SEM results confirm the bright region in AFM phase image (Figure 6.5 (b)) is graphene regions. For annealing the 0.3 atm sample, Figure 6.5 (c) and (d) shows graphene morphology and shape measured at the beginning state of graphene growth. These AFM results reveal that graphene is first grown at the upper step edge. The AFM topography line profile along the black line (inset in Figure 6.5 (c)) shows the position of graphene region at the upper step edge is about 1.2 nm higher than that of SiC region on the same terrace. AFM phase (Figure 6.5 (d)) and SEM (Figure 6.6 (b)) images confirm the protrusive area at upper step edge is graphene region. Although, the height of the protrusive area implies that this region should contain a buffer layer and 3 graphene layers, the thickness measurement using X-ray diffraction (XRD) reveals the presence of graphene monolayer, bilayer and trilayer on this sample are 40%, 25% and 10%, respectively [57]. Since the area in Figure 6.5 (c) and (d) was measured around the beginning state of graphene growth, the graphene thickness on the protrusive region should be graphene monolayer. It implies that the protrusive area consists of SiC layers stacking at the base and a buffer layer and graphene monolayer terminating on the top.

In addition, we use Raman spectroscopy to confirm the thickness of the protrusive striped graphene on the 0.3 atm sample. Since Raman 2D peak originates from Dirac cone, the appearance of Raman 2D peak can confirm the presence of graphene inside the Raman laser beam spot. Figure 6.7 (a) shows an optical image of 0.3 atm sample at the boundary between SiC and graphene regions. Figure 6.7 (b) shows the relation between intensities of 2D peak and positions along the yellow line in Figure 6.7 (a). The relation shows that the intensity of 2D peak is high in graphene region and it becomes lower near the boundary. Finally, the intensity of 2D peak becomes the lowest outside graphene region (in SiC region). The variance of 2D peak intensity is attributed to size of graphene area inside the Raman beam spot. In the graphene region, graphene area is larger than Raman laser beam spot ($\sim 1 \mu\text{m}$) therefore the intensity of the 2D peak in this region is high. At the boundary, the graphene size is smaller than Raman laser beam spot hence the intensity of Raman 2D peak is lower than that in graphene region.

It is well known that the 2D peak shape depends on graphene thickness. For example, if the shape of 2D peak is explained by one Lorentzian function curve, it implies that this graphene film thickness is monolayer. In the case of bilayer graphene, the 2D peak shape is broader than that in the case of graphene monolayer. The 2D peak shape of bilayer graphene may be explained by four Lorentzian function curves. Figure 6.7 (c) shows Raman spectra measured at the position (-500,0). Figure 6.7 (c) inset shows a calculated curve fit on experimental data at 2D peak by using only one Lorentzian function curve, and implies that graphene film thickness on this region is monolayer graphene. The 2D peak shape along the yellow line in Figure 6.7 (a) is also investigated every 50 μm . We can observe only monolayer graphene from the boundary to 500 μm the graphene region. Raman results correspond with XRD and SEM results which reveal that the thickness of the protrusive striped graphene near the boundary region between SiC and graphene is graphene monolayer.

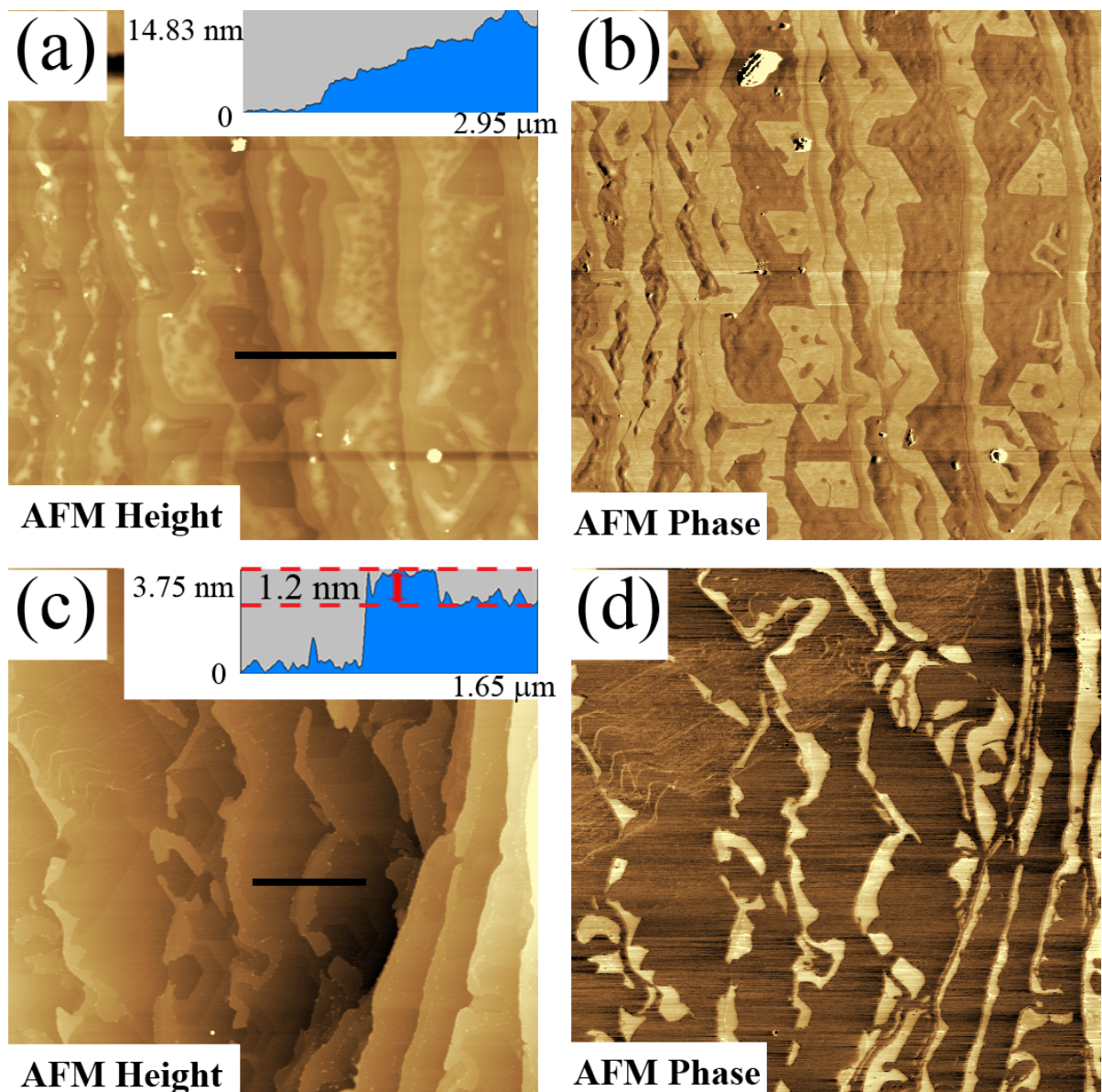


Figure 6.5. $10 \times 10 \mu\text{m}^2$ AFM images of (a) and (b) 0.05 atm and (c) and (d) 0.3 atm samples. Inset in (a) and (c) show line profiles along black lines. Bright regions in AFM phase image (b and d) indicate graphene regions.

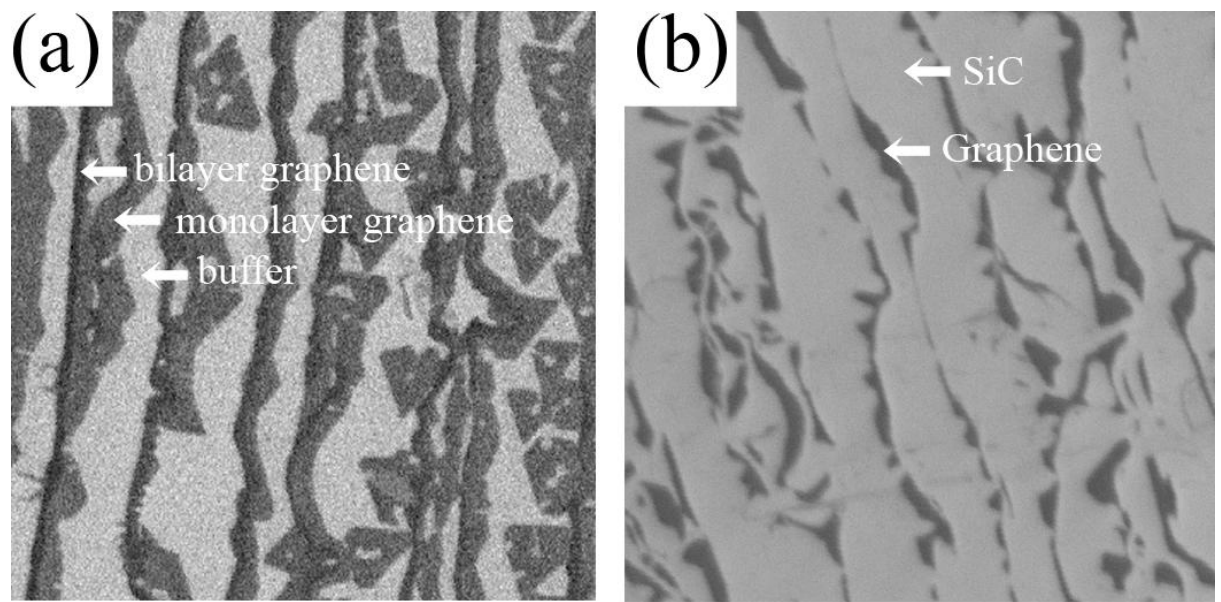


Figure 6.6. $10 \times 10 \mu\text{m}^2$ SEM image of (a) 0.05 atm and (b) 0.3 atm sample taken with acceleration voltage of 2.2 keV.

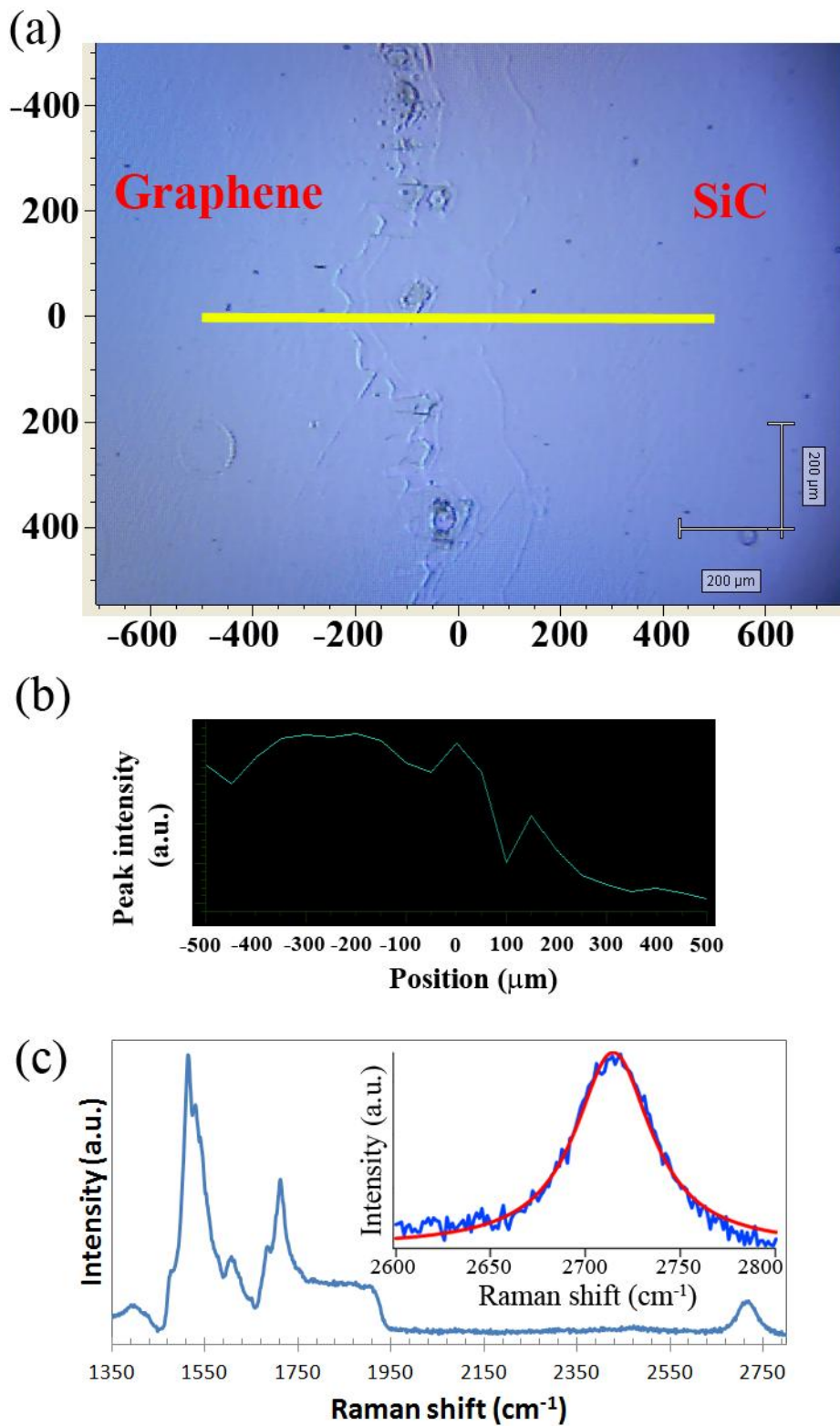


Figure 6.7. (a) 0.3 atm sample image measured at the boundary between SiC and graphene by optical microscope. (b) Intensities of the 2D peak which vary in positions along the yellow line in (a). (c) Raman spectra measured at position (-500,0). Inset shows Raman spectra at 2D peak (blue curve) and fitting curve (red curve).

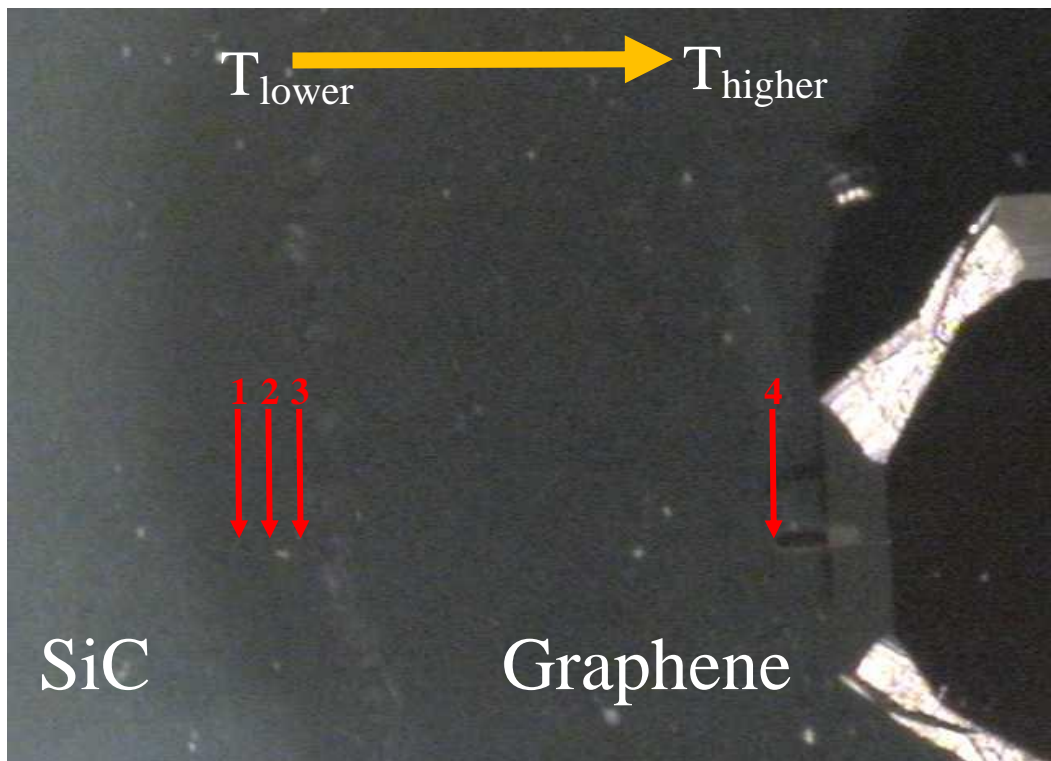


Figure 6.8. Optical microscope image measured on the 0.3 atm sample displaying the positions that are measured by AFM. AFM images at position 1, 2, 3 and 4 are presented in Figure 6.5 (c and d), Figure 6.9 (a and b), Figure 6.9 (c and d) and Figure 6.9 (e and f).

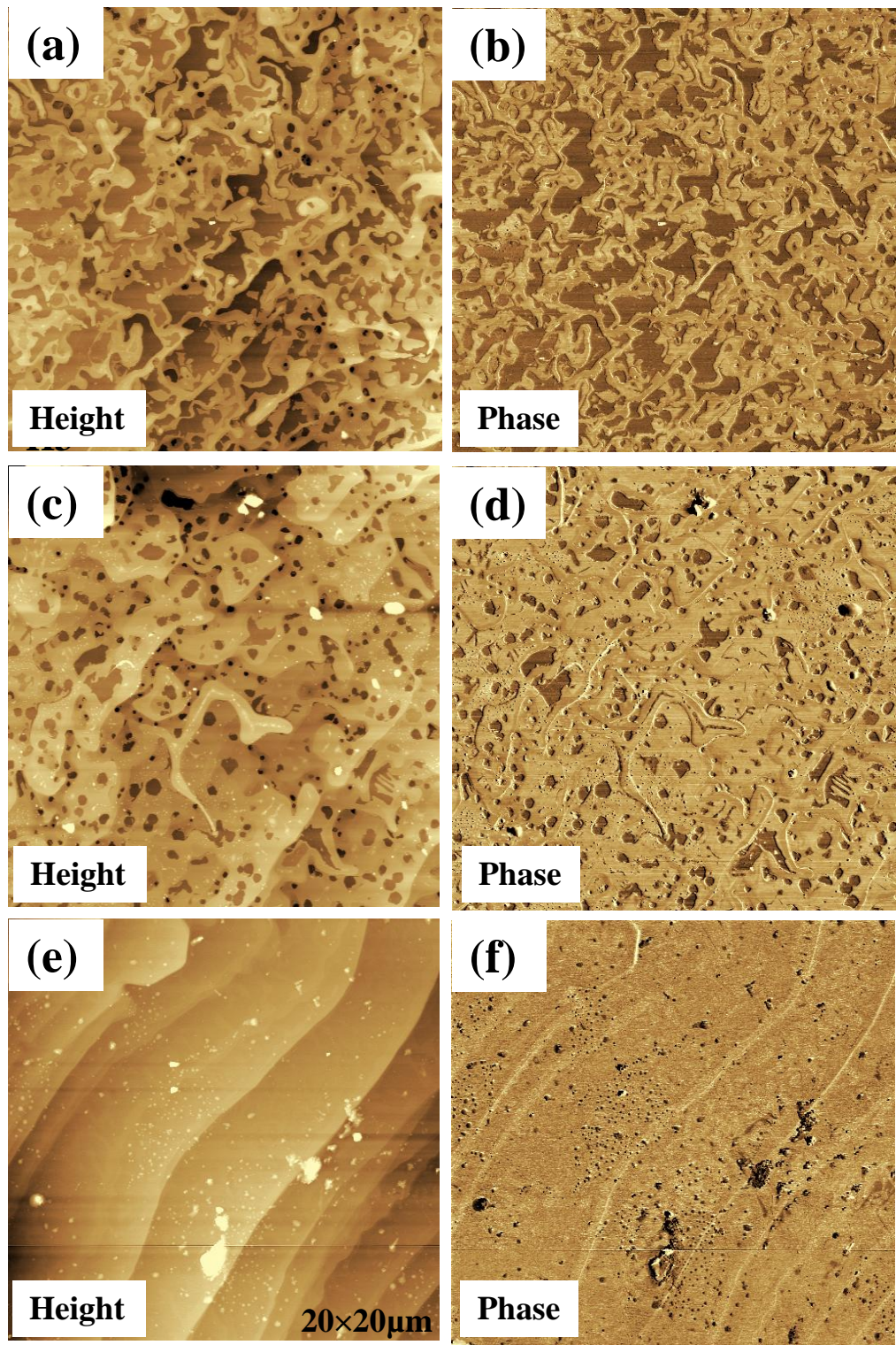


Figure 6.9 AFM $20\times20\mu\text{m}^2$ topographic (a, c and e) and phase (b, d and f) images.

In general, formation of embedded graphene on Si-terminated 6H-SiC is commonly found [58] but the growth of protrusive graphene is rare because it needs higher energy for C diffusion to incorporate and form graphene. Figure 6.9 displays the growth of protrusive graphene on SiC substrate at higher annealing temperature regions by AFM measurement. The positions of AFM measurement are shown in Figure 6.8. At the beginning, narrow SiC steps bunch on the sample surface. After that the protrusive graphene strips are formed at the upper-side step edge (Figure 6.5 (c) and (d)). Then the size of protrusive graphene becomes larger and larger, as shown in Figure 6.9 ((a) and (b)) and Figure 6.9 ((c) and (d)), respectively. Finally, the protrusive graphene completely covers the SiC substrate. The terrace width is obviously wider than the terrace width at the initial state, as shown in Figure 6.9 ((e) and (f)).

Here, I propose models of the graphene growth process. Figure 6.11 shows schematics of graphene growth process for 0.05 atm (Figure 6.11 (b)) and 0.3 atm (Figure 6.11 (c)) samples. A schematic in Figure 6.11 (a) shows the bunching steps, which appear on both samples, before graphene nucleation. In the case of 0.05 atm sample (Figure 6.11 (b)), the SiC substrate is first decomposed at upper step edge. Si atom sublimation leaves behind free C atoms on the lowered area. After that those free C atoms incorporate and nucleate buffer and graphene layer, consecutively. Since the graphene position of this sample is lower than the position of SiC substrate on the same terrace, therefore it is possible that C atoms at the edge of carbon layer (buffer and graphene layer) bond with Si or C atoms of the SiC substrate to reduce the total energy [59]. For 0.3 atm sample (Figure 6.11 (c)), which were annealed under higher graphitization temperature than 0.05 atm sample, the free C and Si atoms which were released from the SiC decomposition diffuse and incorporate at the step edge. Free C and Si atoms can be confined at step edge due to the Schwoebel-Ehrlich barrier, i.e., For free atoms migrating on a terrace, the number of nearest neighbor atoms at the top edge of the step is lower than that on the terrace. This leads to the occurrence of addition diffusion barrier at the step edge as shown in Figure 6.10. This addition diffusion barrier is called Schwoebel-Ehrlich barrier [60,61]. The free C and Si atoms prefer to be trapped around the edge. After many free atoms stopped at the step edge, subsequent free atoms will upward hop on top the previous trapped atoms. After that the Si atoms on top start to sublimate and then the first carbon layer on top is formed by remaining free C atoms. Since the position of the graphene is higher than that of bare SiC terrace, there is no bonding between graphene edge and the SiC substrate. It means we

can fabricate striped graphene with intact edges which near free standing graphene on SiC.

In this section, we describe about two types of graphene growth on SiC (0001), i.e., embedded and protrusive graphene. The type of graphene growth can be controlled by Ar pressure. Namely, if the SiC (0001) is annealed under argon pressure of 0.05 atm, epitaxial graphene film will be embedded in the SiC substrate. On the other hand, if the SiC (0001) is annealed under argon pressure of 0.3 atm, the protrusive graphene on SiC substrate is obtained.

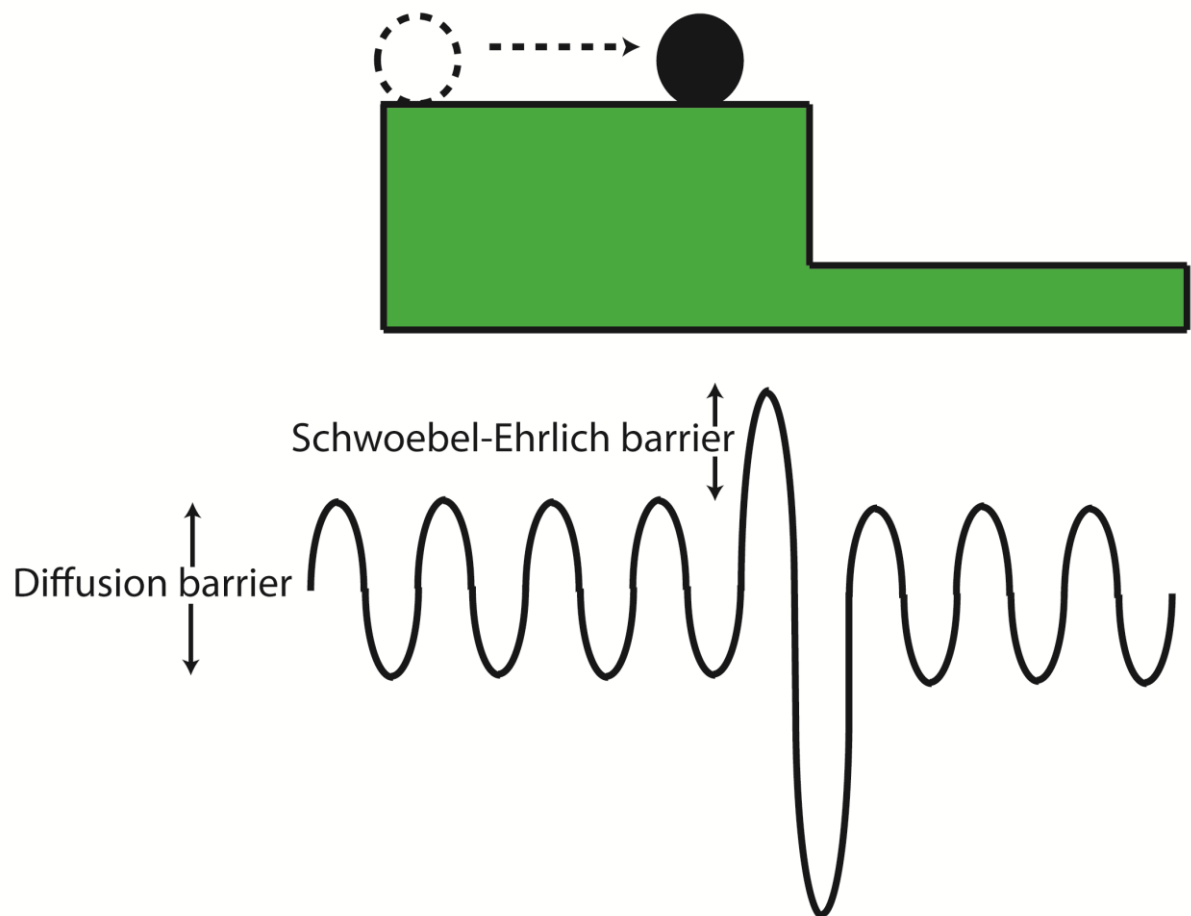


Figure 6.10. Schematic of surface topography (above) and diffusion barrier (below). A black solid circle represents a free atom which diffuses from the terrace to a step edge.

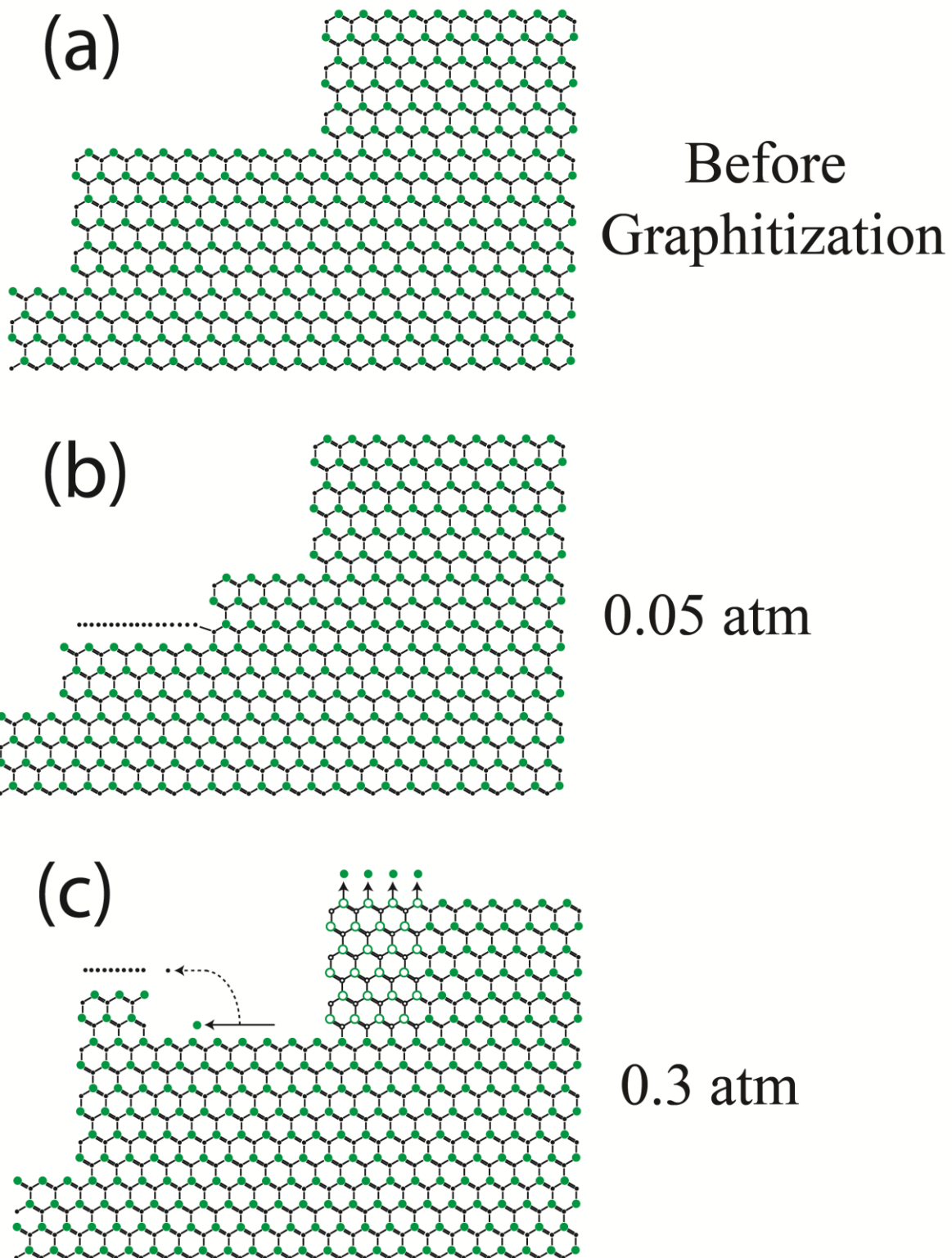


Figure 6.11. Schematic of graphene growth process showing bare SiC surface with bunching step (a), embedded (b) and protrusive (c) carbon layer at SiC step edge. Small and big circles indicate carbon and silicon atoms, respectively.

6.4 Raman characterization

In this section, an electron carrier concentration and strain of embedded (0.05 atm sample) and protrusive (0.3 atm sample) graphene are investigated by Raman measurement. Figure 6.12 shows Raman spectra of 0.05 atm (green solid line) and 0.3 atm (blue solid line) samples after the subtraction of SiC spectra. The position of G peak (near 1600 cm^{-1}) can be measured and is approximately the same for both samples. The inset in the figure shows the magnification of 2D peak around 2700 cm^{-1} . The 2D peak position for the embedded graphene (0.05 atm sample) is slightly blue shifted (around 20 cm^{-1}) with respect to the protrusive sample (0.3 atm sample).

For the electron carrier concentration, the charge doping of graphene can change the G peak position [63-65]. The G peak positions in the two samples are approximately same. It suggests that the carrier concentration of embedded and protrusive graphene is identical. It is corresponding to angle-resolved photoemission spectroscopy (ARPES) results (Figure 6.12 (b) and (c)) showing the same doping level for both samples.

In the case of graphene film strain, Mohiuddin research group found that the strain on graphene film can change the position of G and 2D peaks [66]. In our case, the positions of G peaks of the embedded and protrusive graphene are nearly same but only the 2D peaks of both samples are slightly different. These suggest that the both samples contain approximately the same strain even though there are the bonds between graphene edge and SiC substrate in the case of embedded graphene.

In addition, the graphene film thickness is also determined by fitting the 2D peak. As the number of graphene layer relates to the number of the combination of 2D peak, i.e., 2D peak consists of 1 and 4 combination peaks for graphene monolayer and bilayer, respectively. Figure 6.12 inset shows that the combination of 2D peak for 0.05 and 0.3 atm sample are 1 and 4 combination curves, respectively implying that the thickness of 0.05 and 0.3 atm sample at the Raman measurement area are graphene monolayer and bilayer, respectively.

The above analysis reveals that the types of graphene (embedded and protrusive graphene) do not affect on electron concentration and graphene strain.

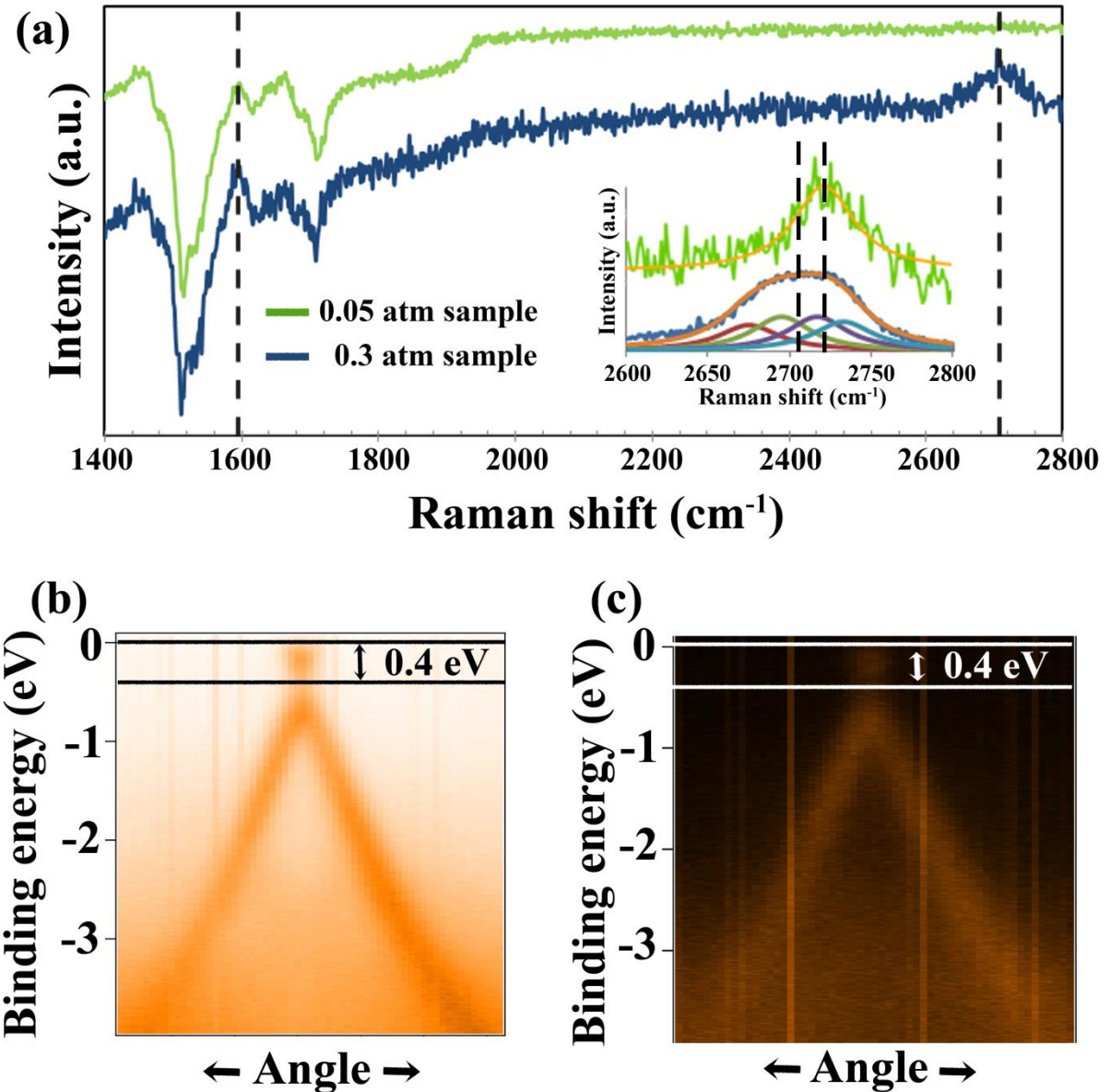


Figure 6.12. (a) Raman spectra after subtracting of SiC spectra. Green and blue solid lines indicate the samples annealed under Ar pressure of 0.05 atm and 0.3 atm, respectively. (a) Inset: magnification of Raman spectra at the 2D peak region. Orange curves are simulation curves. (b) and (c) ARPES spectra of the 0.05 atm and 0.3 atm sample (respectively) showing Dirac cone around the K point of graphene.

6.5 Conclusion

I have grown and investigated the epitaxial embedded and protrusive striped graphene on Si-terminated 6H-SiC (0001). We found that the

graphitization temperature rises from 1550 °C to 1675 °C with increment of Ar pressure from 0.05 atm to 0.3 atm. Graphene unit cell for both samples has rotated by 30 degree from SiC unit cell. In addition, graphene prefers to be grown and embedded at step edge for 0.05 atm sample. In the case of 0.3 atm sample, free C and Si atoms which are released from the SiC decomposition diffuse to the step edge and nucleate protrusive graphene layer there. Raman peak characteristics and ARPES spectra reveal that the embedded and protrusive graphene have approximately the same carrier concentration and graphene film strain.

References for chapter 6

- [54] H. Kageshima, H. Hibino, M. Nagase, Y. Sekine, H. Yamaguchi, Jap. J. of Appl. Phys, 50, 070115 (2011).
- [55] A. Ruamrao, H. Nakahara, K. Soda, Y. Saito, “Growth of Embedded and Protrusive Striped Graphene on 6H-SiC (0001)”, International Journal of Engineering and Innovative Technology, 3, 34, (2014).
- [56] A. Charrier et al., “Solid-state decomposition of silicon carbide for growing ultra-thin heteroepitaxial graphite films,” J. Appl. Phys., 92, 2479 (2002).
- [57] A. Ruamrao, H. Nakahara, K. Akimoto, K. Soda, and Y. Saito, “Determination of non-uniform graphene thickness on SiC (0001) by X-ray diffraction,” Appl. Surf Sci, 282, 297 (2013).
- [58] S. W. Poon, W. Chen, A. T. S. Wee and E. S. Tok, “Growth dynamics and kinetics of monolayer and multilayer graphene on a 6H-SiC(0001) substrate”, Phys. Chem. Chem. Phys., 12, 13522 (2010).
- [59] H. Kageshima, H. Hibino, M. Nagase, Y. Sekine, and H. Yamaguchi, “Theoretical Study on Magnetoelectric and Thermoelectric Properties for Graphene Devices,” Jap. J. Appl. Phys., 50, 070115 (2011).
- [60] S. A. Alexander, “Ehrlich–Schwoebel barrier”,
<http://eng.thesaurus.rusnano.com/wiki/article555>.

- [61] R. L. Schwoebel, “Step motion on crystal surfaces”, J. Appl. Phys. 37, 3682 (1966).
- [62] M. L. Bolen, R. Colby, E. A. Stach, and M. A. Capano, “Graphene formation on step-free 4H-SiC (0001),” Journal of Applied Physics 110, 074307 (2011).
- [63] Jun Yan, Yuanbo Zhang, Philip Kim, and Aron Pinczuk, “Electric Field Effect Tuning of Electron-Phonon Coupling in Graphene”, Phys. Rev. Lett. 98, 166802 (2007).
- [64] S. Pisana, M. Lazzeri, C. Casiraghi, K. S. Novoselov, A. K. Geim, A. C. Ferrari, and F. Mauri, “Breakdown of the adiabatic Born–Oppenheimer approximation in graphene” nat. mater., 6, 198 (2007).
- [65] V. N. Popov, “Dynamic and charge doping effects on the phonon dispersion of graphene”, Phys. Rev. b 82, 045406 (2010).
- [66] T. M. G. Mohiuddin, A. Lombardo, R. R. Nair, A. Bonetti, G. Savini, R. Jalil, N. Bonini, D. M. Basko, C. Galiotis, N. Marzari, K. S. Novoselov, A. K. Geim, and A. C. Ferrari, “Uniaxial strain in graphene by Raman spectroscopy: Peak splitting, Grüneisen parameters and sample orientation” Phys Rev. b 79, 205433(2009).
- [67] D. S. Lee, C. Riedl, B. Krauss, K. V. Klitzing, U. Starke, and J. H. Smet, “Raman Spectra of Epitaxial Graphene on SiC and of Epitaxial Graphene Transferred to SiO₂” Nano Lett 8, 4320 (2008).

Chapter 7

Growth of Non-Concentric Graphene Ring on 6H-SiC (0001) Surface

Optical antennas are devices that efficiently convert the energy of free propagating radiation into localized energy and vice versa. The development of optical antennas is promising for improving the efficiency of sensing, photodetection, photovoltaic technique, light emission, spectroscopy and so on [68]. Graphene is a two dimensional carbon material where its carbon atoms are packed in a honeycomb crystal lattice. Graphene plasmons have much tighter confinement and relatively long propagation distances that are advantage for tunable devices [69]. The electric field enhancement factor of graphene plasmon for tunable terahertz optical antennas was demonstrated using analytical model by Liu *et al.* [70] which has shown that the electric field enhancement factor from graphene ring is about 20 times larger than gold nanoring. They also found that graphene ring with eccentricity can increase efficiency of optical antennas. Traditionally, graphene ring can be fabricated by cutting down a larger graphene which can be prepared in many ways such as mechanical exfoliation of graphite, chemical vapor deposition (CVD) of carbon-bearing gases on the surface of copper films [71,72] and thermal decomposition of SiC substrates.

In this chapter, the growth of non-concentric epitaxial graphene rings on Si-terminated SiC (0001) is studied. This method can keep the ring edge intact. Moreover, the edge structure of the ring is armchair edge because it is the stable edge structure of graphene islands on SiC [73]. The contents in this chapter were published in [74].

7.1 Experimental

Epitaxial graphene was produced by employing N-type Si-terminated 6H-SiC (0001) substrates. The procedure for graphitizing SiC was performed by resistive heating under UHV and inert gas (He, Ne or Ar) pressure of 0.05-0.3 atm. The annealing temperature was in range of ~900°C to graphitization temperature (~1300 °C, ~1600 °C and 1675 °C under UHV, inert gas pressure of 0.05-0.1 atm and Ar pressure of 0.3 atm, respectively) with steps of ~100°C (10~15 minutes per each step).

After annealing, reflection high-energy electron diffraction (RHEED) with incident beam energy of 10 kV was employed to measure the structure of SiC surface in the main chamber (base pressure of ~ 10^{-8} Pa). The morphology of samples was measured by atomic force microscopy (AFM) and scanning tunneling microscopy (STM) in air and UHV, respectively. Ultra-high vacuum scanning electron microscopy (UHV-SEM) with an incident beam of 2.2 keV was also performed.

7.2 Condition for the growth of graphene rings on Si-face SiC (0001)

RHEED results show the surface structure of 6×6 reconstruction after annealing at the graphitization temperature (~1600 °C). The reflections from graphene are appeared around (0.72, 0.72) and ($\overline{0.72}, \overline{0.72}$) spots [75] when the incident beam was applied in the [$\overline{1}010$] direction. In addition, when the sample was rotated by 30 degree ([$\overline{1}\overline{1}20$] incidence), the reflections from graphene are observed near (0, ±2) spots, suggesting that the graphene unit cell is rotated by 30 degree from the SiC unit cell.

I find the non-concentric graphene rings with the diameter of ~500 nm can be grown on the samples after annealing under various conditions as shown in Table 7.1. Figure 7.1 shows AFM topographic (a, b, c, e, g and i) and phase (d, f, h and j) images of the samples annealed in UHV (a and b), He pressure of 0.05 atm (c and d), Ne pressure of 0.05 atm (e and f), Ar pressure of 0.05 atm (g and h) and Ar pressure of 0.3 atm (i and j). In the case UHV (Figure 7.1 (a) and (b)), narrow terraces (~hundreds nanometer) are obtained. Graphene islands are

indiscernible on this sample. For annealing in He gas, bright and dark brown regions in AFM phase images (Figure 7.1 (d)) indicate graphene and non-graphene areas, respectively. The terraces which obtained on this sample surface are obviously wider than those annealed in UHV. It is attributed to higher graphitization temperature and suppression of Si sublimation. The significantly high growth temperature enhances the surface diffusion. Therefore the sample surface can be completely restructured before graphene is formed [76]. On this sample surface, triangular graphene islands appear on wide terraces as indicated by red circles. For Ne (Figure 7.1 (e) and (f)), bright yellow, dark brown and black regions in AFM phase images (Figure 7.1 (f)) indicate graphene bilayer, monolayer and buffer layer, respectively. On wide terraces of this sample the triangular graphene islands with and without non-graphene area inside are observed as shown in inset (e) and (f). Figure 7.1 (g) and (h) show the initial stage of graphene formation measured after a SiC substrate was annealed under Ar pressure of 0.05 atm. The formation of monolayer graphene rings and triangular graphene islands can be observed. Note that the graphene rings on SiC (0001) do not have perfect circles at their edge. The shape of their edges looks like a hexagon. In the case of annealing under Ar pressure of 0.3 atm (Figure 7.1 (i) and (j)), graphene island is absent on the terrace even if the terrace width is as large as the sample annealed under the gas pressure of 0.05 atm.

Table 7.1. Density and diameter of graphene rings on SiC which annealed under various gases and pressure.

Pressure (atm)	UHV	0.05		0.1	0.3
Gas Type		He	Ne	Ar	Ar
Graphitization Temperature (°C)	1300	~1600			1675
Ring Density (μm^{-2})	0	0.17	0.14	0.24	0.056
Ring Diameter (nm)	0	500	500	500	0

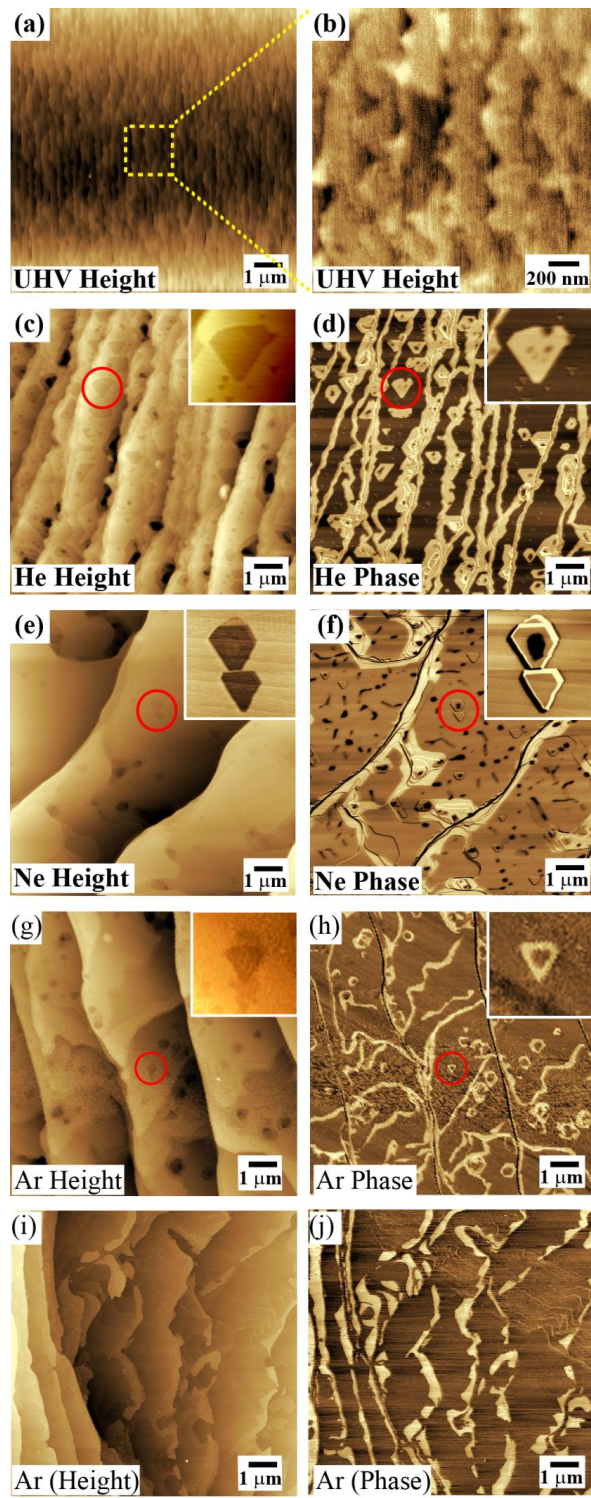


Figure 7.1. AFM topographic (a, b, c, e, g and i) and phase (d, f, h and j) images of the samples annealed in UHV (a and b), He pressure of 0.05 atm (c and d), Ne pressure of 0.05 atm (e and f), Ar pressure of 0.05 (g and h) and Ar pressure of 0.3 atm (i and j). (b) Magnified image of a dash square in (a). Insets in (e, f) and (g, h) are magnified images around cirlcle area in (e, f) and (i, j), respectively.

7.3 Edge structure of graphene ring

The presence of graphene on triangular islands was also confirmed by STM measurement. Figure 7.2 (a) shows the morphology of a triangular graphene island with a deep pit at its center measured on the sample annealed under Ar gas pressure of 0.05 atm by STM. The area in a square dash frame is magnified and shown in Figure 7.2 (b) reveals moiré pattern which originated from a mismatch between graphene structure and the SiC substrate. A rhombohedron indicates 6×6 reconstruction on this surface. The superlattice periodic is ~ 1.8 nm suggests graphene lattice constant is ~ 2.4 Å. Figure 7.2 (c) shows the schematic of (a) revealing the regions of monolayer graphene (yellow) and buffer layer (green). Figure 7.2 (d) shows a schematic of moiré pattern which contains 6×6 reconstruction (indicated by a red rhombohedron) in the same direction as Figure 7.2 (b). A blue triangle is an imitation of a triangular graphene island which is arranged in the same direction as the triangular graphene island in Figure 7.2 (a) demonstrating that the edge structure of the triangular graphene island is armchair edge.

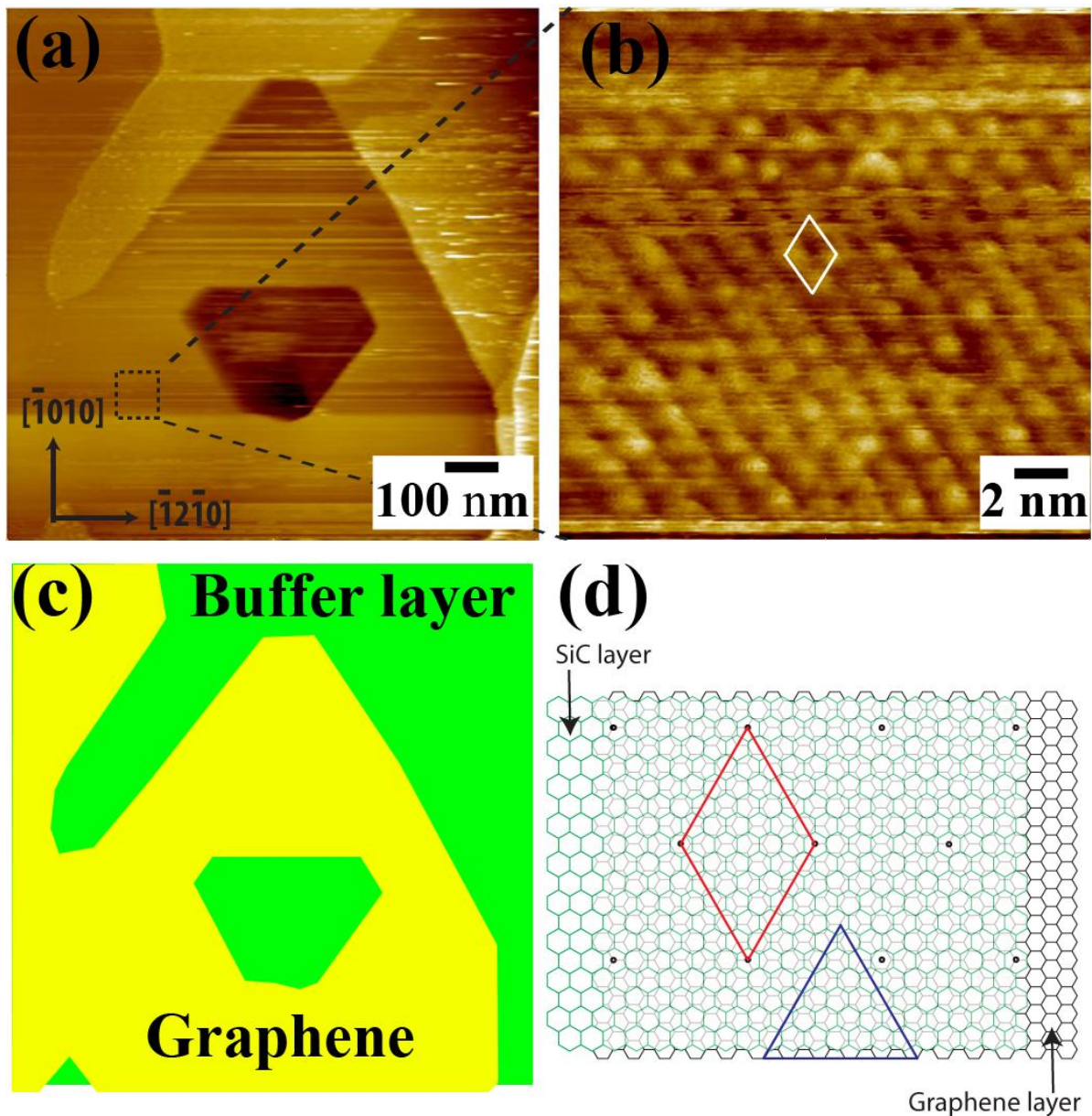


Figure 7.2. (a) STM images ($V = -1$ V and $I = 0.05$ nA) shows morphology of graphene islands which contains a hexagon pit at its center. (b) Magnified STM image ($V = -0.5$ mV and $I = 0.05$ nA) of the dash square frame in (a) showing moiré pattern which originated from mismatch between graphene and the substrate. A rhombohedron indicates 6×6 structure. (c) Schematic of (a) reveals the monolayer graphene (yellow) and buffer layer (green) regions. (d) Schematic of graphene structure lying on SiC structure reveals moiré pattern. A rhombohedron indicates the 6×6 structure with same direction as (b). The triangle is a imitation of triangular graphene of (a), suggesting the triangular island has armchair edge.

7.4 Growth of graphene rings

UHV-SEM is one of the methods which can identify the thickness of graphene layers by SEM contrast. For this measurement, the accelerating voltage is set to 2.2 eV. At this accelerating voltage, SEM contrast of thinner graphene is brighter than that of thicker graphene [77]. We choose the sample which was annealed under Ar pressure of 0.05 atm to study the evolution of graphene rings by UHV-SEM technique. The graphene thickness distribution was also confirmed by X-ray diffraction (XRD) and angle-resolved photoemission spectroscopy (ARPES) [78]. Figure 7.3 (a) shows a schematic of resistive heating method for annealing SiC substrates. This heating method gives us a non-uniform temperature on the sample, leading to an appearance of graphene thickness distribution on the surface. This effect gives us an opportunity to find evidences for the progress of graphene ring growth from the initial state. Figure 7.3 (b) shows SEM image measured at the boundary between graphene (dark region) and SiC (bright region). At the boundary region (Figure 7.3 (c)), The SEM image gave 3 different contrasts, i.e., bright, dark gray and black indicating SiC, buffer and graphene regions, respectively. The buffer layer and striped graphene monolayer are first formed at step edges. Graphene rings also start forming at this state as indicated by a vertical arrow. Surprisingly, we have never found buffer layer ring (without graphene layer) on the substrate although the first carbon layer which is formed on the SiC substrate is buffer layer. It implied that the formation speeds of graphene and buffer layer on the ring are nearly same. At the higher annealing temperature area Figure 7.3 (d), the whole surface is covered by at least 1 carbon layer (buffer layer). We find that the shape of graphene rings evolves to triangle-like and points to the same direction on the same terrace. At the highest annealing temperature area on this sample (Figure 7.3 (e)), a buffer layer area is often found inside the graphene island although the size of triangular graphene islands becomes larger and merges the other graphene regions as shown clearly in Figure 7.3 (f).

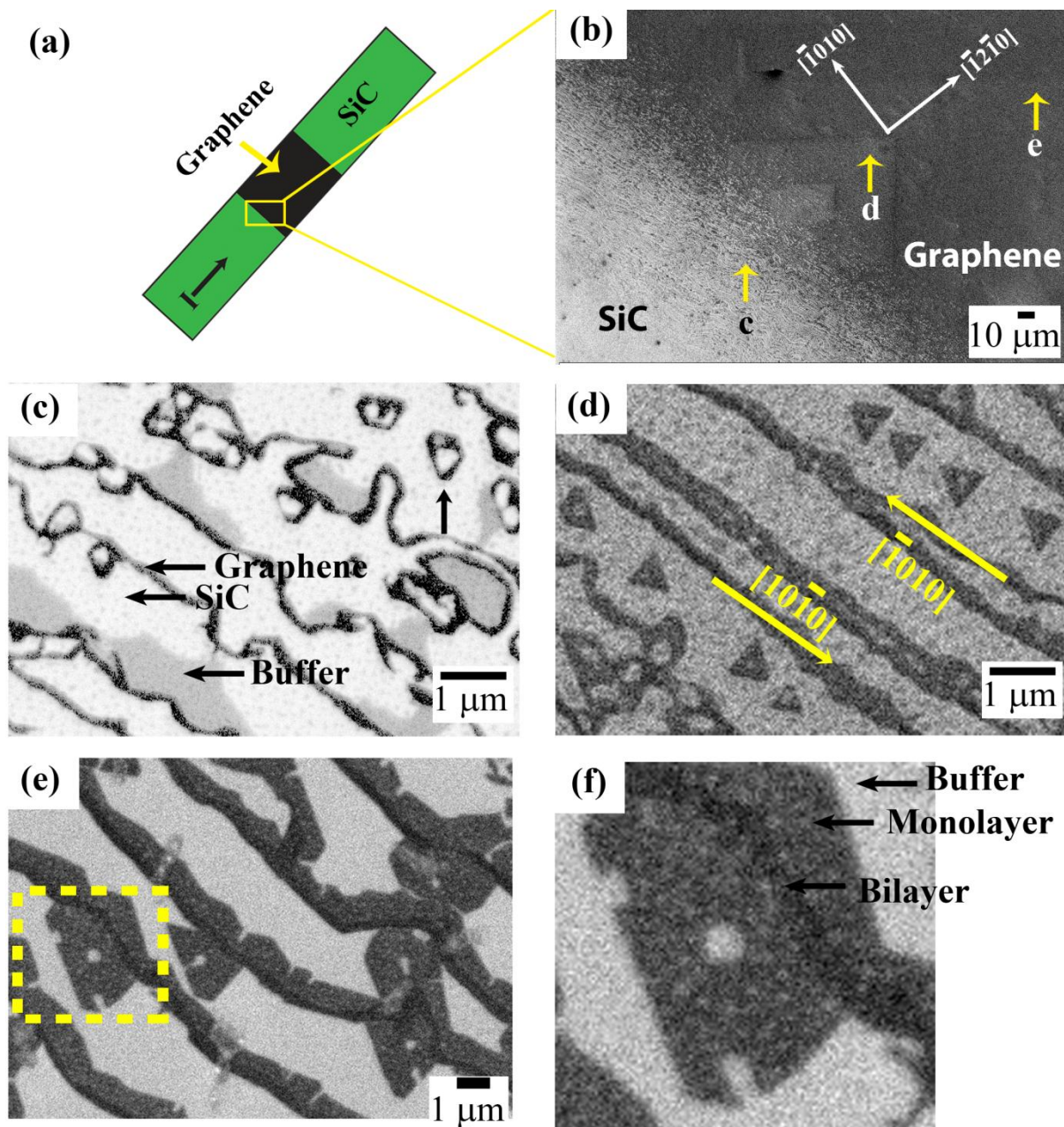


Figure 7.3. SEM image (acceleration voltage of 2.2 kV) of SiC (0001) annealed under argon gas pressure of 0.05 atm. (a) Schematic showing annealing method by resistive heating. (b) Wide view SEM image measured at the boundary between graphene and SiC shows positions which are measured and displayed in (c)-(e). A vertical arrow in (c) indicates an example of graphene ring formed. (f) Manifid image at the square dash rectangle in (e).

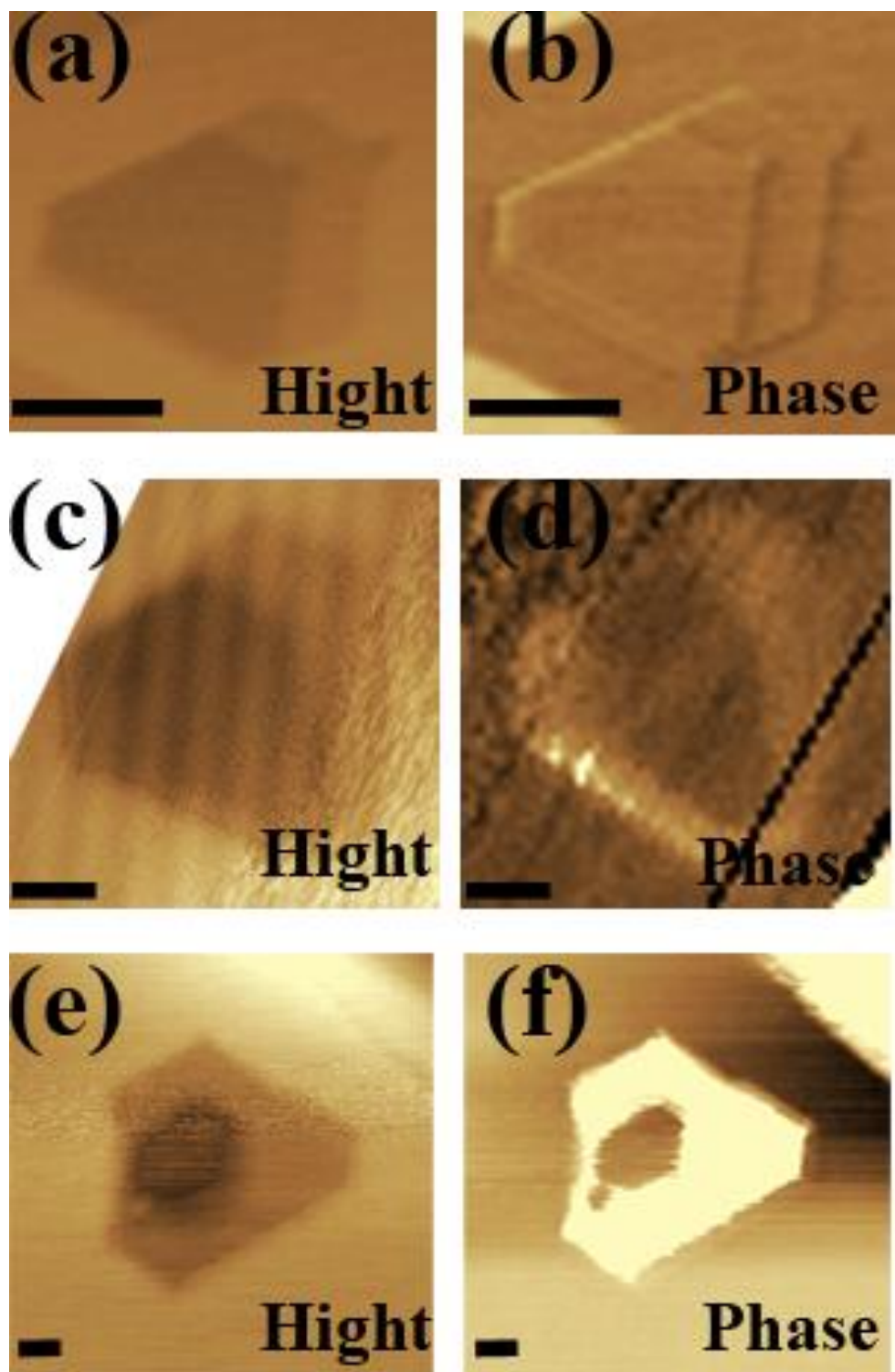


Figure 7.4. AFM topographic (a, c and e) and phase (b, d and f) images showing the growth evolution of triangular graphene islands on SiC (0001) substrate. Scale bars indicate 100 nm. Bright and dark regions in phase images represent graphene and SiC regions, respectively.

Figure 7.4 shows a sequence of graphene ring growth observed by AFM. Figure 7.4 (a) and (b) are topographic and phase images, respectively, measured at the same time and position on the SiC (0001) surface annealed under Ar gas pressure of 0.05 atm, showing a small deep SiC hexagon pit inside a larger shallow one with non-concentricity before graphene ring growth. No difference in phase contrast confirms the material inside and outside the pit are same (both are SiC). Figure 7.4 (c) and (d) display a next step of graphene ring evolution. The difference in phase (bright region) in Figure 7.4 (d) indicates graphene first layer which is grown around a deep pit on a larger shallow one. After that, the graphene ring becomes a bigger triangular graphene island as shown in Figure 7.4 (e) and (f).

7.5 Discussion

7.5.1 Growth of graphene stripe at step edge

We find that the step bunching appears on the surface after the substrate was annealed at near graphitization temperature. When the annealing temperature reaches a graphitization temperature, the buffer layer and graphene monolayer first nucleate at step edge and propagates into their upper terrace with almost identical speed. It is attributed to same rate of Si sublimation. In the case of the growth of buffer layer, Si sublimation rate is fast because Si can be easily sublimated from the bare SiC surface directly. For the growth of graphene monolayer, the SiC layers under the buffer layer are still decomposed with high speed because there are two easy ways for releasing the free silicon atoms; (1) releasing through the above buffer layer to the surface or (2) interstice layer underneath the buffer layer to step edge (Figure 7.5 (a)). This supposition is corresponding with the earlier study which has shown the calculation of the barrier energy for Si penetration through buffer layer structure is ~ 4.7 eV and that for Si interstice is ~ 3.5 eV [79]. The both energy barriers are obviously lower than the case of Si diffusion through a graphene layer (>13 eV). Note that graphene monolayer originated from the topmost buffer layer, i.e., after a new buffer layer was grown, the old buffer layer becomes a new first

graphene layer as indicated by black line in Figure 7.5 (b). The free carbon atoms which are released by erosion of the step edge coalesce to the new buffer layer with same speed as the initial state. Eventually, the extended buffer layer covers SiC surface as shown in Figure 7.5 (b). At this state, the decomposition of SiC under buffer layer is far from step edge leading to the Si atoms under the buffer layer have only one easy way to desorb from the surface, i.e. releasing through buffer layer structure results in reduction of graphene formation speed. Therefore, SiC surface is covered by buffer layer faster than graphene monolayer.

7.5.2 Growth process of graphene rings

We find that graphene rings evolve from SiC hexagon pits which originate from a point defect which caused by vacancy of carbon atom [80]. A carbon atom, which has the lowest energy to form vacancy on a SiC surface, is first dissociated and leaves behind a vacancy as labeled by number 1 in Figure 7.6. This vacancy lowers the number of bonds surrounding Si atoms and leads to their dissociation (labeled by number 2). The surrounding C atoms (number 3) and the next outer Si atoms (number 4) are repeatedly dissociated in the same process, consecutively. Finally a hexagon SiC pit with zigzag edge appears on the terrace. A new pit also nucleates inside the old one by repeating the same process.

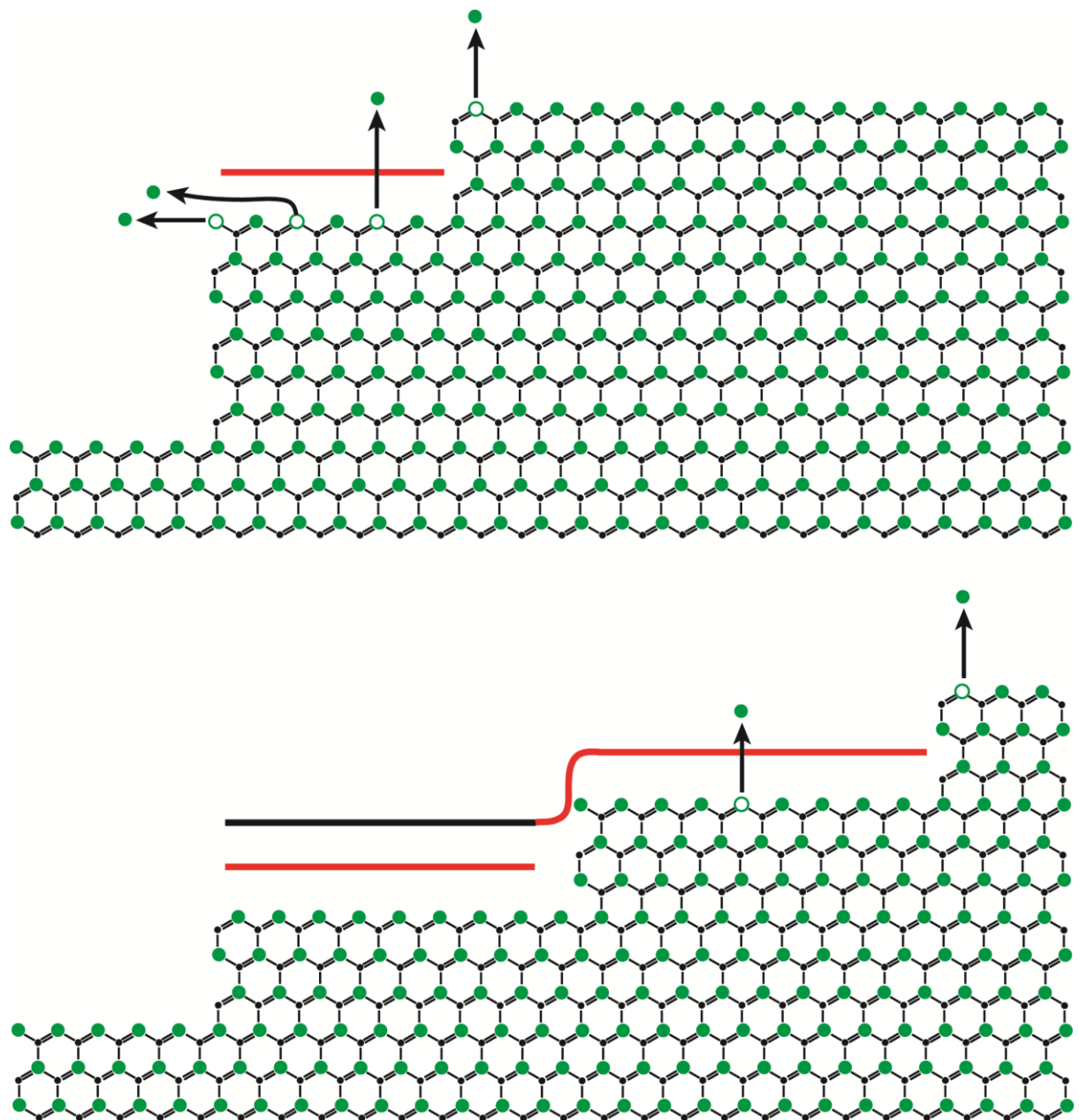


Figure 7.5. Schematic of graphene growth at the step edge showing the formation of (a) buffer and (b) first graphene layers. Small and big circles represent carbon and silicon atoms, respectively. Red and black lines represent buffer and graphene layer, respectively.

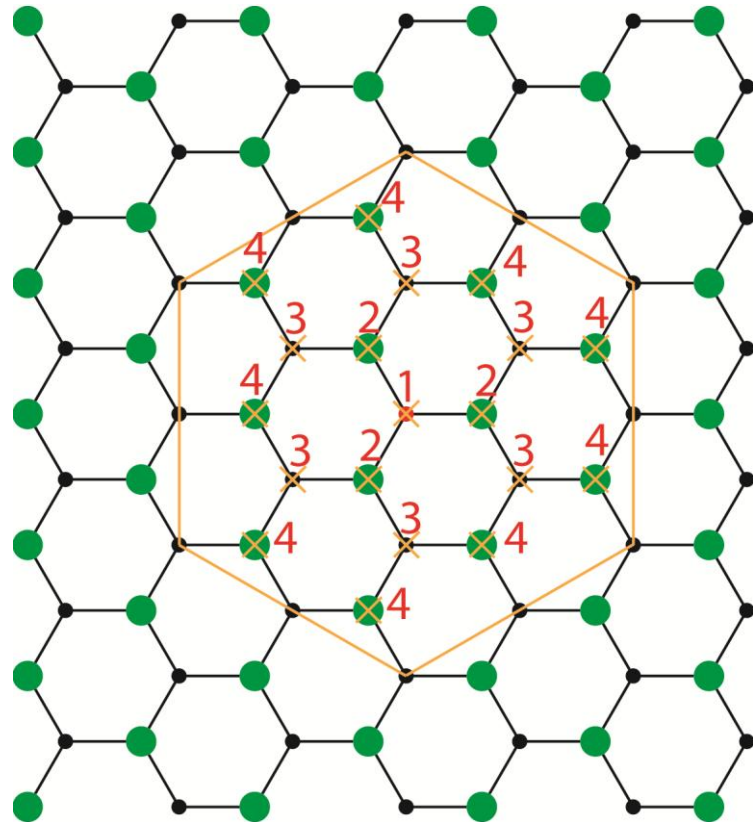


Figure 7.6. Schematic of SiC (0001) surface shows the origin of a SiC hexagon pit with zigzag-edge. Small and big circles represent carbon and silicon atoms, respectively. The number near the atoms indicates dissociation order.

The results from the AFM (Figure 7.1) show graphene rings can be formed on the substrates which are annealed under inert gas pressure around 0.05 atm. In addition, the type of inert gas has no effect on the formation of graphene ring as shown in Figure 7.1 (c) - (h). The key factors of graphene ring growth may be graphitization temperature and Si sublimation rate. In the case of annealing a SiC substrate under inert gas, the graphitization temperature shifts higher, leading to higher possibility of pit formation. Nevertheless graphene rings cannot be grown by annealing a SiC substrate under higher pressure of inert gas although the graphitization temperature increases as shown in Figure 7.1 (i) - (j). It is attributed to compensation of atoms (vacancies once formed are buried easily) on the surface, i.e., annealing under high pressure of inert gas results in increase of graphitization temperature as well as decrease of Si sublimation rate. Although there are many vacancies on the surface during

annealing at high temperature, those vacancies are filled up by atoms diffusing around them.

Schematic in Figure 7.7 shows the sequence of the growth of graphene ring. Two pits with eccentricity are first nucleated on the SiC terrace by carbon vacancy (Figure 7.7 (a)). When the edges of the two pits are eroded and merged each other there is a strong attractive interaction between SiC steps to be united into one group. For a better understanding of erosion speed on the two SiC pits, Figure 7.8 shows a schematic of the erosion speed and direction of the two concentric 6H-SiC pits. The depth of each pit is three SiC bilayers. Since SiC has three-fold symmetry and the erosion speed depends on the stacking structure, therefore three symmetrical directions at the pit step have the same erosion speed. In addition, the stacking sequences of upper and lower half of 6H-SiC are opposite leading to the erosion speed, in the same direction, between shallow and deep pits is different. Eventually, the edges of the two pits will merge each other. After the merging, both edges are, therefore, eroded together even if the upper step has higher erosion speed than the lower one [82]. The speed of erosion of pit step depends on the step height, i.e., a higher step needs higher energy to break Si-C bonding more than a lower one, leading to the erosion speed of the higher step being slower than that of lower one. Therefore, the edge step of the larger pit without edge mergence is eroded fastest (as indicated by vectors in Figure 7.7 (a)), and free carbon atoms from step erosion form graphene layer between large and small pit area. The evidence from SEM measurement (Figure 7.3 (b) and (c)) shows buffer and first graphene layers are formed at around same time. The growth mechanism is same as the case of graphene stripe growth at step edge. Graphene formation in the direction of 2 askew vectors in Figure 7.7 (b) continues until the graphene surrounds the small pit as shown in Figure 7.7 (c). The formation of graphene ring at this stage destroys the strong interaction of merging edge, resulting in independence of the erosion of two pit edge (separation of the step edges). The erosion speed depends on the direction of the step; since 6H-SiC has 3-fold symmetry, 3 equivalent direction have the same erosion speed but the other three have different one. This causes final shape of graphene islands to be triangle-like (Figure 7.7 (d)).

The epitaxial graphene rings are fabricated by annealing SiC under inert gas pressure of 0.05 atm. The width of graphene rings can be controlled by annealing temperature and time. Most of graphene rings which are grown by this method give us off-center rings that are suitable for application to tunable

terahertz optical antennas because the calculation using the model from Liu et al shows the electric field enhancement factor of graphene ring increases with eccentricity of the ring. Moreover, this electric field enhancement factor is about 20 times larger than that of gold nanoring with the same size [70]. However, in the model the diameter of graphene ring was chosen to be 100 nm. The diameter in their calculation is different from our results which give us the minimum graphene ring diameter of ~500 nm, implying that the electric field enhancement factor from our graphene rings may be larger than that from the model. The largest rings (shape is triangle-like) is approximately 2 μ m.

7.6 Conclusion

We found the growth of non-concentric graphene rings with armchair edge on SiC (0001) by annealing under inert gas pressure. The formation of graphene ring depends on the pressure of ambient gas but slightly depends on the type of gas. The highest density of non-concentric graphene rings occurs after annealed under condition of Ar pressure of 0.05 atm. The minimum diameter of graphene rings is about 500 nm.

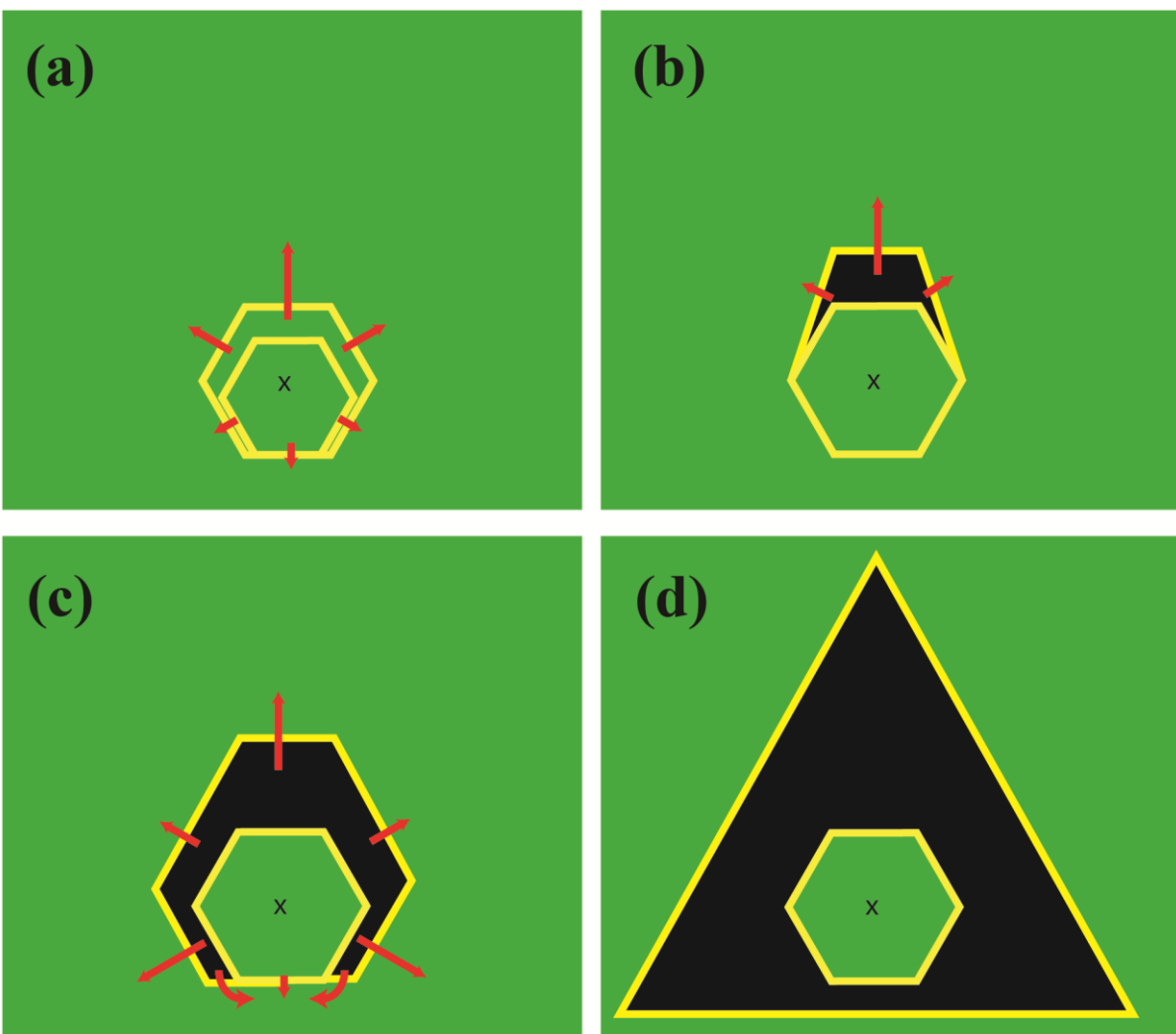


Figure 7.7. Schematic showing a sequence of the growth of epitaxial graphene ring. Green and black regions represent SiC and graphene, respectively. Red vectors indicate step erosion direction and speed. Symbol “X” indicates an origin point to guide the eye.

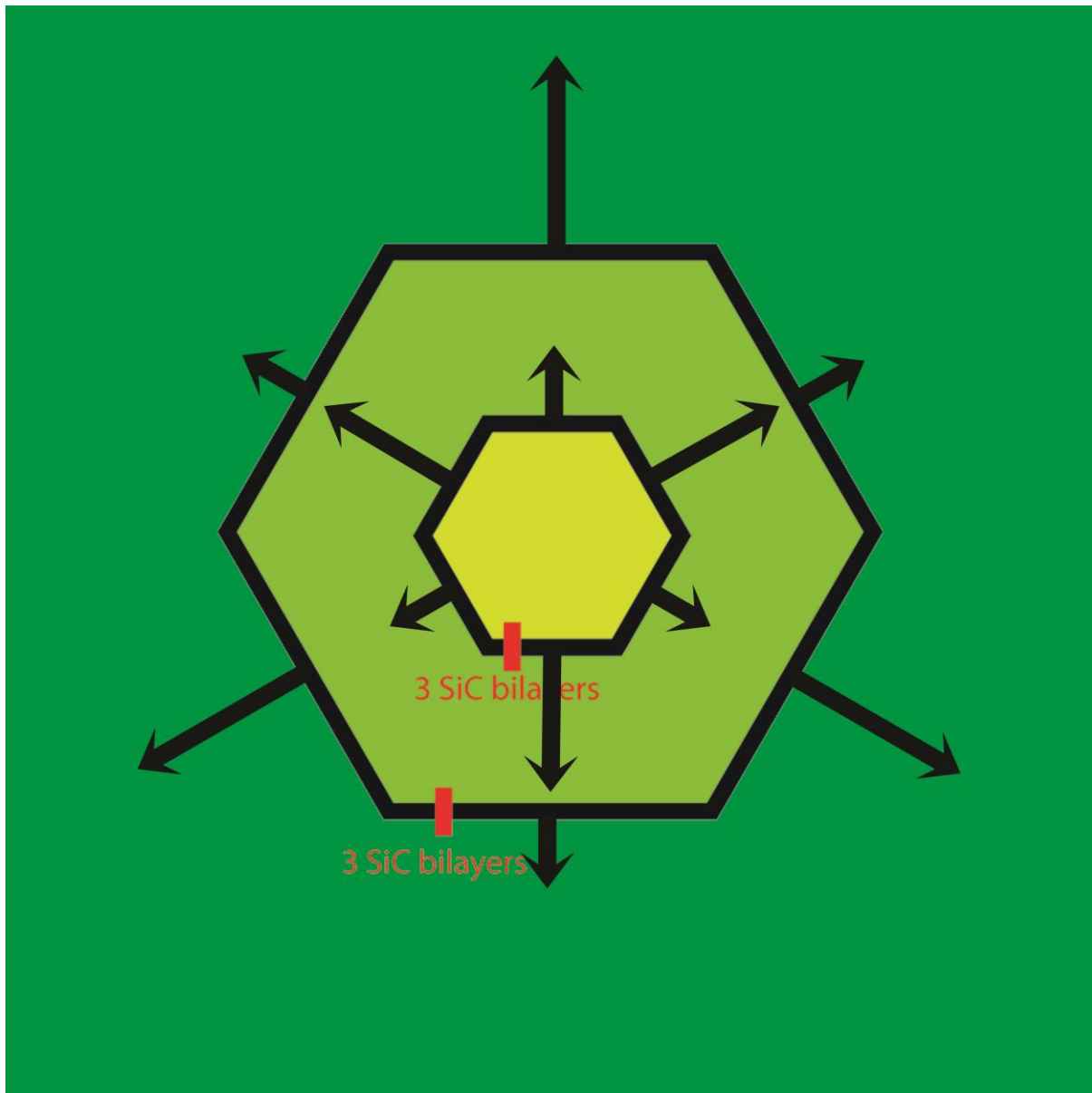


Figure 7.8. Schematic of erosion speed on two SiC pits.

References for chapter 7

- [68] L. Novotny, N. V. Hulst, antennas for light, Nat. Photonics 5, 83 (2011).
- [69] F. H. L. Koppens, D. E. Chang, F. J. G. de Abajo, Graphene Plasmonics: A Platform for Strong Light-Matter Interactions, Nano Lett. 11, 3370 (2011).

- [70] P. Liu, W. Cai, L. Wang, X. Zhang, J. Xu, Tunable terahertz optical antennas based on graphene ring structures, *Appl. Phys. Lett.* 100, 153111 (2012).
- [71] A. Ismach, C. Druzgalski, S. Penwell, A. Schwartzberg, M. Zheng, A. Javey, J. Bokor, Y. Zhang, Direct chemical vapor deposition of graphene on dielectric surfaces, *Nano Lett.* 10, 1542 (2010).
- [72] J. Tian, H. Cao, W. Wu, Q. Yu, Y. P. Chen, Direct imaging of graphene edges: atomic structure and electronic scattering, *Nano Lett.* 11, 3663 (2011).
- [73] G. M. Rutter, N. P. Guisinger, J. N. Crain, P. N. First, J. A. Stroscio, Edge structure of epitaxial graphene islands, *Phys. Rev. B* 81, 245408 (2010).
- [74] A. Ruammatree, H. Nakahara, Y. Saito, Growth of non-concentric graphene ring on 6H-SiC (0001) surface, *Appl. Surf. Sci.* 307, 136 (2014).
- [75] A. Charrier et al, Solid-state decomposition of silicon carbide for growing ultra-thin heteroepitaxial graphite films, *J. Appl. Phys.* 92, 2479 (2002).
- [76] K. V. Emtsev et al., Towards wafer-size graphene layers by atmospheric pressure graphitization of silicon carbide, *Nature Mat.* 8, 203 (2009).
- [77] H Hiura, H Miyazaki, K. Tsukagoshi, Determination of the number of graphene layers: discrete distribution of the secondary electron intensity stemming from individual graphene layers, *Appl. Phys. Express* 3, 095101 (2010).
- [78] A. Ruammatree, H. Nakahara, K. Akimoto, K. Soda, Y. Saito, Determination of non-uniform graphene thickness on SiC (0 0 0 1) by X-ray diffraction. *Appl. Surf. Sci.* 282, 297 (2013).
- [79] G. F. Sun, Y. Liu, S. H. Rhim, J. F. Jia, Q. K. Xue, M. Weinert, and L. Li. Si diffusion path for pit-free graphene growth on SiC(0001), *Phys. Rev. B* 84, 195455 (2011).
- [80] M. L. Bolen, S. E. Harrison, L. B. Biedermann, M. A. Capano, Graphene formation mechanisms on 4H-SiC(0001), *Phys. Rev. b* 80, 115433 (2009).
- [81] T. Kimoto, A. Itoh, H. Matsunami, T. Okan, Step bunching mechanism in chemical vapor deposition of 6H- and 4H-SiC{0001}, *J. Appl. Phys.* 81, 3494 (1997).

[82] W. Wulfhekela et al, Regular step formation on concave-shaped surfaces on 6H–SiC(0 0 01) ,Surf. Sci. 550, 8 (2004).

Chapter 8

Summary of This Thesis

In this thesis, I have demonstrated the growth and characterization of graphene on Si and C terminated SiC. Moreover, I have demonstrated a new method for estimating graphene thickness on 6H-SiC (0001) (In chapter 4). This method gives us the absolute and reliable information about graphene thickness distribution on SiC substrate by using XRD experimental results and simple Laue function. This new method was confirmed by other measurements such as angle-resolved photoemission spectroscopy, ultra-high vacuum scanning electron microscope and Raman spectroscopy.

In case of the growth of graphene on C-terminated SiC (chapter 5), an Ar-mediated rapid heating method was carried out to grow a high quality few-layer graphene on the C-face 6H-SiC (000 $\bar{1}$) substrate. After annealing, the few-layer graphene was obtained. The few-layer graphene can continuously extend across the steps (3–9 nm in height) to form large-scaled grains. Raman spectra show that the peak positions remain unconverted at 1585 cm^{-1} (G band) and 2700 cm^{-1} (2D band). The intensity ratio between 2D peak and G peak ($I_{2\text{D}}/I_{\text{G}}$) is predominant in the range of about 1.4–2.5.

For the growth of graphene on Si-terminated SiC, I have demonstrated the growth of various shapes of graphene on SiC (0001) such as embedded and protrusive graphene strips, graphene rings and graphene triangles. I found that the shapes of the graphene depend on inert gas pressure and annealing temperature. In chapter 6, the growth of epitaxial embedded and protrusive striped graphene on Si-terminated 6H-SiC (0001) was demonstrated by annealing the SiC substrates under argon pressure of 0.05 and 0.3 atm, respectively. I found that the graphitization temperature rises from $1550\text{ }^{\circ}\text{C}$ to $1675\text{ }^{\circ}\text{C}$ with increment of Ar pressure from 0.05 atm to 0.3 atm. The reflection high energy electron diffraction results reveal that graphene unit cell for both cases, embedded and protrusive graphene, is rotated by 30 degree from SiC unit

cell. In addition, graphene prefers to be grown at upper-side step edge. In the case of the sample annealed under argon pressure of 0.3 atm, a nucleation of protrusive graphene layer occurs at the upper-side step edge. It is attributed to diffusion of free C and Si atoms which are released from the SiC decomposition and migrate to the step edge and form graphene there. In addition, Raman peak characteristics and ARPES spectra revealed that the embedded and protrusive graphene on the sample annealed under Ar pressure of 0.05 atm and 0.3 atm, respectively, have approximately the same carrier concentration and graphene film strain.

In chapter 7, the growth of non-concentric graphene rings with an armchair edge was demonstrated by annealing SiC substrates under inert gas pressure. The experimental results reveal that pressure of ambient gas is an important factor for the growth of graphene rings. In this chapter I also express that the type of gas is slightly effect on the formation of graphene rings. In addition, I found that the highest density of non-concentric graphene rings occurs after annealing under the condition of Ar pressure of 0.05 atm. The minimum diameter of graphene rings is about 500 nm.

Acknowledgments

The present research was performed in Professor Saito's laboratory, Department of Quantum Engineering, Graduate School of Engineering, Nagoya University. The author would like to thank his research advisors, Professor Yahachi Saito, Assistant Professor Hitoshi Nakahara and Lecturer Professor Koji Asaka, Department of Quantum Engineering, Graduate School of Engineering, Nagoya University, for guidance and valuable suggestion in preparing this thesis.

He would like to acknowledge Professor Koichi Akimoto, Division of Mathematical and Physical Sciences, Graduate School of Science, Japan women's University for guidance and valuable suggestion in synchrotron X-ray diffraction technique. He also thanks Professor Kazuo SODA, Department of Quantum Engineering, Graduate School of Engineering, Nagoya University for useful advices in angle-resolved photoemission spectroscopy technique.

Synchrotron X-ray diffraction measurements were supported by Photon Faculty, High Energy Accelerator Research Organization, Tsukuba, Ibaraki Prefecture, Japan. The ARPES measurements were performed at the Institute of Molecular Science, Okazaki, Aichi Prefecture, Japan. Raman spectroscopy, ultra high vacuum scanning electron microscope, scanning tunneling microscope were carried out at Venture Business Laboratory, Nagoya University. The author thanks heartily administrator of above organization for their supports in experiments in this thesis.

The author acknowledges Mr. Hailong Hu, Mr. Chenxing Wang, Mr. Shinichi Ito, Mr. Yohei Hasebe, Mr. Shunya Oishi, Mr. Yuji Shinomiya, Mr. Yutaro Suzuki, Mr. Masahiro Matsuda, Mr. Keita Yamaguchi, Mr. Tomonori Kato, Mr. Yuto Kawai, Mr. Sotaro Fujita, Mr. Noboru Yokoyama and all other members who have studied in Professor Saito's laboratory.

Finally, the author would like to thanks, parents, brothers, all his teachers and good friends for encouragement throughout his doctoral course.

List of Papers

1. Original Paper

Title	Journal	Authors
Determination of non-uniform graphene thickness on SiC (0001) by X-ray diffraction	Applied Surface Science 282, 297-301 (2013).	<u>A. Ruammitree</u> , H. Nakahara, K. Akimoto, K. Soda, Y. Saito
Few-layer epitaxial graphene with large domains on C-terminated 6H-SiC	Surf. Interface Anal. 44, 793–796 (2012).	H. Hu, <u>A. Ruammitree</u> , H. Nakahara, K. Asaka Y. Saito
Growth of Embedded and Protrusive Striped Graphene on 6H-SiC (0001)	International Journal of Engineering and Innovative Technology Vol. 3, Issue 7, 34-38 (2014).	<u>A. Ruammitree</u> , H. Nakahara, K. Soda, Y. Saito
Growth of non-concentric graphene ring on 6H-SiC (0001) surface	Applied Surface Science 307, 136-141 (2014).	<u>A. Ruammitree</u> , H. Nakahara, Y. Saito

2. Conferences

Title	Conference	Authors
Effect of adsorption of benzene on field electron emission from a carbon nanotube	The 38 th Fullerene-Nanotubes General Symposium (2010, Nagoya Japan)	<u>A. Ruammitree</u> , H. Hu, H. Nakahara and Y. Saito
Growth of epitaxial graphene on SiC (0001) and (000-1) by heat treatment in Ar atmosphere	2010 the 71 st The Japan Society of Applied Physics (2010, 応用物理学会、長崎大学 文教キャンパス)	H. Hu, <u>A. Ruammitree</u> , H. Nakahara and Y. Saito
X-ray Diffraction Study on Epitaxial Graphene Grown on SiC(0001)	2011 the 58 st The Japan Society of Applied Physics (2011, 応用物理学会、神奈川工科大学)	<u>A. Ruammitree</u> , H. Hu, H. Nakahara, K. Akimoto, S. Harada, K. Soda, Y. Saito
Epitaxial growth of large-scale few-layer graphene on SiC (000-1) by heat treatment in Ar atmosphere	2011 the 58 th The Japan Society of Applied Physics (2011, 応用物理学会、神奈川工科大学)	H. Hu, <u>A. Ruammitree</u> , H. Nakahara, K. Asaka, Y. Saito
Determination of Epitaxial Graphene Thickness by X-ray Diffraction and Raman Spectroscopy	8 th International Symposium on Atomic Level Characterizations for New Materials and Devices`11 (ALC`11, 2011, Seoul Korea) 8 th International	<u>A. Ruammitree</u> , H. Hu, H. Nakahara, K. Akimoto, S. Harada, K. Soda, Y. Saito

Growth of Large-scale Domains of Epitaxial Graphene on C-face SiC	Symposium on Atomic Level Characterizations for New Materials and Devices`11 (ALC`11, 2011, Seoul Korea)	H. Hu, <u>A. Ruammitree</u> , H. Nakahara, K. Asaka and Y. Saito
Initial Growth Stage of Epitaxial Graphene on Si-terminated SiC (0001) in Ar	2011 the 72 th The Japan Society of Applied Physics (2011 年, 第 72 回応用物理学会、山形大学 小白川キャンパス)	<u>A. Ruammitree</u> , H. Hu, H. Nakahara, K. Akimoto, K. Soda and Y. Saito
Preferential growth of Ar-mediated epitaxial graphene on 6H-SiC	The 41 st Fullerenes-Nanotubes-Graphene General Symposium (2011 Tokyo Metropolitan University, Minami-Osawa Campus)	H. Hu , <u>A. Ruammitree</u> , D. Maeta, H. Nakahara, K. Asaka, Y. Saito
Effect of inert gas on the growth of epitaxial graphene on Si-terminated SiC (0001)	The 44 th Fullerenes-Nanotubes-Graphene General Symposium (2013 University of Tokyo, Hongo Campus)	<u>A. Ruammitree</u> , H. Nakahara, Y. Saito
Growth of triangular and striped graphene islands on SiC (0001) by thermal decomposition in inert gas atmosphere	9th International Symposium on Atomic Level Characterizations for New Materials and Devices '13 (2013 Sheraton Kona, The Big Island, Hawaii, USA).	<u>A. Ruammitree</u> , H. Nakahara, Y. Saito

Growth of embedded and protrusive graphene rings on 6H-SiC (0001) by thermal decomposition in argon gas atmosphere	The 4th edition of Graphene Conference (6-9 May 2014 at Centre de Congres Pierre Baudis, Toulouse, France).	<u>A. Ruammitree</u> , H. Nakahara, Y. Saito
--	---	--

3. Awards

Award Name	Place and Time
Student Award	9th International Symposium on Atomic Level Characterizations for New Materials and Devices '13 (2013 Sheraton Kona, The Big Island, Hawaii, USA).